EXCITATION OF THE SCHUMANN BAND BY LIGHTNING AND OTHER TRANSIENT EVENTS

By

QUINCY A. FLINT

A DISSERTATION PRESENTED TO THE GRADUATE SCHOOL
OF THE UNIVERSITY OF FLORIDA IN PARTIAL FULFILLMENT
OF THE REQUIREMENTS FOR THE DEGREE OF
DOCTOR OF PHILOSOPHY

UNIVERSITY OF FLORIDA

2022

I dedicate this dissertation to my parents
Robert and Donna

ACKNOWLEDGEMENTS

This dissertation is the culmination of seven years of dedication to the Ionospheric Radio Lab at The University of Florida. It has been my honor to work with many wonderful colleagues during the course of my graduate studies, many of whom I wish to acknowledge here.

First and foremost, I would like to thank my advisor, Prof. Robert Moore, for his unwavering support and guidance throughout my graduate career. His constant insistence on critically applying the scientific method has made me a better researcher and engineer. The many late-night lab conversions and backyard barbecues will not soon be forgotten.

I would like to express my thanks to my Ph.D. supervisory committee members for their help and guidance along my path to graduation. In and outside of the classroom, I owe a great debt of gratitude to Prof. Moore, Prof. Rakov, Prof. Uman, and Prof. Harris for providing me with the opportunity to grow in the department and in the research field. I thank Prof. Matcheva for her valuable perspective as my external committee member.

The content of this dissertation was greatly enhanced by the diligent work of amateur observers Kevin Palivec and Thomas Ashcraft. Their impressive ground-based optical observations of TLEs, with careful timing and location information, enabled the precise analysis of radio observations in Chapter 2.

I am also grateful to Alfred Chen and the ISUAL team at National Cheng Kung University, Taiwan, for their rigorous work supplying global TLE observations from the ISUAL satellite, which are used extensively for the statistical analysis presented in Chapter 3.

Thanks is also due to Ryan Said and Ron Holle at Vaisala, Inc. for supplying the GLD360 data set used in the analysis of Chapter 4. The use of this data set dramatically simplified lightning-to-receiver distance calculations.

I extend a hearty thanks to past and present members of the Ionospheric Radio Lab with whom I have worked, including Dr. Michael Mitchell, Dr. Daniel Kotovsky, Neal

Dupree, Dr. Hunter Burch, Clint Snider, and Harrison Burch. Your support and encouragement has not gone unappreciated. I owe a special debt of gratitude to Dr. Hunter Burch who has been an exceedingly positive influence over the last several years. I thank both Hunter and his wife, Margaret, for being wonderful friends.

Lastly, I would like to acknowledge my family. This work would not have been possible without your love and support. Mom, Dad, Toby, and Jenni, thank you for always being there for me. There is no substitute for family.

The work presented in this dissertation was supported by DARPA/US Air Force contract FA8650-15-C-7535, DARPA grants HR00111820013, D19AC00009, and HR001121C0081, and NSF grant AGS-1521747 to the University of Florida.

TABLE OF CONTENTS

page

LIST OF TABLES

LIST OF FIGURES

Figures page

Abstract of Dissertation Presented to the Graduate School
of the University of Florida in Partial Fulfillment of the
Requirements for the Degree of Doctor of Philosophy

EXCITATION OF THE SCHUMANN BAND BY LIGHTNING AND OTHER TRANSIENT EVENTS

By

Quincy A. Flint

May 2022

Chair: Robert C. Moore
Major: Electrical and Computer Engineering

The Schumann Resonances are observed as peaks in the natural radio spectrum below 100 Hz, and they provide an important means to evaluate the energy budget of the Global Electric Circuit, a concept that attempts to explain basic energetic coupling mechanisms between different regions of near-Earth space. These naturally-occurring resonances are historically thought to be driven by lightning, which radiates a broad spectrum due to its impulsive nature, and a significant amount of observational evidence supports this characterization. With the relatively recent discovery of fantastical optical emissions, known as transient luminous events (TLEs), above thunderstorms, scientists have identified additional potential sources of radio impulses with spectral content below 100 Hz. Previous investigations have attempted to estimate the relative contribution of these other sources of extremely-low-frequency (ELF) radio impulses to the Schumann Band and Global Electric Circuit, and while these studies offer some insight, none have been comprehensive enough to answer key questions, such as: Are the Schumann Resonances driven by lightning?

This dissertation uses experimental observations to quantitatively characterize extremely-low-frequency/very-low-frequency (ELF/VLF) transients, specifically Q-bursts (ELF only), N-bursts (ELF+VLF), and V-bursts (VLF only), and their relationships with TLEs. It compares satellite-based optical observations with ground-based radio observations to confirm these relationships on a statistical basis. Lastly, it analyzes one full

week of experimental observations performed using a global array of ELF/VLF receivers to quantify the relative contribution of each type of radio burst to the Schumann Band.

In the end, it determines that gigantic jet events overwhelmingly radiate Q-bursts, sprite events N-bursts, and typical cloud-to-ground lightning return strokes V-bursts. The relationship is complicated, however. Given an observation of a Q-burst, it is likely that a gigantic jet produced the transient, and given an observation of a V-burst, it likely that the causative source is a typical lightning return stroke. Given an observation of an N-burst, however, the source is more likely to be elves-producing lightning than sprites.

Experimental observations confirm that lightning is indeed the predominant driver of the Schumann Resonances. On average, V-bursts, N-bursts, and Q-bursts contribute roughly 76%, 23%, and 1%, respectively, of the Schumann energy budget. For over 2 hours per day, however, N-bursts contribute over 40% of the energy budget, demonstrating they are an important factor in the Global Electric Circuit. Moreover, for over 40 minutes per day, N-bursts contribute over 50% of the energy and therefore temporarily drive the Schumann Band. We thus conclude that while lightning is indeed the primary driver of the Schumann Resonances, elves-related lightning flashes are important and occasionally dominant contributors to the band and to the Global Electric Circuit.

CHAPTER 1
INTRODUCTION

The work presented in this dissertation experimentally quantifies the relative contributions of lightning and other transient events to the Schumann Band between 5 Hz and 50 Hz. The Schumann Resonances play an important role in the Global Electric Circuit (GEC), a model that attempts to explain the coupling of energy between the Earth's magnetosphere, ionosphere, troposphere, and ground. The GEC guides the scientific understanding of global-scale electrodynamic phenomena and can be used to assess important societal impacts, such as how space weather can drive ionospheric currents that can cause billions of dollars of damage to power grids, or how lightning activity can be used as a quantitative measure of global climate change.

Lightning has long been thought to be the primary and perhaps exclusive driver of the Schumann Resonances [*Galejs et al.*, 1972; *Sentman*, 1996; *Rycroft et al.*, 2012; *Slyunyaev et al.*, 2019]. This perspective slowly started to change with the discovery of transient luminous events (TLEs), flashes of visible light high above thunderstorms, in the late 1980's [*Vaughan and Vonnegut*, 1989; *Franz et al.*, 1990; *Boeck et al.*, 1992; *Sentman et al.*, 1995; *Wescott et al.*, 1995; *Boccippio et al.*, 1995; *Fukunishi et al.*, 1996; *Pasko et al.*, 2002; *Su*, 2003]. Some TLEs, such as sprites and gigantic jets, have long conducting channels between the cloud tops and the ionosphere [*Lyons*, 1996; *Lyons et al.*, 2003; *Pasko et al.*, 2001; *Pasko*, 2008]; the electrical currents within these channels can radiate strongly in the extremely low frequency radio band [*Cummer et al.*, 1998; *Reising et al.*, 1999; *Stanley et al.*, 2000; *Cummer*, 2003], exciting the Schumann Cavity. Scientists have previously attempted to estimate the contribution of such TLEs to the Schumann Band [*Williams*, 2006; *Satori et al.*, 2013; *Guha et al.*, 2017], but without a global array of instruments and comprehensive experimental observations, only gross estimates have been made. This dissertation uses experimental observations of ELF/VLF transients to much more accurately and quantitatively assess energetic contributions to the Schumann Cavity with 30-minute resolution for a one-week period in August 2016.

This introductory chapter provides the reader with the background necessary to understand the scientific contributions of this dissertation which are delineated at the end of the chapter. Chapter 2 provides a metric to distinguish three different types of ELF/VLF transients and experimentally associates these radio impulses with different types of TLEs or lightning. Chapter 3 leverages space-based observations of TLEs by the ISUAL satellite and employs the metrics identified in Chapter 2 to independently corroborate the TLEs identified by the ISUAL team. Chapter 4 quantitatively evaluates the contribution of each type of radio burst to the Schumann Band below 50 Hz using a full week of observations by the University of Florida's global ELF and VLF receiver network. At the end of Chapter 4, it will be clear that, while lightning is typically the dominant source of the Schumann Resonances, sprites and sprite-related lightning significantly contribute to and at times are the dominant drivers of the Schumann Cavity. Chapter 5 summarizes the contributions of this dissertation and suggests directions for future research.

1.1 A Brief History of Early Radio

Years of careful observations and scientific experimentation has contributed to our current state of understanding in the radio science community, but it was Guglielmo Marconi who first proved to the world that long-distance radio communication was possible [*Burrows*, 1962]. In the 19th century, it was widely believed that wireless communication was limited to line-of-sight transmissions, or inherently short-range transmissions [*Andersen*, 2017; *Marconi*, 1962, p. 106]. In 1901, however, Marconi made his famous first wireless transatlantic communication that helped to dispel that belief, forever changing the future of telecommunications. A Morse-code "S" was transmitted from Cornwall, England which he received in Newfoundland, Canada as three faint dots or "dits," as they are known in the radio community [*Marconi*, 1962, p. 106-107]. The transformative impact of his efforts on the field of radio is sealed by the 1909 Nobel Prize in Physics [*Marconi*, 1909], which he shared with engineer Karl Ferdinand Braun, for "contributions to the development of wireless telegraphy."

Marconi's work was made possible thanks to the efforts of many engineers, physicists, and hobbyists who preceded him. It was Heinrich Hertz's spark gap transmitter [*Hertz*, 1893, p. 30-53] that produced the electromagnetic signal required for the early generations of radio transmission. Hertz's radio transmitter in turn helped to validate the theoretical work laid out by James Clerk Maxwell [*Maxwell*, 1873] twenty years before. The reformulation of these complete yet cumbersome equations by Oliver Heaviside in the late 19th century [*Heaviside*, 1893a] using vector calculus [*Heaviside*, 1892, 1893b] provides us with a compact system of physically observed laws we know today as Maxwell's Equations.

At the time of Marconi's experiment, the mechanisms that enable long-distance radio wave propagation were not well understood or well accepted. Many years earlier, for instance, Gauss [*Gauss*, 1839; *Glassmeier and Tsurutani*, 2014], Stewart [*Stewart*, 1882], and others had considered the possibility of a conducting layer of the upper atmosphere, but the concept had not taken root. After Marconi's experiment, however, Arthur Kennelly [*Kennelly*, 1902] and Oliver Heaviside [*Heaviside*, 1902, p. 213-218] explained the long-distance propagation phenomenon using a conducting layer of the atmosphere to reflect the signals over the horizon. Nevertheless, the existence of the ionosphere remained entirely philosophical until *de Forest* [1912] experimentally proved its existence using a vertical radio-sounding technique that could readily be repeated. Still, the scientific community remained unaware, as pointed out by *Tuve* [1974], because this result was not broadcast to the world until Edward Appleton repeated the experiment in 1924 [*Appleton and Barnett*, 1925a, b; *Appleton*, 1927], a feat for which he later received a Nobel Prize in Physics [*Appleton*, 1964]. It would be this ionized layer of the lower atmosphere, known as the Kennelly-Heaviside layer, that would successfully explain the feasibility of over-the-horizon communication by guided means.

We now know that extremely low frequency (ELF, 3 Hz−3 kHz) and very low frequency (VLF, 3 kHz−30 kHz) radio signals can propagate to great distances (1,000's of km) around the globe with relatively low attenuation due to the existence of the ionosphere

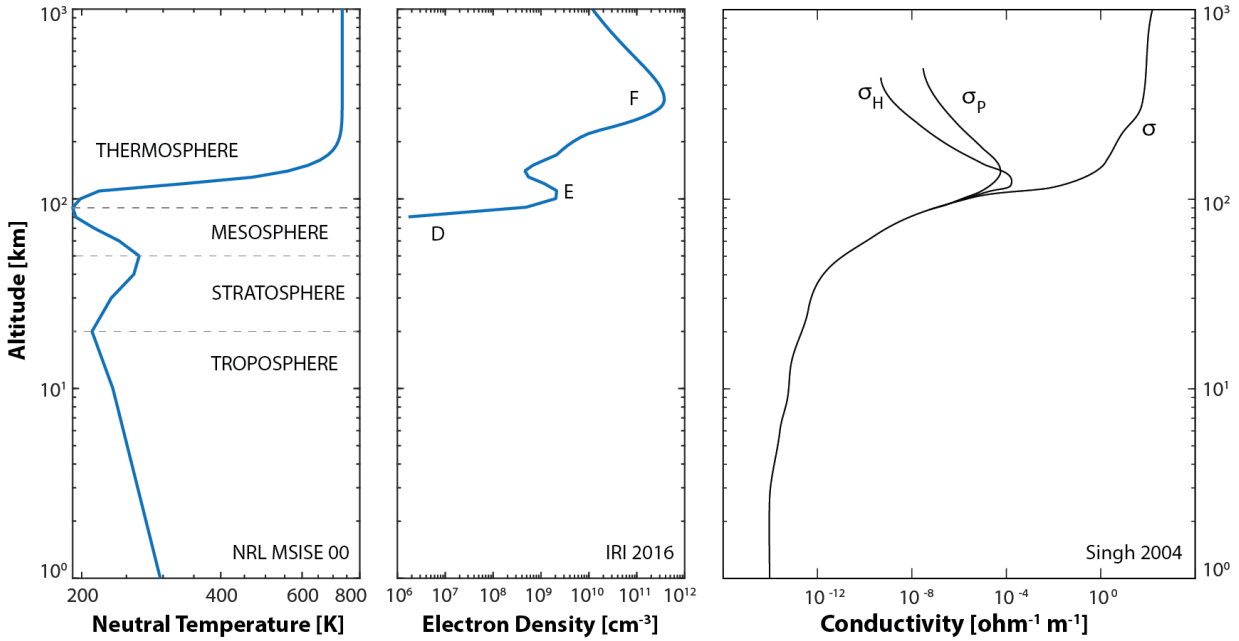

Figure 1-1. (left) Example neutral temperature profile obtained from NRL-MSISE-00. (middle) Example electron density profile obtained from the International Reference Ionosphere 2016. (right) Illustrative conductivity profiles obtained from *Singh et al.* [2004].

[*Holzer and Deal*, 1956; *Galejs et al.*, 1972; *Davies*, 1990, p. 367].

1.2 The Ionosphere

The ionosphere [*Watson-Watt*, 1926; *Mimno*, 1937; *Ratcliffe*, 1954; *Budden*, 1961; *Wait*, 1962; *Gardiner*, 1969] is the region of rarefied air in the Earth's upper atmosphere between ∼50 and 1,000 km altitude that is characterized by a significant increase in the number of free electrons. It serves both as the upper boundary of the Earth-ionosphere waveguide that supports ELF/VLF radio wave propagation around the globe [*Galejs et al.*, 1972] and as a charged surface whose existence contributes to a natural atmospheric electric field [*Jansky and Pasko*, 2014]. The vertical extent of the ionosphere is heavily dependent upon exposure to the Sun [*Eccles*, 1912], as solar Lyman-α radiation is the primary source of ionization in the region [*Watanabe et al.*, 1955; *Houston Jr*, 1958; *Nicolet and Aikin*, 1960; *Whitten and Poppoff*, 1965].

The regions of the upper atmosphere can be characterized by inversions in

temperature and are designated the troposphere, stratosphere, mesosphere, and thermosphere, as shown in the left panel of Figure 1-1. While the neutral gas density and atmospheric pressure decrease exponentially with altitude away from the Earth's surface, the number of free electrons tends to increase with altitude due primarily to ionization by solar radiation, as illustrated in the middle panel of Figure 1-1. This panel also shows that the ionosphere can be characterized based on rapid changes in electron density, with D-, E-, and F-regions labeled on the chart. The decreasing number of neutral particles together with the increasing number of free electrons produces a rapid increase in mean-free-path and thereby conductivity with increasing altitude above the surface of the Earth. The ionosphere is anisotropic, however, due to the presence of the Earth's magnetic field. It is therefore instructive to consider the Pedersen, Hall, and Parallel conductivity components [Bittencourt, 1995, p. 639]:

$$\sigma_P = \frac{N_e q_e^2}{m_e}\left[\frac{\nu + j\omega}{(\nu + j\omega)^2 + \omega_{ce}^2}\right] \tag{1-1}$$

$$\sigma_H = \frac{N_e q_e^2}{m_e}\left[\frac{\omega_{ce}}{(\nu + j\omega)^2 + \omega_{ce}^2}\right] \tag{1-2}$$

$$\sigma_{||} = \frac{N_e q_e^2}{m_e}\left[\frac{1}{\nu + j\omega}\right] \tag{1-3}$$

where N_e is the electron density, q_e is the electron charge, m_e is the electron mass, ν is the electron-neutral collision frequency, ω_{ce} is the cyclotron frequency, defined as $|q_e|B_0/m_e$, B_0 is the strength of the Earth's magnetic field, and ω is the frequency of the wave.

An illustrative set of these conductivity components, taken from *Singh et al.* [2004], is plotted in the right hand panel of Figure 1-1. The components shown here are not calculated directly from the values in the left two panels, but illustrate an important point. The reflection of ELF/VLF waves is brought about by the rapid change with altitude in Pedersen conductivity below 100 km altitude, shown in the plot. This data set also

highlights the large parallel conductivity component above 100 km altitude, which supports the existence of field-aligned currents that couple the ionosphere with the magnetosphere. Additionally, this figure highlights the non-zero conductivity that extends from ionospheric altitudes all the way down to the ground, supporting electrical atmospheric currents. Both the high altitude parallel conductivities and the non-zero low altitude conductivities support electrical currents that are important components of the Global Electric Circuit.

Returning to the ionosphere, VLF signals are typically taken to reflect from the D-region ionosphere [*Galejs et al.*, 1972], whereas ELF signals are typically taken to reflect from the lower E-region [*Cummer and Inan*, 2000; *Pappert and Moler*, 1974]. ELF and VLF signals are thus sensitive to changes in ionospheric electron density and temperature produced by space weather events, such as solar X-ray flares [*Thomson and Clilverd*, 2001; *McRae and Thomson*, 2004; *Moore and Burch*, 2018], galactic γ-ray bursts [*Inan et al.*, 2007], and auroral precipitation events [*Cummer*, 1997], among others. By modifying the ionospheric conductivity, space weather events in turn affect the distribution of charge throughout the lower atmosphere, resulting in so-called Wilson currents which transfer charge from storm clouds to the ionosphere. Over time, these charges redistribute from the ionosphere to the ground in regions of air where mechanisms for charge separation are not active. These regions of inactivity are called fair-weather regions [*Ogawa*, 1985; *Chalmers*, 1967], and they are disrupted by active solar winds and geomagnetic storms [*Siingh et al.*, 2007; *Tinsley*, 2000]. Because variations in the ionosphere affect charge distribution throughout the atmosphere, we now turn our attention to the Global Electric Circuit, and in particular the role the ionosphere plays in the Global Electric Circuit.

1.3 The Global Electric Circuit

The Global Electric Circuit (GEC) is a model that aims to describe the electrical charge distribution throughout the various layers of Earth's atmosphere and magnetosphere and the redistribution of those charges during transient events. Figure 1-2 depicts many of the physical aspects considered by the traditional view of the GEC and

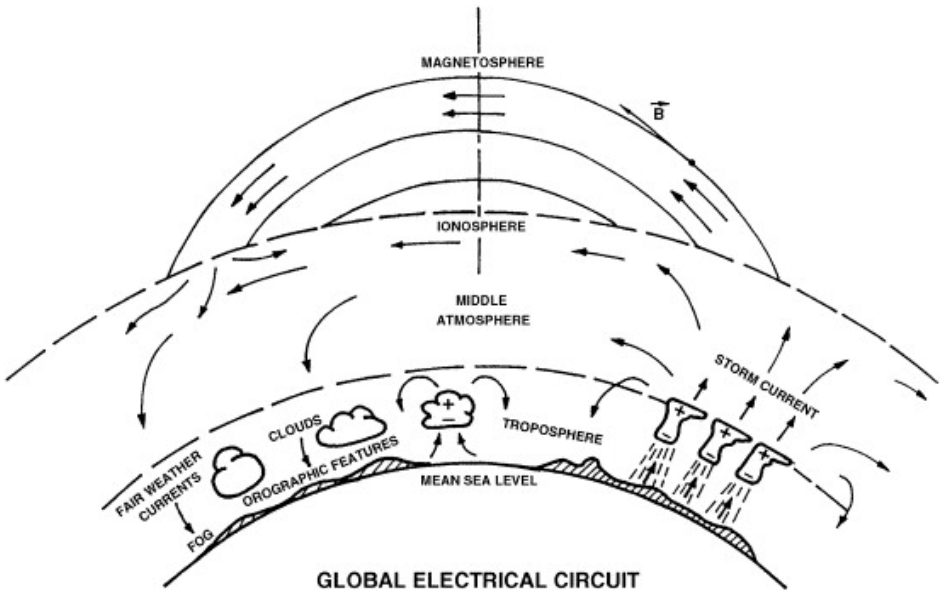

Figure 1-2. Illustration of physical mechanisms included in the traditional Global Electric Circuit [*Roble and Tzur*, 1986; *Siingh et al.*, 2007].

illustrates the steady-state flow of electric currents in the atmosphere that maintain the steady-state distribution of charge within the GEC [*Bering III et al.*, 1998]. Wilson currents, named after C.T.R. Wilson who proposed the idea in 1920 [*Wilson*, 1920], flow upward from thunderstorm clouds to the ionosphere, depositing charge on this layer. Field-aligned magnetospheric currents contribute substantially to the GEC, especially at high latitudes, and provide a means to transport charge to the magnetosphere or even between hemispheres [*Williams*, 2009]. The ionospheric charge is also slowly lowered to the ground over time via fair-weather currents. Meanwhile, charge can be returned to the clouds by cloud-to-ground lightning discharges.

This description of the GEC can be modeled using a set of leaky capacitors and switches [e.g., *Rycroft and Odzimek*, 2012], as shown in Figure 1-3. For each atmospheric layer, a leaky capacitor is set to maintain a certain charge and support a certain current under steady-state conditions. For each "event," a switch is used to discharge the appropriate capacitor, setting into action a charge redistribution that occurs with readily calculable RC time constants. In this way, both steady-state atmospheric currents and

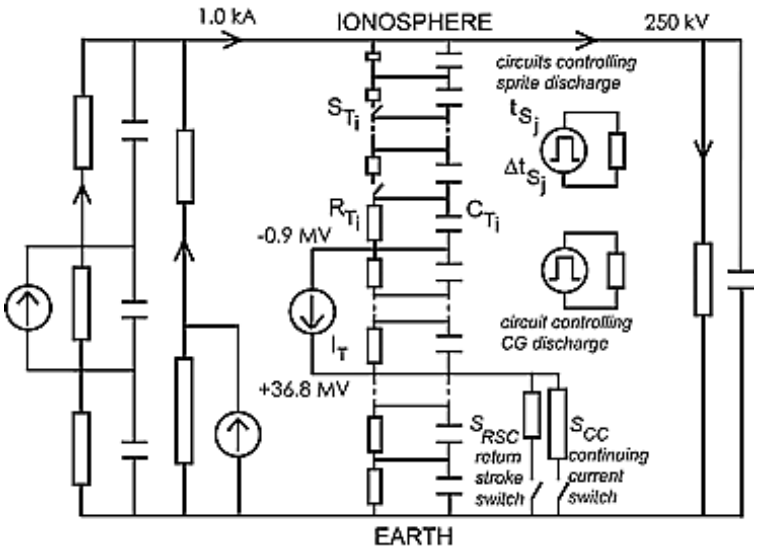

Figure 1-3. Circuit diagram of a thunderstorm as series resistors in parallel with capacitors attached to an elevated charge source in a switch circuit [*Rycroft and Odzimek*, 2012].

transient discharges are modeled.

Space weather and similar events couple to this circuit by modifying the resistivity and conductivity at ionospheric altitudes, in turn modifying the values of the resistors and capacitors for the ionospheric components. Transient luminous events and lightning, on the other hand, provide a means to discharge components of the circuit. Figure 1-3 specifically identifies switches that correspond to lightning-related return strokes and continuing currents. At higher altitudes, it identifies circuitry intended to model discharges associated with sprites.

It is now well recognized that TLEs, and specifically gigantic jets and sprites, play important roles in the GEC [*Sato and Fukunishi*, 2003; *Füllekrug and Rycroft*, 2006]. Gigantic jets form a direct connection from the cloud to the ionosphere and transfer charge between these regions [*Pasko et al.*, 2002; *Su*, 2003]. Sprites are initiated by large cloud-to-ground charge transfers produced by the parent lightning flash and their conducting streamer channels at high altitudes transfer charge in the upper atmosphere [*Pasko*, 2010].

Of course, the transient charge transfers modeled by the GEC are associated with time-varying currents that can radiate electromagnetic waves. In the context of the global electric circuit, this radiation is typically considered to be <100 Hz, but higher frequency components are also radiated, as will be discussed in later sections. The components below ~100 Hz are interpreted as exciting the Schumann Cavity and comprises what is sometimes referred to as the AC component of the Global Electric Circuit, or alternatively as the Schumann Resonances.

1.4 The Schumann Resonances

The conducting Earth and conducting lower ionosphere together form a spherical resonant cavity, which is referred to as the Schumann Cavity. ELF radio waves may propagate around the globe multiple times in different directions within the Schumann Cavity and excite the natural resonances of the cavity. In this case, when the wavelength of the radio wave approaches integer multiples of the radio circumference of the Earth, these natural resonances are stimulated [*Sentman*, 1996]. This phenomenon was first conceived by *Schumann* [1951, 1952] and bears his name. In the case of the Schumann Cavity, for signals below 100 Hz, the transverse electromagnetic (TEM) mode (which will be discussed with Equations 1-6 and 1-7) is the only propagating mode, and it can be expanded as a sum of Schumann Modes as [*Sentman*, 1996]:

$$E(\theta,\omega) = \hat{r}\frac{iI(\omega)\,ds}{4\pi a^2 h_1 \epsilon_0}\omega \sum_n \frac{2n+1}{(\omega-\omega_n)(\omega+\omega_n^*)} P_n(\cos\theta) \tag{1-4}$$

$$H(\theta,\omega) = \hat{\phi}\frac{iI(\omega)\,ds}{4\pi a^3 h_1 \epsilon_0 \mu_0}\omega \sum_n \frac{2n+1}{(\omega-\omega_n)(\omega+\omega_n^*)} P_n^1(\cos\theta) \tag{1-5}$$

where $I(\omega)$ is the Fourier transform of the current source as a function of angular frequency ω, a is the radius of the Earth, h_1 is the conductivity boundary height for the middle atmosphere ($\sigma = \epsilon_0\omega$), ϵ_0 is the free space permittivity, μ_0 is the free space permeability, P_n is the associated Legendre polynomial, P_n^1 is the associated Legendre polynomial of the first degree and order n, and $\omega_n/2\pi = f_n$ are the fundamental resonance modes in a

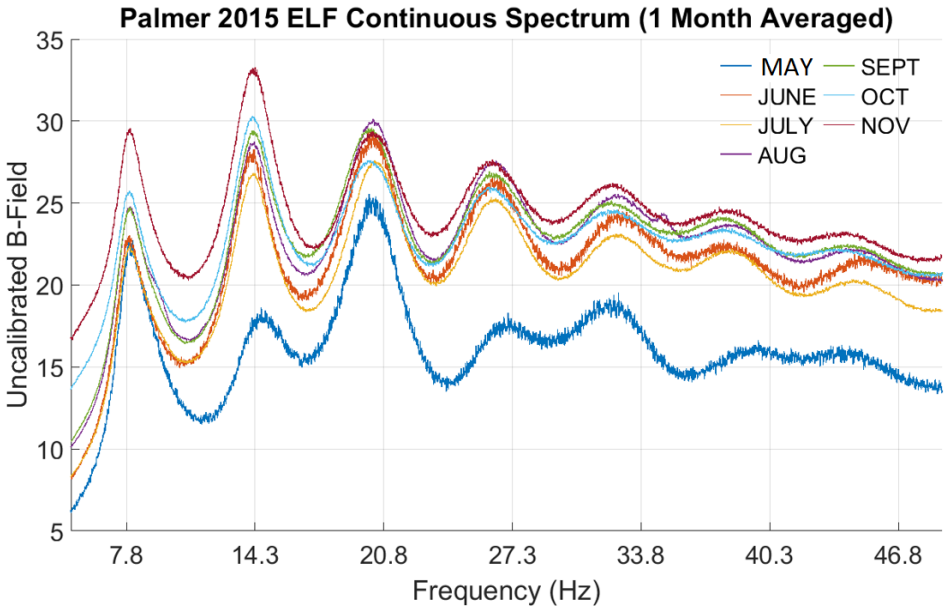

Figure 1-4. The first 7 modes of the Schumann Resonances observed from Palmer Station. The monthly averages are plotted to highlight seasonal variation in amplitude.

perfectly reflecting cavity. In practice, the fundamental frequency of the first SR mode fluctuates about a nominal center frequency of 7.8 Hz with higher order resonances spaced ~6.5 Hz apart [*Balser and Wagner*, 1960; *Wait*, 1962; *Shvets et al.*, 2010].

The resonant amplitude peaks and resonant frequencies of the Schumann Resonances vary as a function of the time of day, season, and solar cycle [*Balser and Wagner*, 1962; *Ogawa et al.*, 1969; *Williams*, 1992; *Fullekrug*, 1996; *Fullekrug and Fraser-Smith*, 1996]. This phenomenon is readily observable in Figures 1-4 and 1-5. This data is obtained from the low-ELF receiver at Palmer Station, Antarctica which was installed in May of 2015 and has provided reliable, continuous measurements since then. In Figure 1-4, the first seven modes of the Schumann Resonances are clearly distinguishable. Monthly averages of the ELF data show the variation in Schumann Resonance mode peak amplitudes with season. The peak mode amplitudes also change dramatically throughout the day as can be seen in the left and right panels of Figure 1-5 in which the monthly-averaged amplitude of the 3rd SR mode is plotted over the course of a day. The North-South channel shown in the left panel of Figure 1-5 experiences daily maxima at 0900 UTC and 2100 UTC, corresponding

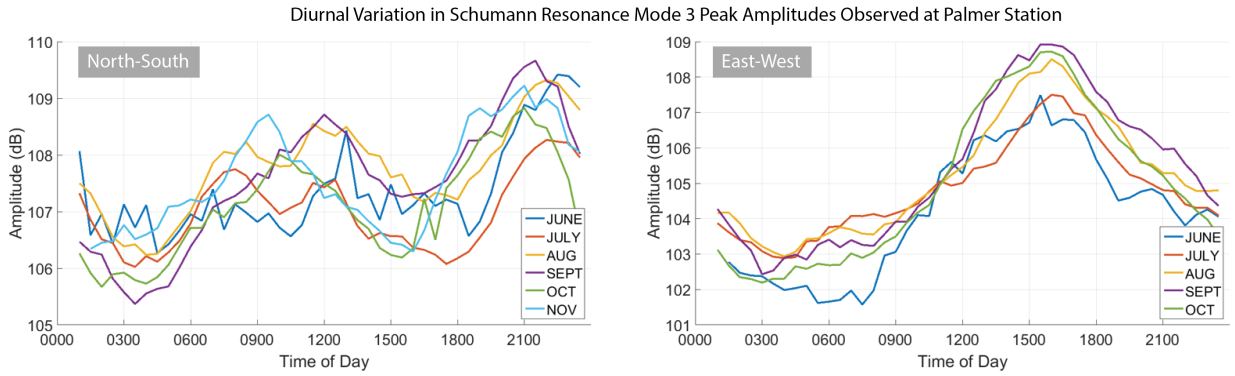

Figure 1-5. The daily variation in the peak amplitude of the 3rd mode of the Schumann Resonance. The North-South channel has maximum amplitudes during peak lightning activity in Asia and the Americas. The East-West channel has a clear maximum in amplitude during peak lightning activity in Africa.

to peak lightning hours in Asia and the Americas. The East-West channel shown in the right panel peaks at 1500 UTC, corresponding to the peak lightning hours in Africa.

Of course, this effect has long been of interest to workers in the atmospheric electricity field and beyond. Figure 1-6 shows the perceived variation in fair-weather electric fields against the perceived levels of lightning-driven electric fields. The top trace is known as the Carnegie curve as these records were obtained from experiments aboard a geophysical survey ship, the *Carnegie* [*Harrison*, 2012] by *Parkinson and Torrenson* [1931] and *Torreson et al.* [1947]. The correlation between the fair-weather electric field and the thunder occurrence rate was noted. It is now clear that the fair-weather electric field measurements are measurements of the Schumann Resonances which are driven in large part by lighting activity, explaining the correlation initially observed. The Carnegie curve indicates a potentially large (20%) diurnal variation in electric field values [*Füllekrug and Rycroft*, 2006] and thus, the Schumann Resonances.

This dissertation quantifies the excitation of the Schumann Band by measuring the energy present in the TEM field component below 50 Hz (as will be discussed with Equations 1-6 and 1-7) for different ELF/VLF transients. Because Equations 1-4 and 1-5 represent a decomposition of the TEM mode itself, the power and energy calculations performed represent an integration over the first 7 Schumann Modes.

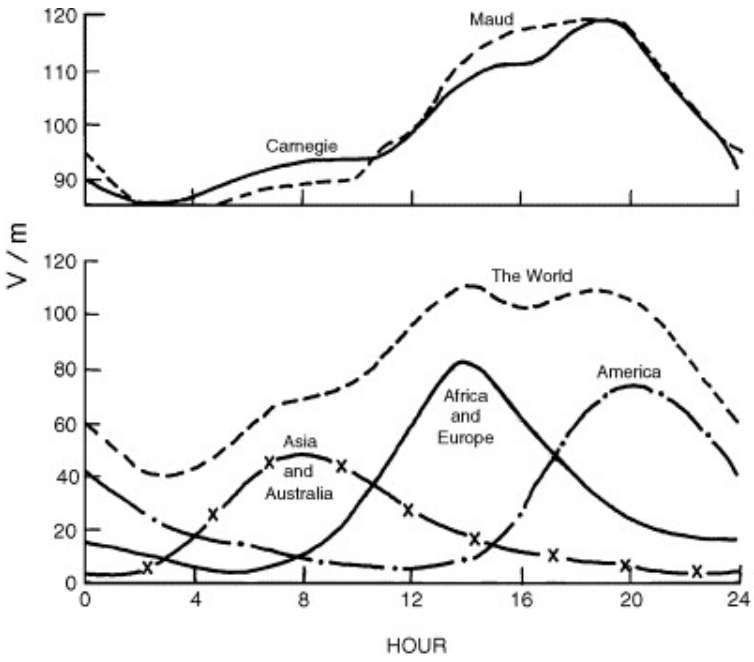

Figure 1-6. Global lightning variation and ELF band energy: Carnegie Curve [*Roble and Tzur*, 1986; *Siingh et al.*, 2007].

The ELF/VLF transients measured in this work also exhibit spectral content well above 100 Hz. The propagation of the higher frequency components is not well described by the concept of the Schumann Cavity. Instead, in the next section, we consider radio wave propagation within a slice of the cavity, referred to as the Earth-ionosphere waveguide.

1.5 ELF/VLF Propagation in the Earth-Ionosphere Waveguide

The efficient reflection of ELF and VLF radio waves from the lower ionosphere and from the ground results in the formation of signals that can propagate to great distances around the globe with low attenuation within the waveguide formed by the Earth and the ionosphere (i.e., the Earth-ionosphere waveguide) [*Holzer and Deal*, 1956; *Galejs et al.*, 1972; *Davies*, 1990]. While the Schumann Cavity is fully three-dimensional and encompasses the whole Earth, the Earth-ionosphere waveguide represents a two-dimensional slice of the cavity and is typically used to evaluate wave propagation over distances less than half the circumference of the globe.

It is interesting to note that while VLF waves can propagate several thousand kilometers and still be detectable, ELF waves can propagate around the globe multiple

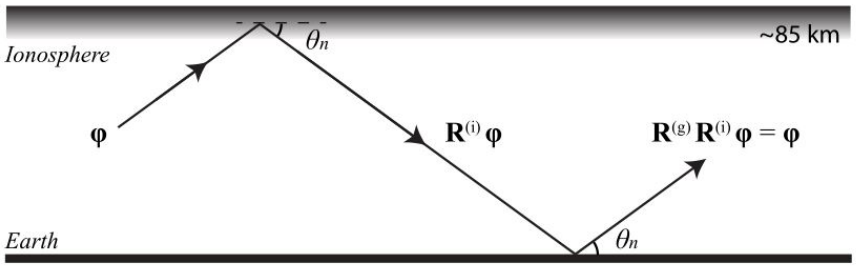

Figure 1-7. Diagram of VLF wave propagation in the Earth-ionosphere waveguide [*Kotovsky*, 2016].

times [*Ogawa et al.*, 1966b]. ELF and VLF propagation velocities are highly dependent on ionospheric conditions (particularly day-time vs. night-time variations), but it is generally accepted that VLF waves travel very near the speed of light [*Galejs et al.*, 1972, p. 310], whereas ELF signals propagate at nearly 80% the speed of light [*Füllekrug and Constable*, 2000; *Fullekrug*, 2005]. Due to this significant variation in propagation velocity, the signal waveform packet widens as it propagates farther from the source. This phenomenon is illustrated many times throughout this work as the ELF portion of the signal is delayed in time relative to the VLF portion of the signal, depending on distance from the source. Transients generated at the antipodal point about the Earth (and propagate halfway across the globe) can have ELF components lagging the VLF by as much as 35 ms, assuming propagation at 80% and 99.9% the speed of light, respectively.

Because signals at different frequencies propagate with different velocities, propagation in the Earth-ionosphere waveguide is considered to be dispersive. Moreover, each frequency component of a given waveform can potentially excite multiple waveguide modes, each of which propagate with a different attenuation rate, phase velocity, and group velocity. As depicted in Figure 1-7, in the Earth-ionosphere waveguide, a mode is formed when the propagation to the ionosphere, the reflection from the ionosphere, the propagation to the ground, and the reflection from the ground all together produce a signal that is in-phase, or reinforces, the original signal. These modes are formed for discrete (complex-valued) angles of propagation, called eigenangles, and these eigenangles

determine the attenuation rate, phase velocity, and group velocity of each mode.

For ELF/VLF signals above ∼2 kHz propagating in the Earth-ionosphere waveguide, multiple modes can propagate simultaneously, and the signal observed at a receiver is the sum total of all the modes incident upon the receiver. A signal source excites each waveguide mode with a distinct excitation factor, and then each mode propagates with the phase velocity and attenuation rate of the mode. The resulting electric and magnetic fields at the receiver are given by *Galejs et al.* [1972]:

$$E_\theta = -i\sqrt{\mu_0/\epsilon_0} Ids \sum_n S_n^{0.5} \Delta_n(z) F_n \tag{1-6}$$

$$B_\phi = -iIds \sum_n S_n^{0.5} F_n \tag{1-7}$$

$$F_n = \frac{i}{\sqrt{D\lambda h}} \sqrt{\frac{D/a}{\sin(D/a)}} G_n(z) G_n(z_s) \Lambda_n \exp(i\pi/4 + ik_0 D S_n) \tag{1-8}$$

where I is the current source, μ_0 is the free-space permeability, ϵ_0 is the free-space permittivity, $\lambda = 2\pi/k_0$ is the free-space wavelength, k_0 is free-space wave number, a is the radius of the Earth, h is the height of the ionospheric boundary, D is the source-receiver distance, $S_n = \sin(\theta)$ is the eigenvalue, Λ_n is the excitation factor, and $G_n(z)$ and $G_n(z_s)$ are the height gain functions for the receiver and source respectively evaluated at mode n.

For ELF signals less than $\sim$ 2 kHz, only a single mode propagates, dramatically simplifying the expressions above. In the single mode case, the electric field can be readily be expressed in terms of the B-field as:

$$E_\theta = \sqrt{\mu_0/\epsilon_0} \Delta_0(z) B_\phi. \tag{1-9}$$

Thus, for ELF wave components <100 Hz, the Poynting Flux can be simply calculated from the transverse electromagnetic (TEM) fields (i.e., for $n = 1$):

$$S = E \times H^* \tag{1-10}$$

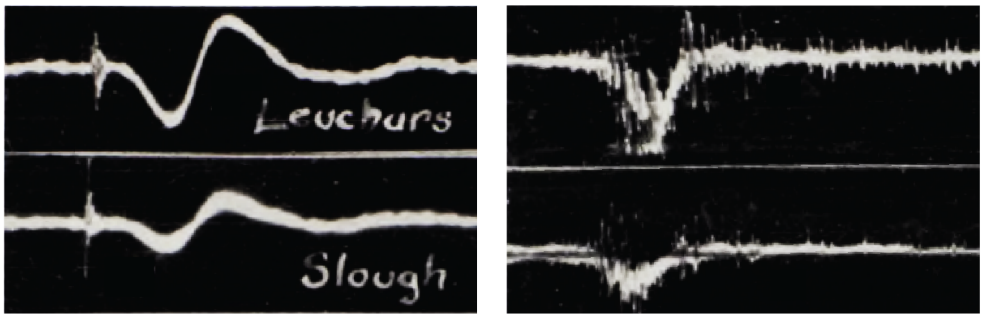

Figure 1-8. Early multi-site observations of ELF slowtails via cathode ray tubes and film photography [*Watson Watt et al.*, 1937]. Potential N-burst is shown in the left panels, wheras a potential Q-burst is shown in the right panels. Each record spans approximately 150 ms.

This expression yields the power radiated into the waveguide per unit cross-sectional area. Under the assumption that propagation conditions are approximately the same in all directions from the source, this expression can be integrated over the waveguide surface at a distance R from the source to yield the total power radiated into the waveguide, as will be done in Chapter 4.

1.6 ELF/VLF Transients: Experimental Observations

The theoretical discussion in the previous section may seem mathematically intensive, but the fact is that engineers and observational scientists have been fascinated by observations of transient enhancements in the ELF/VLF band (and their potential sources) for the better part of a century. Research on ELF/VLF transients began more than eighty years ago. *Appleton and Chapman* [1937] were the first to observe slow oscillatory tails following the initial lightning sferic impulse. In the same year, *Watson Watt et al.* [1937] presented a wide variety of ELF/VLF observations associated with lightning. An example N-burst and Q-burst observed by *Watson Watt et al.* [1937] (although not identified as such by the authors) are shown in Figure 1-8. Nearly thirty years later, and more than twenty years before the first confirmed sighting of transient luminous events far above thunderstorms, Ogawa and colleagues performed a series of careful radio observations of impulsive burst-like noise in the ELF/VLF band [*Ogawa et al.*, 1966b, a; *Ogawa and*

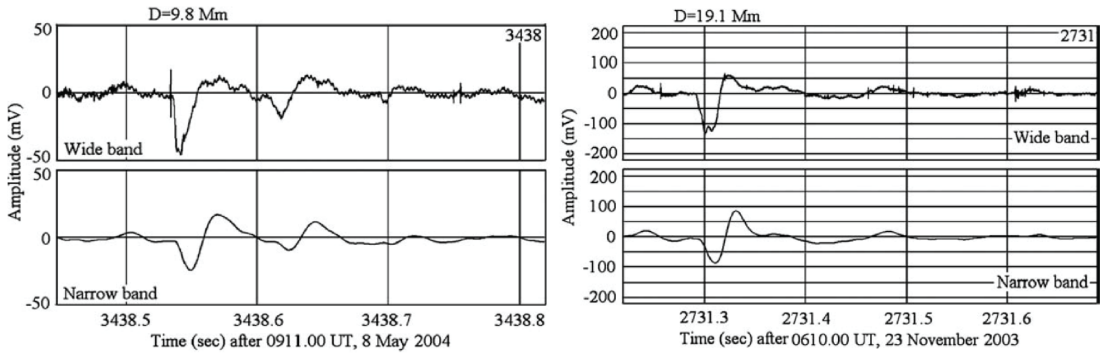

Figure 1-9. Observations of Q-bursts presented by *Ogawa and Komatsu* [2009].

Tanaka, 1967]. *Ogawa et al.* [1966b] specifically identified three classifications for the types of signals observed by *Watson Watt et al.* [1937]. The "ELF flash" and "ELF burst" both cover the broad class of transient events in the ELF range. Flashes are those events occurring (somewhat arbitrarily) within 1,000 km of the causative source; those measured beyond this threshold are termed bursts. The remaining ambient field is termed "ELF continuous."

The burst category is further refined by relative spectral content. *Ogawa et al.* [1966b] termed an event an N-burst (N for noisy) if the waveform contains significant ELF and VLF content and termed an event a Q-burst (Q for quiet) when the received wave has significant ELF content but little to no VLF. No quantitative definitions or thresholds were supplied. *Ogawa et al.* [1966b] suggested that N-bursts were associated with cloud-to-ground lightning, whereas the source of Q-bursts was not identified, given the information available at that time. While others had observed this behavior [*Watson Watt and Appleton*, 1923; *Watson Watt et al.*, 1937], *Ogawa et al.* [1966b] are generally credited with the detection and classification of ELF burst-like transients. Nevertheless, it should be noted that *Watson Watt et al.* [1937] presumed all of their observations, which included both Q-bursts and N-bursts, were associated with some form of lightning.

The impact of the work presented by *Watson Watt et al.* [1937] and *Ogawa et al.* [1966b] was not fully realized until the rapid expansion of TLE research in the 1990's and the associated effort to identify radio characteristics associated with the events [e.g.,

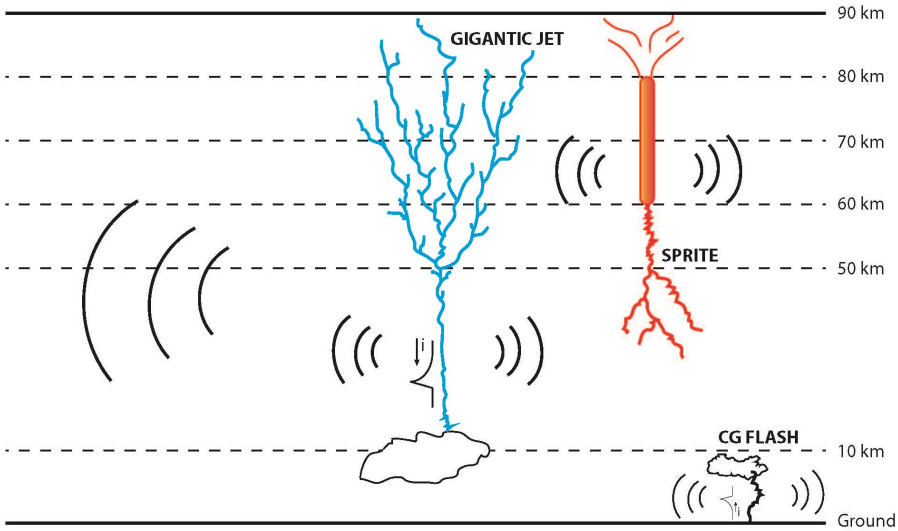

Figure 1-10. An illustration depicting waveguide excitation shown excited by a CG lightning flash, sprite, and a gigantic jet.

Boccippio et al., 1995; *Burke and Jones*, 1995; *Nickolaenko et al.*, 2010]. After the discovery of sprites and other TLEs, Ogawa and Komatsu revisited the Q-burst topic and published high quality observations of ELF transients [*Ogawa and Komatsu*, 2007, 2008, 2009], and a set of Q-burst observations are repeated from their work in Figure 1-9. *Ogawa and Komatsu* [2009] identify both bursts as Q-bursts despite a small VLF component being visible in the left hand panels, highlighting the need for a quantitative metric for burst characterization. In fact, we discuss these aspects in greater detail in the upcoming section on sprites and gigantic jets.

1.7 Potential Sources of ELF/VLF Transients

While lightning and transient luminous events are clearly possible sources for ELF/VLF transients, they are not the only potential sources. Intense γ-ray flares, and similar events that introduce rapid large-scale changes to the ionosphere, are also thought to be potential sources for ELF/VLF transients [*Tanaka et al.*, 2011; *Nickolaenko and Schekotov*, 2011]. In this dissertation, however, we consider and evaluate three potential sources for ELF/VLF transients, depicted in the cartoon diagram of Figure 1-10: lightning, sprites, and gigantic jets. Other TLEs are referenced in passing, and a study of extra-galactic sources is left for future work.

1.7.1 Cloud-To-Ground Lightning

Cloud-to-ground (CG) lightning has the effect of raising charge from the ground to the cloud or of lowering charge from the cloud to the ground; it produces radiated fields which can be observed at great distances as ELF/VLF transients. The majority of lightning discharges are intra-cloud discharges, which take place inside the thundercloud. Of the lightning discharges that connect to the ground, over 90% lower negative charge from the cloud to the ground (−CG). The remaining 10% or so effectively lower positive charge to the ground (+CG) by actually raising negative charge from the ground to the cloud [*Rakov and Uman*, 2003, p. 4].

The CG lightning discharge is composed of many elements and for insight into the complete process we refer the reader to [*Rakov and Uman*, 2003]. Here we highlight the components of the lightning flash that most affect the observed characteristics of the radio atmospheric (or sferic, or ELF/VLF transient).

Initially, a downward descending leader steps from the cloud toward the ground, depositing charge along the length of the channel. An upward propagating leader extends from the ground toward the channel, and upon connection a few hundred meters above the ground, launches a return stroke. The return stroke is a current pulse that propagates from the ground to the cloud at approximately half the speed of light, neutralizing the channel charge in the process. This process lowers negative charge to ground in the −CG case and raises negative charge to the cloud in +CG case. In some cases, a continuing current persists in the channel, perhaps accompanied by short impulses known as M-components.

The process of charge transfer is illustrated in Figure 1-11, which is reproduced from *Dwyer and Uman* [2014]. Upward propagating lightning of both polarities is also possible, but is not discussed in this work.

The typical −CG lightning discharge can displace 20 C of charge, and a typical continuing current can displace approximately 10 C of charge [*Berger*, 1975; *Rakov and Uman*, 2003].

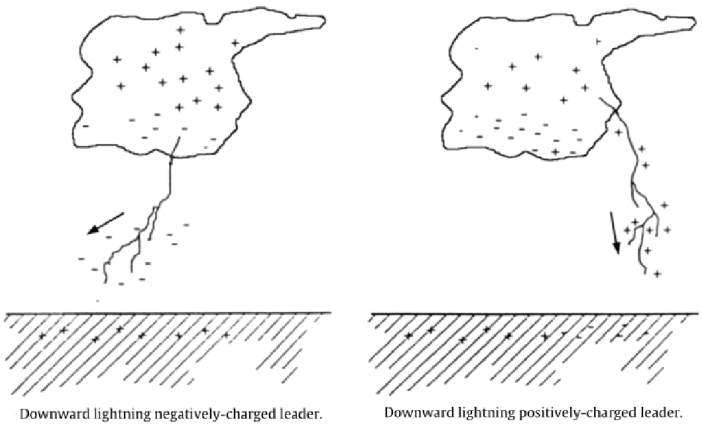

Figure 1-11. Charge transfer process in +CG and −CG lightning adapted from *Dwyer and Uman* [2014] and *Berger* [1967].

Radiation from lightning is largely impulsive, which produces a broad spectrum, including low and high frequencies. The length of the lightning channel is on the order of 5−10 km. Due both to the length of the channel and the timing characteristics of the return stroke current, the sferic radiates strongly in the VLF band and the spectrum peaks between 5 and 10 kHz [*Rakov and Uman*, 2003, p. 6]. It has been theorized that the continuing current is responsible for producing the ELF portion of the received sferic waveform [*Watson Watt et al.*, 1937; *Hepburn*, 1957; *Reising et al.*, 1996; *Cummer et al.*, 1998], often called the ELF slow tail [*Watson Watt et al.*, 1937; *Hepburn*, 1953]. Although the ELF component of a typical lightning sferic below 50 Hz is small, at a global flash rate of 50−100 per second, lightning likely contributes a significant amount of energy to the Schumann Band.

1.7.2 Transient Luminous Events (General)

Transient luminous events are a class of optical events oftentimes observed in conjunction with thunderstorms and sudden changes in the electric field that accompany the lightning discharge. The fortuitous 1989 detection of an optical event above a thunderstorm cloud associated with a lightning flash below by *Franz et al.* [1990] provided the first documentation of such an event. This momentous discovery pioneered the

investigation into a class of events that had been theorized many years before by C.T.R. Wilson [*Wilson*, 1924, 1956]. While observers over the years (primarily airline pilots) have described similar optical events [*Boys*, 1926; *Malan*, 1937; *Vaughan and Vonnegut*, 1989], it was the photograph by *Franz et al.* [1990] that sparked a community-wide interest into what have since become known as transient luminous events (TLEs).

Observers in the 1990's launched a series of successful campaigns [e.g. *Lyons*, 1994] across the Midwest United States to make more observations of these mysterious phenomena, later named sprites [*Sentman et al.*, 1995], to understand the basic underlying physics. In the process, they discovered several new TLEs including sprite halos [*Boeck et al.*, 1992; *Barrington-Leigh et al.*, 2001], elves [*Fukunishi et al.*, 1996], blue jets [*Wescott et al.*, 1995], and gigantic jets [*Pasko et al.*, 2002; *Su*, 2003]. Among these TLEs, the only serious potential sources for ELF/VLF transients are sprites and gigantic jets. Sprite halos are not likely to produce large currents, except in their relation to sprites. Blue jets may produce small transients, but perhaps far below the noise floor at any significant distance. Elves result from the intense heating of the ionosphere by the lightning electromagnetic pulse [*Taranenko et al.*, 1996], which produces rapidly expanding optical flashes in the ionosphere, but is not likely to produce significant currents to source ELF/VLF transients. We discuss sprites and gigantic jets in detail in the following sections.

1.7.3 Sprites

Sprites (see Figure 1-12) are large-scale brilliant transient luminous events that occur at 30−90 km altitudes high above thunderclouds [*Sentman et al.*, 1995; *Lyons*, 1996]. They appear as short-duration, red flashes of light, oftentimes generated by mesoscale convective systems [*Williams*, 1998]. They are believed to initiate when the quasi-static electric field associated with the charge transfer of a powerful lightning flash exceeds the breakdown potential of air at ionospheric altitudes [*Wilson*, 1924; *Pasko et al.*, 1997]. They have been observed to be laterally displaced from the parent lightning flash by as much as 30 to 50 km [*Wescott et al.*, 2001] and delayed by as much as 150 ms after the causative return

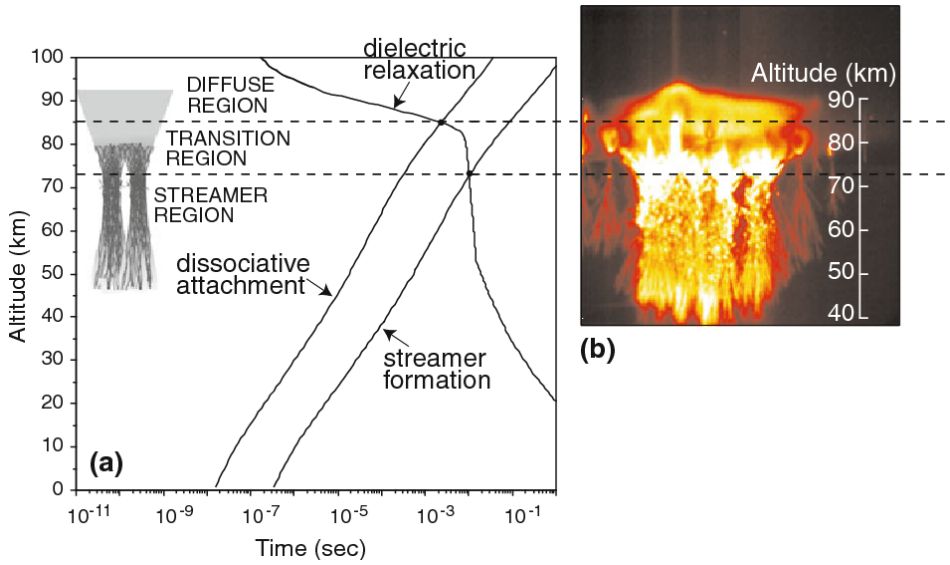

Figure 1-12. Depiction of the altitude distribution of the sprite structure with timescales of rates of relaxation and rates of attachment and streamer formation [*Pasko et al.*, 2013].

stroke [*Cummer and Füllekrug*, 2001; *Li et al.*, 2008]. Streamers initiating more rapidly after the parent lightning strike tend to appear at greater altitudes than delayed sprites which initiate at lower altitudes [*Hu et al.*, 2007; *Stenbaek-Nielsen and McHarg*, 2008; *Li et al.*, 2008]. Sprites have predominantly been observed in association with strong +CGs which displace large amounts of charge (100s of Coulombs) from the thundercloud [*Cummer and Inan*, 1997].

While sprite morphology varies case by case and appears to be connected to the amount of charge lowered to ground and the length of the lightning channel (*charge moment change*), the general structure is defined in three parts as shown in Figure 1-12 [*Pasko et al.*, 1998]. The sprite onset initiates in the streamer region, where a propagating streamer head rapidly stretches downward forming a vertical channel over tens of kilometers long [*Liu*, 2010]. In some cases, when the local field exceeds the breakdown potential, an upward travelling component will form [*Li and Cummer*, 2011]. Upward travelling streamers stop rapidly when the atmospheric conductivity is too great to support propagation [*Pasko et al.*, 2002]. Downward going streamers cease to propagate after a

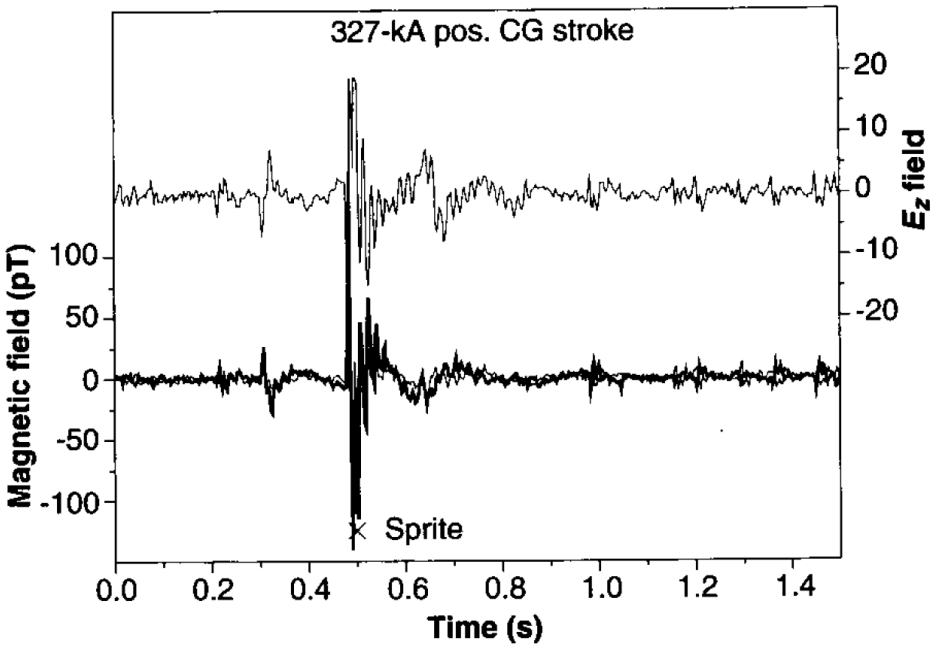

Figure 1-13. ELF signature of a sprite reported by *Boccippio et al.* [1995].

period of slow deceleration when the streamer electric field falls below 5% of the breakdown field [*Li and Cummer*, 2009]. In relatively longer exposure times, the streamer appears as a long tendril or channel, but in high-resolution photography a distinct streamer head is seen to light up only a small segment of the streamer path [*Stenbaek-Nielsen and McHarg*, 2008] while the channel behind the head can support current flow [*Liu*, 2010]. These streamers have not been observed to connect to the storm clouds, however modelling reports suggest this may occur in some instances [*Pasko et al.*, 2001]. It should be apparent that the sprite body itself serves to rearrange charges in the upper atmosphere and is expected to radiate in the ELF range.

In 1994, *Boccippio et al.* [1995] made visual observations of sprites occurring over the Midwest while making simultaneous measurements of the radio emissions of the same event at extremely low frequencies (ELF) at a station in Rhode Island, some 2,300 km distant. The observations associated the occurrence of a sprite with an ELF transient, repeated here in Figure 1-13, which *Boccippio et al.* [1995] strongly suggested was a Q-burst. Their work did not benefit from simultaneous ELF and VLF observations, however, and therefore

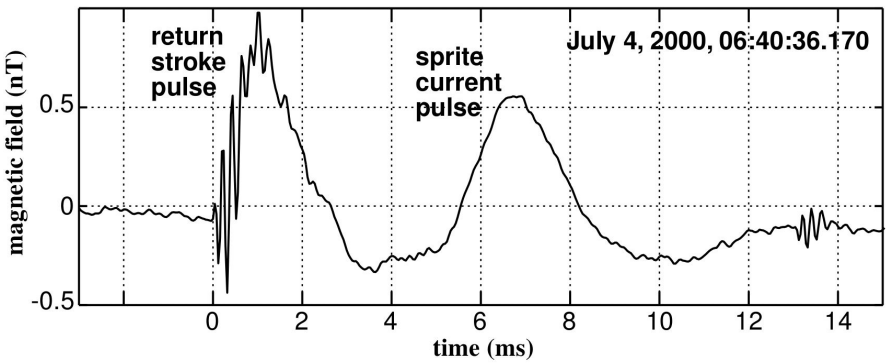

Figure 1-14. A Sprite current pulse is shown here in Duke University ELF B-field data trailing a return stroke pulse [*Cummer*, 2003].

a rigorous distinction between an N-burst and Q-burst could not be made. Nevertheless, the association between Q-bursts and sprites was made and has persisted in the literature, regardless of the presence or absence of VLF energy [e.g., *Burke and Jones*, 1995; *Williams*, 1998; *Ogawa and Komatsu*, 2007; *Nickolaenko et al.*, 2010; *Guha et al.*, 2017]. These ELF transients, without consideration for VLF spectral content, have long been used as a proxy to infer global rates of sprite occurrence [*Cummer*, 1997; *Reising et al.*, 1999; *Sato and Fukunishi*, 2003]. The term N-burst has been neglected altogether in the literature. Even the ELF/VLF summary chapter (Chapter 13) included in the seminal work by *Rakov and Uman* [2003] identify slow-tails as synonymous with Q-bursts, without consideration for VLF spectral content. Strangely enough, even the more recent articles (since 2000) published by *Ogawa and Komatsu* [*Ogawa and Komatsu*, 2007, 2008, 2009] support the Q-burst/sprite association, despite the explicit lack of simultaneous VLF observations to support this conclusion, as required by Ogawa's own definition of a Q-burst [*Ogawa et al.*, 1966b]. We note that by the quantitative metrics outlined in Chapter 2, it is likely that the ELF transient observed by *Boccippio et al.* [1995] would be identified as an N-burst.

Additional observations of *delayed sprites* have been used to identify *sprite currents* that also generate similar ELF portions of the sferic [*Cummer et al.*, 1998, 2006]. An example sprite current pulse can be seen in Figure 1-14. The return stroke pulse contains broadband energy above and below 1 kHz, while the sprite current primarily contains ELF

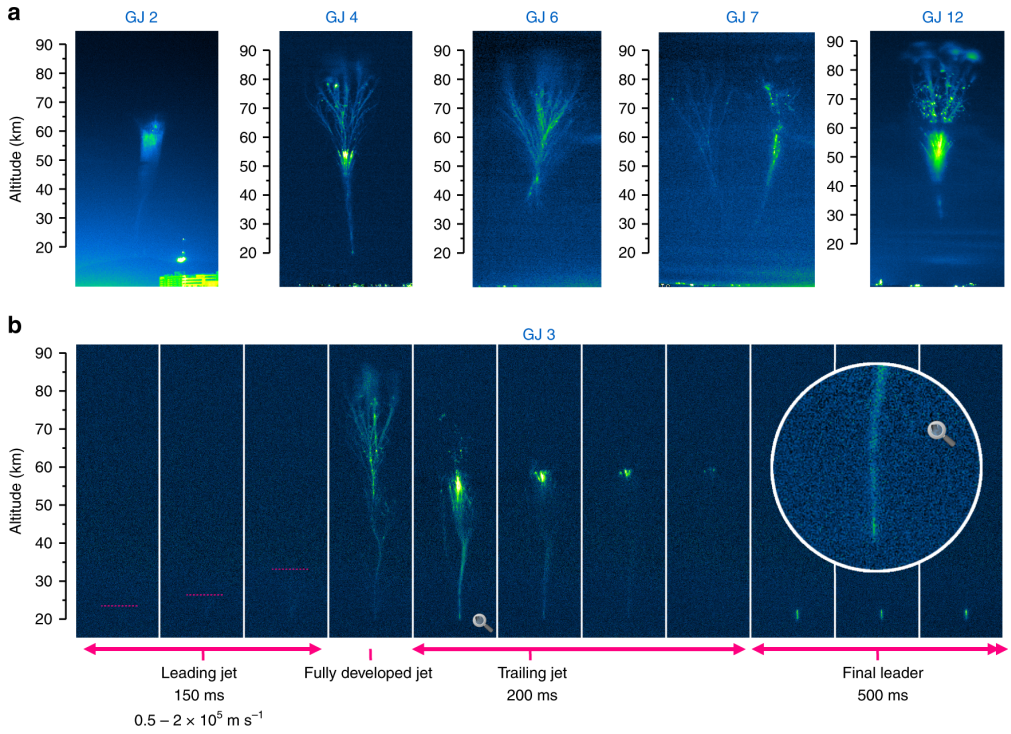

Figure 1-15. High-speed image evolution of a gigantic jet developing [*Van Der Velde et al.*, 2019].

energy below 1 kHz. Similar observations presented by *Reising et al.* [1999] demonstrated that the ELF current pulse coincided with a brightening of the sprite channel detected using the "Fly's Eye" photometer array. This coincidence strongly suggests that the sprite current was the source of the observed ELF pulse.

1.7.4 Gigantic Jets

Gigantic jets (GJ, see Figure 1-15) were first observed by *Pasko et al.* [2002] in Puerto Rico and subsequently by *Su* [2003] over the South China Sea. It consists of an upward propagating leader channel that initiates in the cloud and extends upward to ionospheric altitudes forming a direct connection between the cloud and the ionosphere. The gigantic jet develops over several 100s of milliseconds and reaches vertical lengths of $50 - 80$ km [*Su*, 2003; *Pasko*, 2008]. Gigantic jets transfer charge between the cloud and the ionosphere (like Wilson currents) thus serving to charge/discharge this region. They also radiate strongly at lower frequencies [*Van Der Velde*, 2010].

The gigantic jet channel develops in three primary stages. An initial rapid development from cloud to ionosphere called the *leading jet* forms in a matter of milliseconds. This process is similar to the stepped leader stage of conventional CG lightning [*Krehbiel et al.*, 2008]. Propagation velocities of the leading jet vary widely in the literature as the jet develops quickly compared to the frame rate of many low-light cameras. Measurements of velocities on the order of 10^5-10^6 m/s [*Soula et al.*, 2011] have been reported and are generally consistent with known propagation velocities of lightning leaders [*Pasko*, 2003; *Uman*, 2001]. After a brief period of apparent inactivity, the event appears to develop fully, creating a beautiful branching channel between the cloud and ionosphere. This re-brightening is short-lived as the event appears in full for only 10−100 ms [*Soula et al.*, 2011]. Some researchers suggest this process is comparable to the return stroke process in CG lightning [*Su*, 2003], while others suggest this process is more similar to the continuing currents observed in CG lightning [*Cummer*, 2009].

This initial development is followed by a secondary, slow rising structure called the *trailing jet*, occurring over a period of hundreds of milliseconds [*Su*, 2003]. The trailing jet propagates at reported velocities on the order of 10−100 km/s and has never been observed to reconnect to the ionosphere. This component fizzles out slowly at lower altitudes before halting altogether.

Occasionally, a *final leader* will appear at the tail end of an event as a persistent channel glow [*Van Der Velde et al.*, 2019]. See Figure 1-15 for a high-speed time series of this evolution [*Van Der Velde et al.*, 2019].

Estimates of the total charge transferred are obtained from field measurements [*Su*, 2003; *Cummer*, 2009] in a manner analogous to that used to measure sprite charge moment changes. Analysis of a negative gigantic jet by *Cummer* [2009] reported a total charge transfer of 144 C over a 74 km channel for a total charge moment change of 10,656 C-km, much greater than those first reported by *Su* [2003]. *Su* [2003] observed five gigantic jets with an average CMC of 1,425 C-km per event. *Van Der Velde* [2010] reported a charge

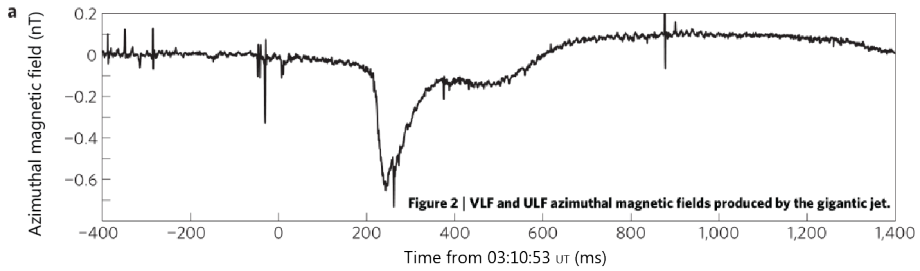

Figure 1-16. An ELF pulse associated with a gigantic jet is shown here in Duke University ELF B-field data [*Cummer*, 2009].

moment change of 11,600 C-km in association with a gigantic jet observed in Italy, corroborating the *Cummer* [2009] measurements. The gigantic jet may significantly affect the chemical composition of the ionosphere and our understanding of the charging and discharging of the Global Electric Circuit [*Pasko*, 2003]. The total amount of charge displaced by a gigantic jet is comparable to that moved by sprite-producing lightning (100s of Coulombs). Both sprite-lightning and gigantic jets tend to displace more charge than conventional CG lightning flashes.

Similar to sprites, gigantic jets are known to radiate a strong ELF component, but unlike sprites, they are not associated with a cloud-to-ground return stroke [*Su*, 2003]. While gigantic jets do appear to propagate in a fashion similar to CG lightning [*Krehbiel et al.*, 2008], observers have reported significantly slower current rise times than are observed in CG return strokes [*Cummer*, 2009]. *Cummer* [2009] estimated the current rose to its peak value in ∼30 ms, which is four orders of magnitude slower than the rise time measured in a typical −CG flashes (∼5 μ s) [*Rakov and Uman*, 2003]. ULF and ELF/VLF pulses have been observed to time align convincingly with the occurrence of gigantic jets [*Van Der Velde et al.*, 2007; *Van Der Velde*, 2010; *Lu et al.*, 2011; *Sung-Ming et al.*, 2012; *Van Der Velde et al.*, 2019]. One such example is shown in Figure 1-16, where the ELF/VLF transient exhibits only a small VLF component near 0 ms but a pronounced ELF component appears near 200 ms. The distinction between this type of ELF/VLF transient and the sprite-associated transients shown in Figures 1-13 and 1-14 is dramatic.

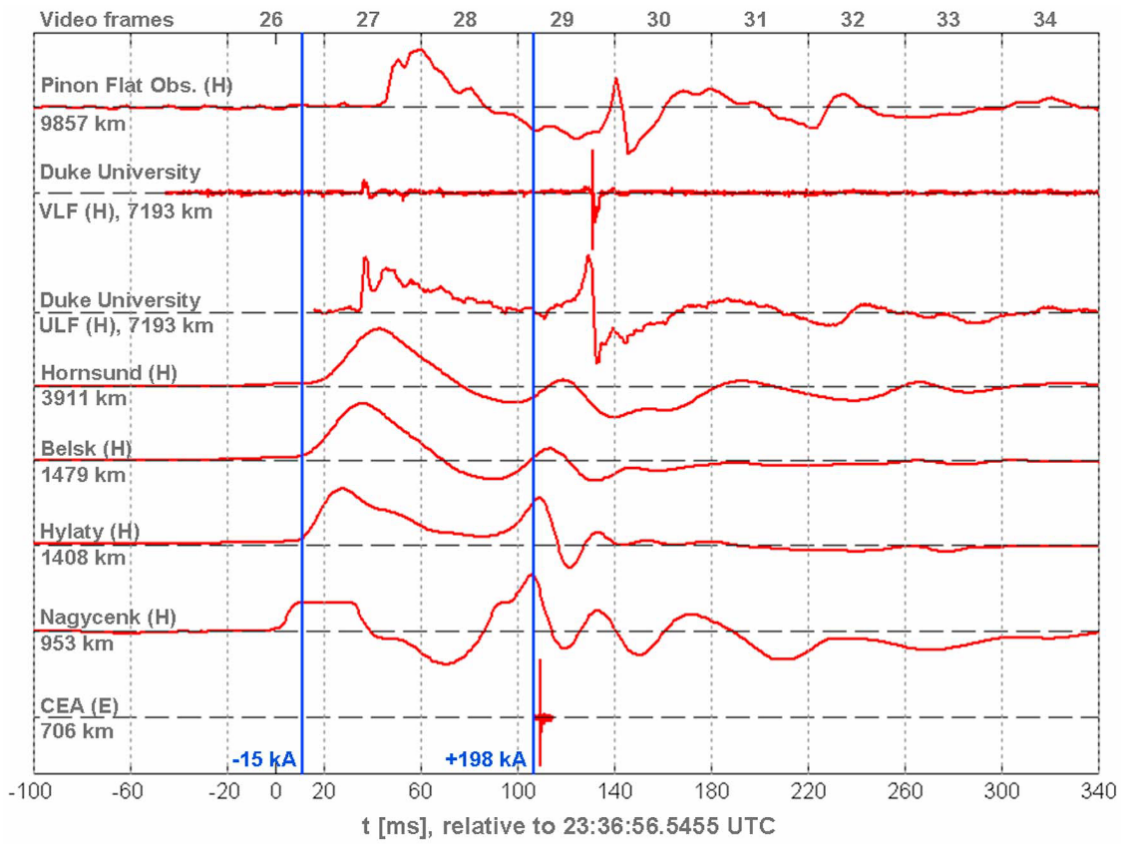

Figure 1-17. Global observations of ELF/VLF transients associated with a gigantic jet near 0 ms and a sprite near 100 ms [*Van Der Velde*, 2010].

One last example is particularly revealing. *Van Der Velde* [2010] recorded the occurence of a gigantic jet followed 80 ms later by a sprite. Figure 1-17 shows a global set of observations of the resulting ELF/VLF transients. The gigantic jet occurs first and registers as a slow undulation in all of the ELF channels. The two Duke University channels are most interesting, however, as they denote VLF observations and ULF (ultra-low-frequency) observations. The gigantic jet barely registers in the VLF channel, but exhibits a massive deflection in the ULF. The sprite occurs second, near 100 ms, and clearly launches a strong ULF/ELF/VLF wave that propagates around the world. Notably, the Duke VLF sensor detects a large VLF impulse.

These observations, together with the sprite observations, appear to illuminate the relationship between ELF/VLF transients, lightning, and transient luminous events. These

observations are rare, however, and a long-term statistical study has not been undertaken. It is not quantitatively clear what magnitudes of ELF and/or VLF content constitute detection of ELF and/or VLF components of the transient. Also, it is not clear whether these characteristics are reliable enough that a radio-based detection process can be implemented and trusted. Lastly, it has not been evaluated how these pulses contribute to the Schumann Cavity and the Global Electric Circuit. This dissertation presents new observations of ELF/VLF transients associated with gigantic jets, sprites, and elves, provides quantitative metrics for characterizing the ELF/VLF transients, performs the statistical analysis, and evaluates each event's statistical contribution to the Schumann Band.

1.8 Experimental ELF and VLF Observation Geometry

Experimental observations presented in this dissertation were performed by the Ionospheric Radio Lab at the University of Florida, which operates a global network of ELF and VLF radio receivers. A map of this global array is shown in Figure 1-18. These instruments continually monitor the magnetic field activity between 5 Hz and 42 kHz. The ELF receivers have a flat response between 5 and 500 Hz and are sampled at 5 kHz, or 10 kHz in some instances, while the ELF/VLF receivers have a flat response between 150 Hz and 42 kHz and are sampled at 100 kHz. The receiver systems are each composed of air-core loop antennas, low noise amplifiers, a length of audio cable, a line receiver with final gain and anti-alias filtering stage, and an analog-to-digital converter. The data is synchronized in time and frequency with a GPS trained oscillator providing absolute timing accuracy within 30 ns rms of UTC and frequency precision of 10^{-12} Hz [*Mitchell*, 2015]. The 16-bit resolution provided by our ADC allows for sensitive measurements with high resolution. The typical system exhibits better than 90 dB spurious free dynamic range.

The geographic distribution of ELF and VLF receivers is of special importance to this work. Remote, low noise environments such as those found in Antarctica, Greenland, and Alaska are ideal for making measurements below 1 kHz where power line noise regularly

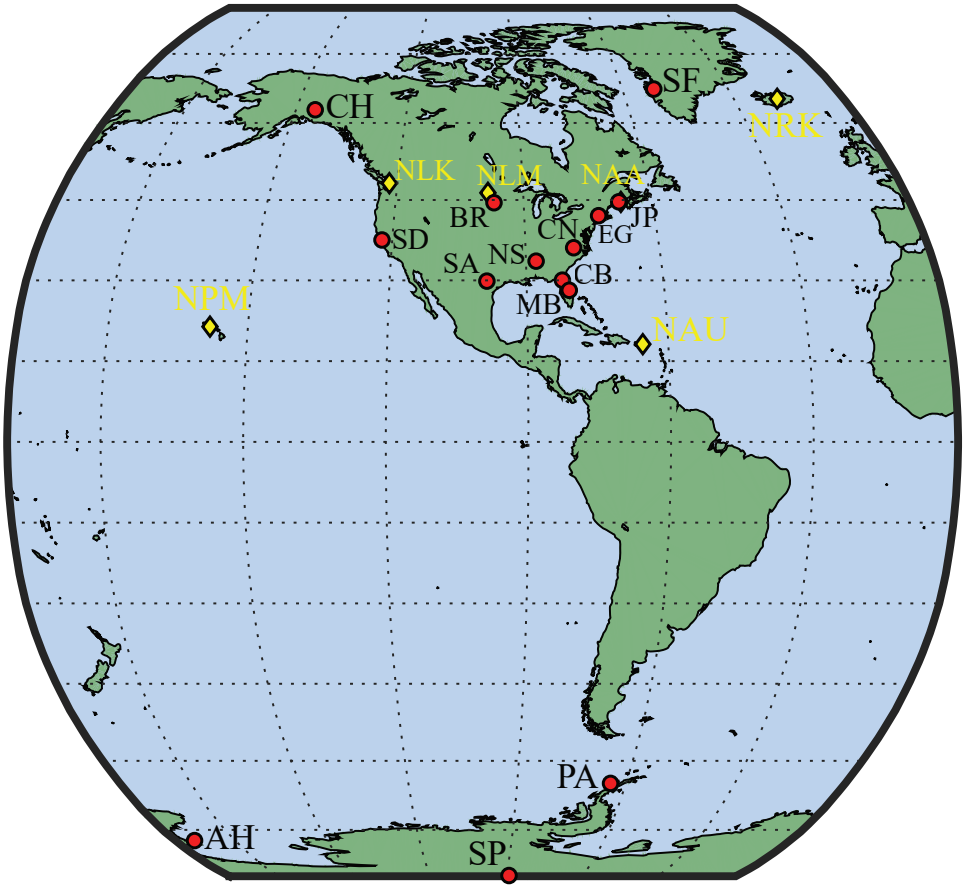

Figure 1-18. Map of University of Florida ELF/VLF receiver array (red circles) and North American VLF transmitters (yellow diamonds)

inhibits these measurements in more densely populated regions. None of our ELF receivers need to employ notch filters to reduce 50 or 60 Hz hum; such filters can meaningfully distort the frequency response of the system.

For ELF/VLF transient analysis, the ELF observations and ELF/VLF observations are used to produce three different signals. First the data on both receivers are rotated in post processing to output the transverse magnetic field for each transient. The ELF signal is then filtered to a bandwidth of 5-300 Hz. The ELF/VLF signal is filtered to two different bandwidths: an ELF component between 150 and 1000 Hz and a VLF component between 5 and 15 kHz. ELF signals from the ELF receiver are plotted by themselves, whereas the ELF and VLF components from the ELF/VLF receiver are plotted together.

1.9 Scientific Contributions

The work described in this dissertation contributes the following to the scientific understanding of the natural world:

1. Provided a quantitative metric to reliably characterize ELF/VLF radio transients. Definitively identified gigantic jets as a source of the Q-burst and sprites as a source of the N-burst; used the same definitions to identify a new class of radio transient, called a V-burst, and associate it with typical cloud-to-ground lightning.

2. Demonstrated a method to apply the metric to experimental observations and automatically distinguish between Q-bursts, N-bursts, and V-bursts based on the spectral content of the received ELF/VLF radio transient. Achieved event identification accuracy of 94% for Q-bursts, 92% for N-bursts, and 96% for V-bursts.

3. Evaluated the global occurrence rates of Q-bursts (2.1 per minute), N-bursts (49.6 per minute), and V-bursts (73.8 per second) using 1 week of global experimental observations from August 2016.

4. Assessed the relative energy contributions from Q-bursts, N-bursts, and V-bursts to the Schumann Band. Determined that on average 76% of the Schumann Resonances are contributed by V-bursts, 23% by N-bursts, and 1% by Q-bursts. V-bursts are responsible for more than 50% of the energy in the Schumann Band >23 hours per day, while N-bursts are responsible for more than 50% of the energy for 47 minutes per day.

5. Determined that typical lightning and elves-related lightning are responsible for the current sources that drive the Schumann Resonances.

CHAPTER 2
ASSOCIATING RADIO BURSTS WITH TRANSIENT LUMINOUS EVENTS

The introductory chapter highlighted the fact that for over twenty years, scientists have associated the fantastic optical flashes above thunderstorms known as sprites with a specific type of radio signature known as the Q-burst. At the same time, different ELF/VLF signatures have been reported to be associated with gigantic jets. Yet, there does not appear to exist a quantitative metric by which to distinguish transients associated with sprites from those associated with gigantic jets.

In this chapter, observations of ELF/VLF transients performed by the University of Florida's global ELF/VLF receiver array are used to determine a quantitative metric by which to characterize ELF/VLF transients as Q-bursts and N-bursts. A new type of transient is identified and deemed the V-burst. These metrics are used to analyze the ELF/VLF transients observed simultaneously with ground-based amateur optical observations of sprites and gigantic jets. In the end, the record is corrected, and sprites are associated with N-bursts, whereas gigantic jets are associated with Q-bursts. More importantly, the proposed metric can be employed to automatically process ELF/VLF transient observations to identify sprites and gigantic jets.

2.1 Description of the Experiment

On three separate nights in September 2016, ground-based images of TLEs were taken by amateur observers Kevin Palivec and Thomas Ashcraft. Palivec operated a Watec 902H Ultimate low-light camera with an 8mm CCTV fixed-focus lens recording at 60 fps from his observation station in Hawley, Texas. Ashcraft operated a mobile observation suite. A fourth event was detected by Diego Rhamon of the Brazilian Meteor Observation Network (BRAMON) in 2017 over Taperoa, Brazil using a Sony PY-SH361 CCTV camera from his home 100 km away in Campina Grande, Brazil.

Continuous ELF/VLF radio observations during these time periods were performed by the University of Florida's global ELF/VLF receiver array. The six receivers used in this work are located at Arrival Heights, Antarctica (AH, 77.8296°S, 166.6627°E),

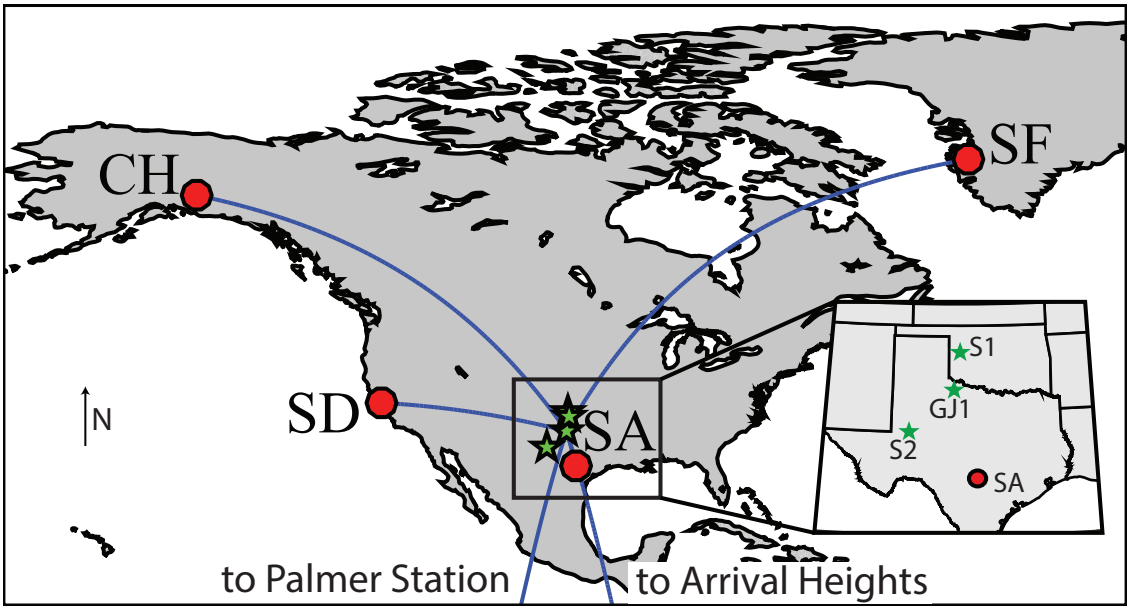

Figure 2-1. Map displaying the geographic distribution of UF's global ELF/VLF radio receiver network and location of two sprites and a gigantic jet over Texas and Oklahoma.

Chistochina, Alaska (CH, 62.6122°N, 144.6165°W), Palmer Station, Antarctica (PA, 64.7745°S, 64.0508°W), San Antonio, Texas (SA, 29.7613°N, 98.5687°W), Stanford, California (SD, 37.4093°N, 122.1805°W), and Sondrestromfjord, Greenland (SF, 66.9861°N, 50.9460°W). Receiver details are provided in Chapter 1. A map of the ELF/VLF receiver stations and the events analyzed in this study are shown in Figure 2-1.

2.2 Sprites and N-Bursts

On 10 September 2015, optical observations of a sprite were performed by Thomas Ashcraft over the Salt Plains National Wildlife Refuge in Cherokee, Oklahoma. A photograph of this event can be seen in Figure 2-2(C). Lightning records obtained from the National Lightning Detection Network (NLDN) confirm a positive cloud-to-ground (+CG) return stroke of 82 kA peak current at the same time, 03:39:14.419 UT, and location (36.779° N, -98.343° W). This event was detected at an ELF/VLF receiver located a short 671 km away in San Antonio, Texas as is shown in Figure 2-1.

Visual inspection of ELF and VLF data at this time shows the presence of an N-type radio burst. That is, a transient broadband pulse is observed in ELF and VLF data as the

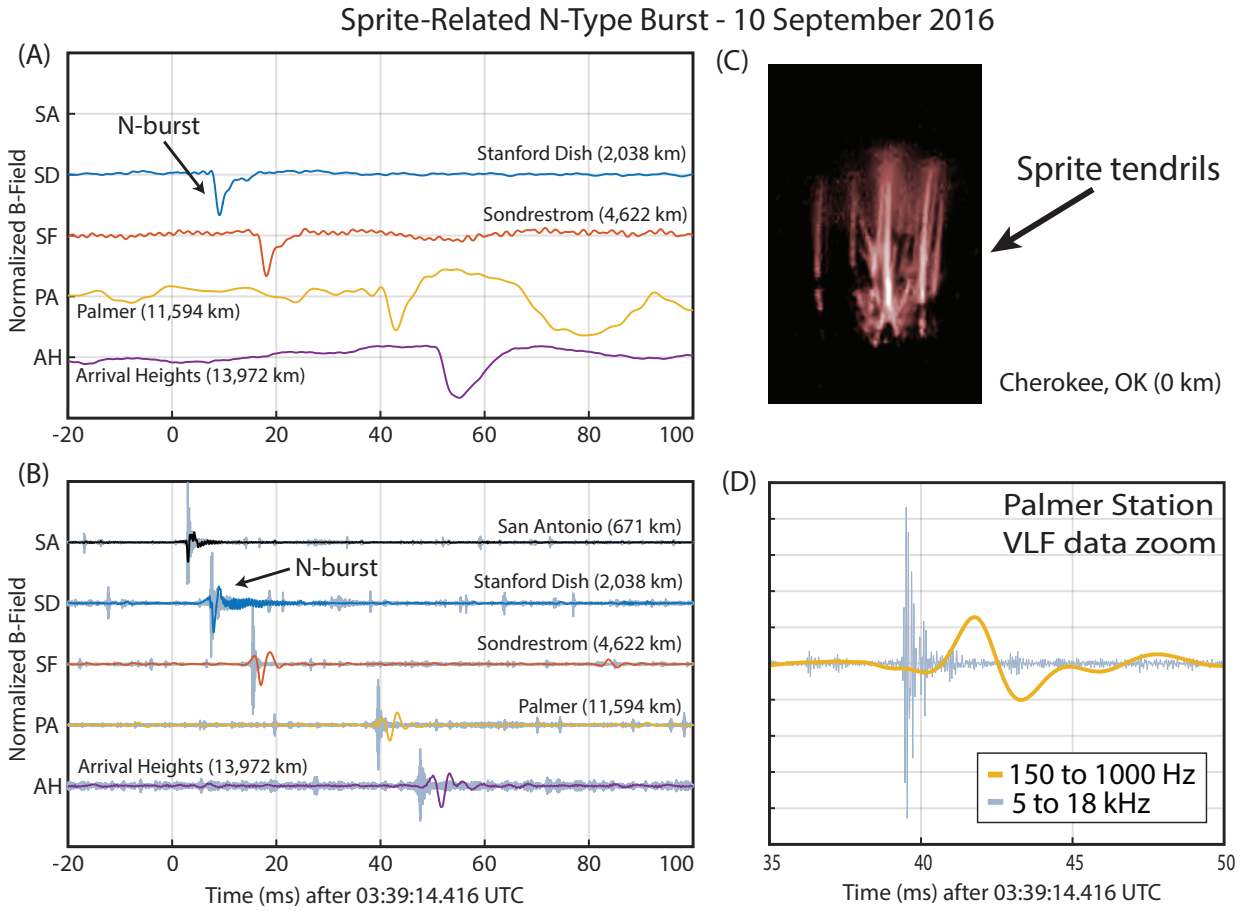

Figure 2-2. N-burst. Normalized azimuthal B-fields recorded by UF's (A) ELF receivers shown filtered from 5 to 300 Hz and (B) ELF/VLF receivers filtered from 150 Hz to 1000 Hz and from 5 to 15 kHz. Panel (C) shows the event photograph (credit: Thomas Ashcraft) and Panel (D) shows a close-up of the ELF/VLF transient received at Palmer Station, Antarctica.

wave propagates about the globe, as shown in Figure 2-2(A). The time axis of the signal is indexed relative to the onset time of the optical emission and the amplitude is normalized to the maximum amplitude in the window.

Substantial ELF and VLF energy are associated with this event as a large ELF-pulse is seen in the colored traces, and a large VLF-pulse is seen in the gray traces. Without applying a quantitative metric yet, we notice that in each of the bands, the ELF/VLF transient registers significantly above the noise floor.

As the wave propagates around the globe, the VLF component (gray trace) leads the

trailing ELF (colored trace) component as has been previously theorized [*Galejs et al.*, 1972, p. 310] [*Wait*, 1962; *Chapman et al.*, 1966; *Ogawa and Komatsu*, 2009] and observed experimentally [*Watson Watt et al.*, 1937; *Taylor and Sao*, 1970; *Brooks*, 1992; *Reising et al.*, 1999; *Van Der Velde*, 2010]. The dispersive nature of the Earth-ionosphere waveguide is well-understood: When the N-burst is measured by the nearest ELF receiver, (Stanford), the ELF and VLF components are aligned in time, but when the event is measured at Arrival Heights, 13.5 Mm away, the ELF component lags the VLF component by ∼10 ms.

Radio-location from a single station can be performed with a co-located measurement of the magnetic field and vertical electric field using the impedance method [*Burke and Jones*, 1995] or applying direction finding and sferic time-separation using a single station [*Koochak and Fraser-Smith*, 2020] or by using multi-station triangulation methods [*Füllekrug and Constable*, 2000; *Füllekrug et al.*, 2015]. We were able to identify the causative return stroke in NLDN data. We identified the corresponding N-burst by accounting for the expected ELF and VLF propagation delays from the reported time and place of the sprite observation. This method will be applied in the analysis of sprites, gigantic jets, and elves throughout the remainder of the chapter.

On 18 September 2016, a second N-burst associated with a sprite was observed and is shown in Figure 2-3. The sprite was photographed over Midland, Texas at 02:45:52.66 UT. NLDN records confirm a positive cloud-to-ground stroke at 02:45:52.60 UT, some 40 miles north (32.372° N, 102.231° W), with an estimated peak current provided by NLDN of 74 kA. An N-burst was identified by visual inspection of the ELF and VLF data shown in Figure 2-3(A). Again we point out the significant signal levels in all ELF and VLF bands, registering well above the noise floor. In both cases, the sprites are clearly associated with N-bursts by visual inspection.

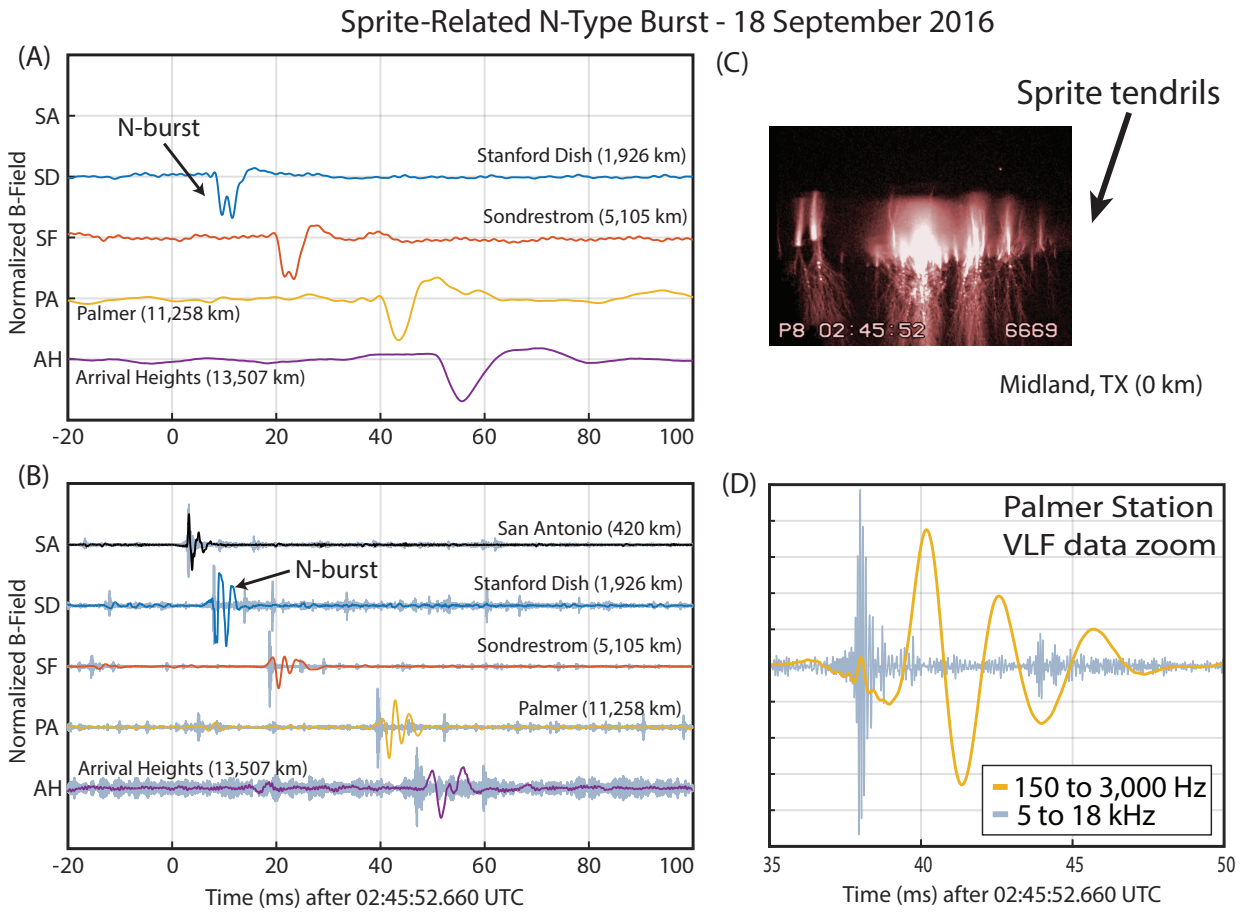

Figure 2-3. N-burst. Normalized azimuthal B-fields recorded by UF's (A) ELF receivers shown filtered from 5 to 300 Hz and (B) ELF/VLF receivers filtered from 150 Hz to 1000 Hz and from 5 to 15 kHz. Panel (C) shows the event photograph () and Panel (D) shows a close-up of the ELF/VLF transient received at Palmer Station, Antarctica.

2.3 Gigantic Jets and Q-Bursts

On 8 September 2016, Kevin Palivec, located in Hawley, Texas pointed his camera north toward Lubbock, Texas. At 01:25:39.315 UT, he recorded a gigantic jet with characteristic initial rapid development of the entire structure from cloud top to ionosphere, in a single frame, followed by a slow rising trailing jet seen clearly over the course of 12 frames (200 ms), as shown in Figure 2-4(C).

Figure 2-4(A,B) shows the ELF/VLF transient associated with this gigantic jet. The ELF component (A) is similar to that for the sprites. The VLF component (B), on the

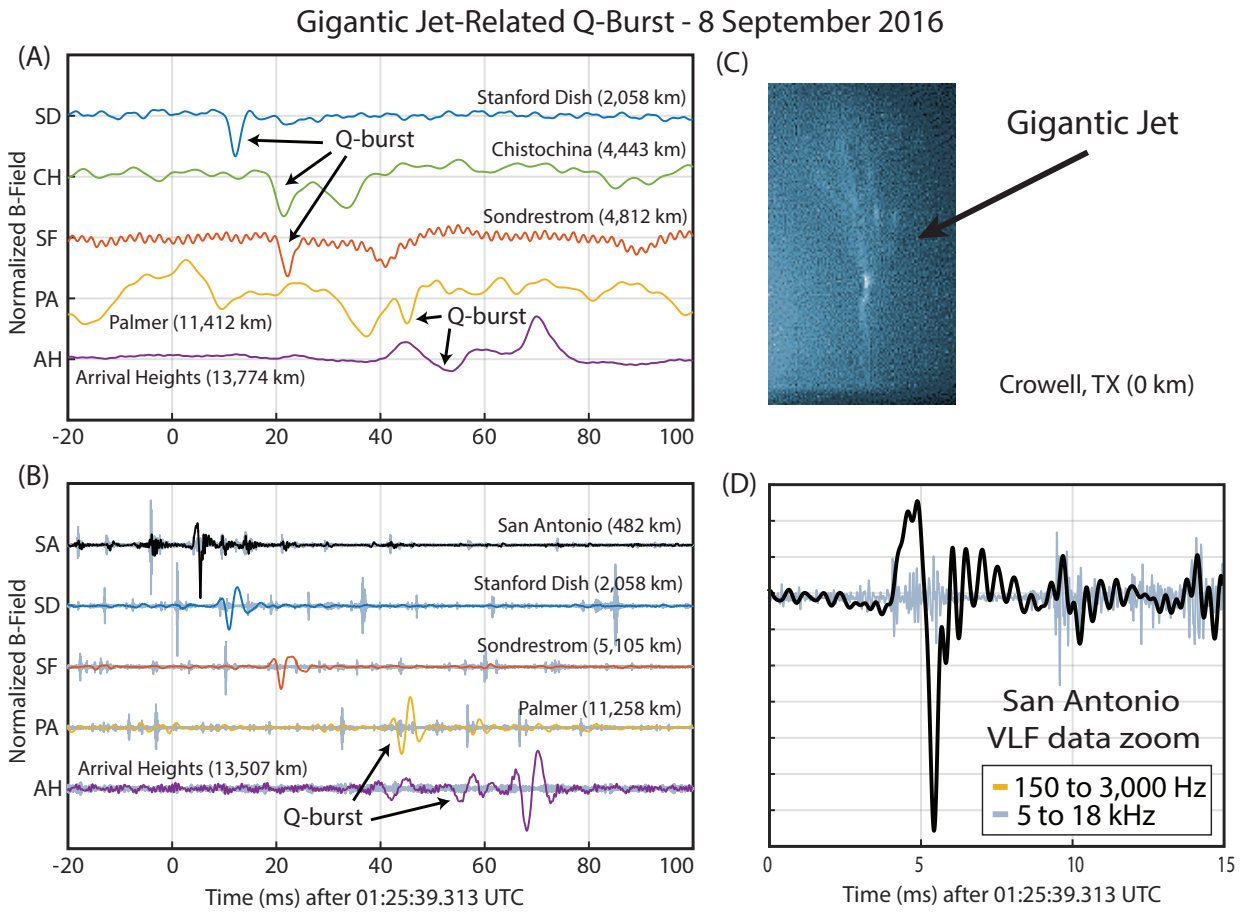

Figure 2-4. Q-burst. Normalized azimuthal B-fields recorded by UF's (A) ELF receivers shown filtered from 5 to 300 Hz and (B) ELF/VLF receivers filtered from 150 Hz to 1000 Hz and from 5 to 15 kHz. Panel (C) shows the event photograph (credit: Kevin Palivec) and Panel (D) shows a close-up of the ELF/VLF transient received at San Antonio, Texas (482 km distant).

other hand is dramatically different – very little VLF content is observed to propagate around the globe. Of particular interest are observations performed at San Antonio, Texas, a mere 482 km from the event. While a significant ELF (150-1000 Hz) component is present at San Antonio, the VLF (5 to 15 kHz) component is absent – a VLF component is not detectable even at such a close distance.

Following the nomenclature of Ogawa, the San Antonio recording falls into the category of a Q-flash, whereas more distant observations are classified as Q-burst measurements. Observations made at Chistochina, Sondrestromfjord, Palmer Station, and

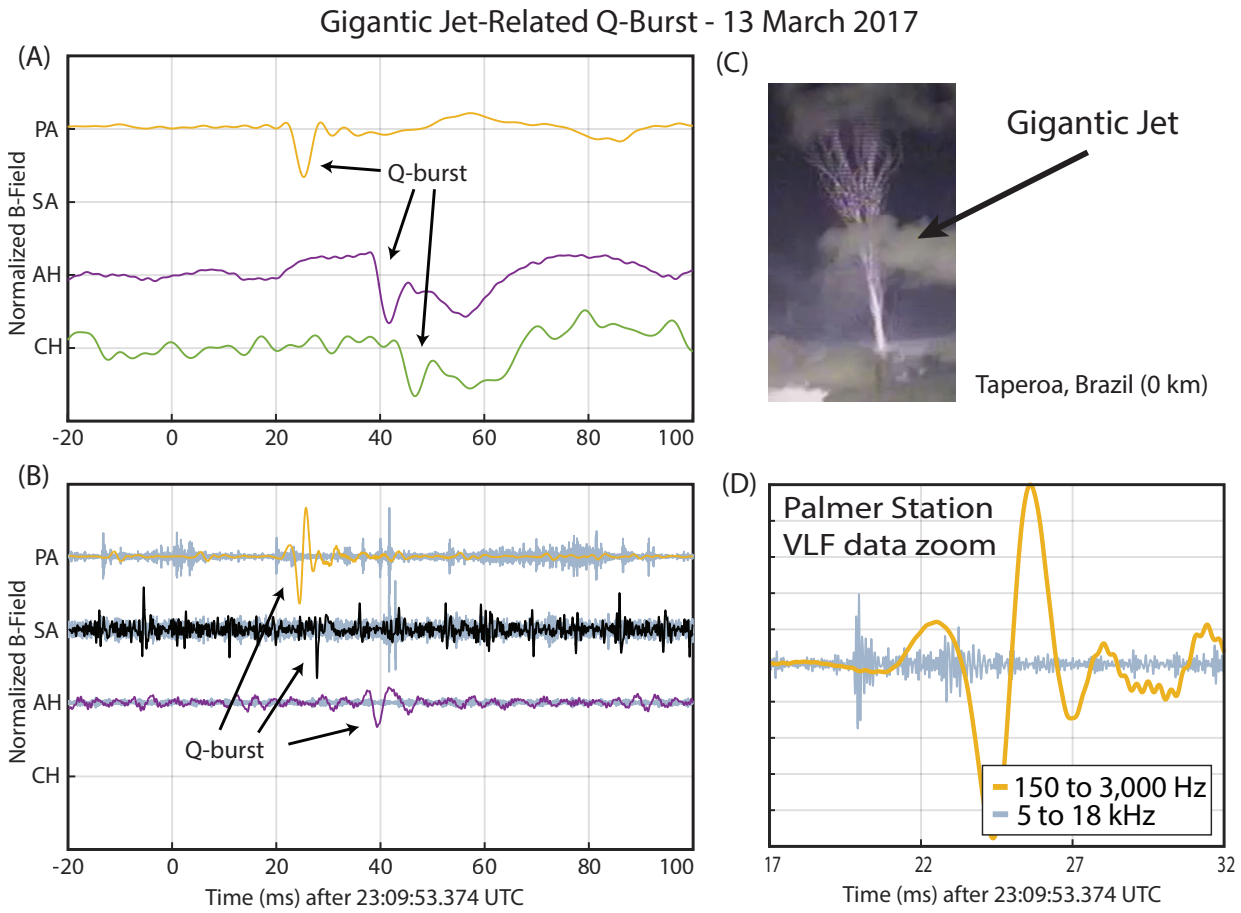

Figure 2-5. Q-burst. Normalized azimuthal B-fields recorded by UF's (A) ELF receivers shown filtered from 5 to 300 Hz and (B) ELF/VLF receivers filtered from 150 Hz to 1000 Hz and from 5 to 15 kHz. Panel (C) shows the event photograph () and Panel (D) shows a close-up of the ELF/VLF transient received at Palmer Station, Antarctica.

Arrival Heights all show a clear broadband signal in the ELF data and little to no companion propagating VLF signature.

A second Q-burst producing gigantic jet was observed over Taperoa, Brazil by BRAMON on 13 March 2017. A beautiful color image of this event is provided in Figure 2-5(C) along with the UF observations of ELF/VLF transients in Figure 2-5(A,B). The ELF component is observed to be well above the noise floor, whereas little to no accompanying VLF content is observed. By visual inspection, this event is classified as a Q-burst based on the presence of ELF content and the absence of VLF energy. There must

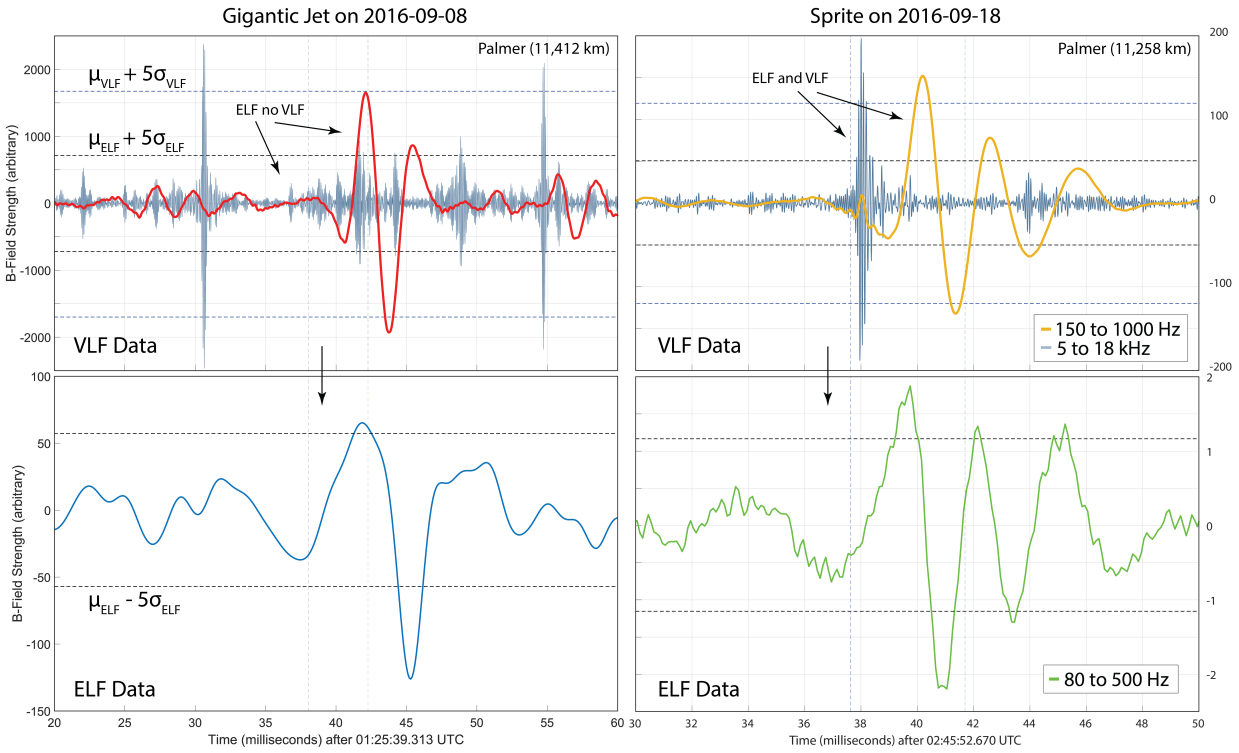

Figure 2-6. The ELF/VLF transients associated with a gigantic jet and a sprite observed at Palmer Station, Antarctica. 5σ thresholds demonstrate the characterization method.

be a threshold for this classification, however, because the VLF content is small, but not zero. Panel (D) shows the observations at Palmer Station, Antarctica, where the small VLF component is observed.

Based on the observations shown here, it is clear that gigantic jets are capable of producing Q-bursts. The explanation behind the difference in spectra produced is simple: gigantic jets form a longer channel of current, roughly 60-80 km, compared to typical cloud-to-ground lightning with a vertical extent of around 5-10 km and will more readily radiate larger wavelengths.

2.4 Sprites and Gigantic Jet Discussion

Based on visual inspection of the ELF/VLF transients, it appears that sprites are associated with N-bursts and gigantic jets are associated with Q-bursts. Without a quantitative metric, however, a determination for every event would need to be performed

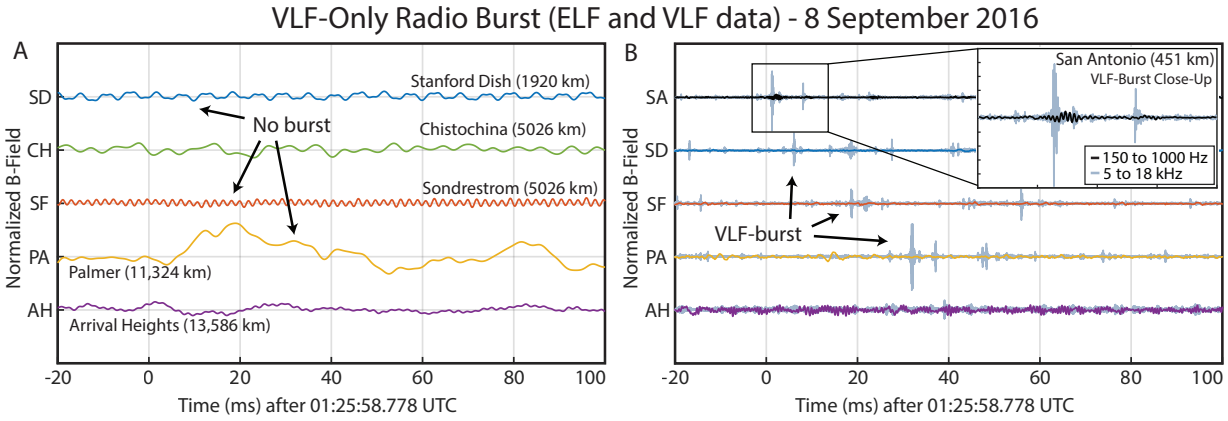

Figure 2-7. V-burst. Normalized azimuthal B-fields recorded by UF's (A) ELF receivers shown filtered from 5 to 300 Hz and (B) ELF/VLF receivers filtered from 150 Hz to 1000 Hz and from 5 to 15 kHz. The inset panel shows a close-up of the ELF/VLF transient received at San Antonio, Texas.

manually. In order to process a large number of events, it is clearly desirable to produce a method for identification that can be automated.

We begin by calculating a 1-second running mean (μ) and a 1-second running standard deviation σ for each band of interest (ELF and VLF). Detailed inspection of the data suggests that setting a $mu \pm 5\sigma$ threshold could perform well as a means to detect content within each band, meaning that when the data set deviates from the the mean by more than five standard deviations, we consider that a positive detection of signal content within the band.

Figure 2-6 shows the ELF/VLF transients observed with a gigantic jet and sprite. The $mu \pm 5\sigma$ thresholds are identified on the plots for reference. For the gigantic jet, the transients do not trigger the VLF detection threshold, but do trigger the ELF detection threshold, indicating the detection of a Q-burst. For the sprite, the transients trigger both VLF and ELF detection thresholds, indicating the detection of an N-burst.

The application of this algorithm to the entire data set observed on 8 September 2016 produced an interesting result: an extremely large number of ELF/VLF transient events with no ELF content and only VLF content. This third type of low frequency radio burst was neither investigated nor proposed by Ogawa. A VLF-only burst (or V-burst for short)

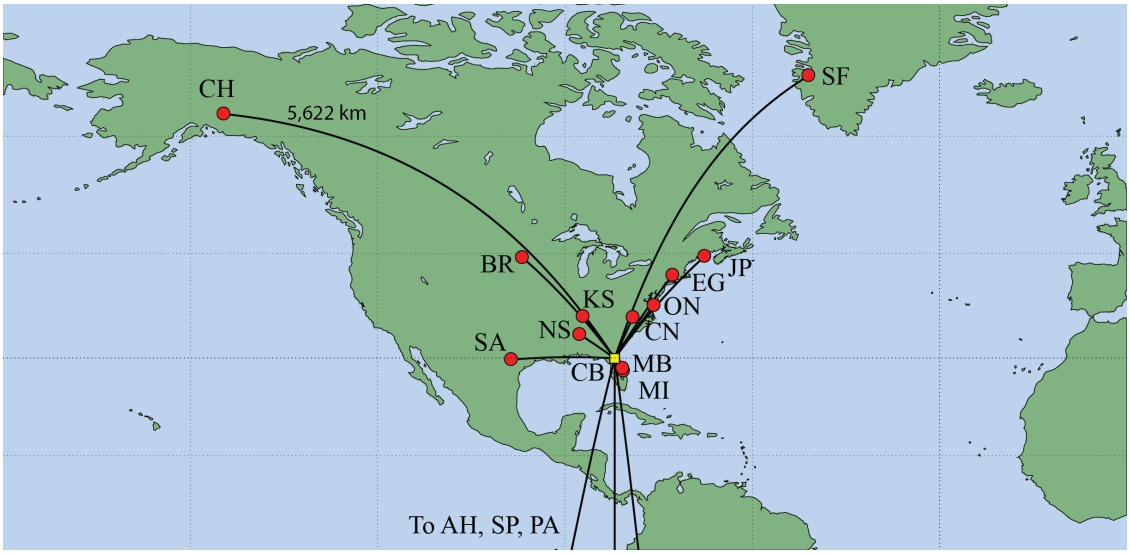

Figure 2-8. Map showing the propagation paths from the ICLRT in Starke, FL to the ELF/VLF receiver stations that were in operation during the 2016 rocket-triggered lightning campaign. The yellow square marks the trigger location.

is shown in Figure 2-7. It was observed at multiple stations with a significant VLF sferic pulse, with no associated ELF component. No causative lightning return stroke was identified in NLDN data in the region, but the radio event triangulated to the same region as the gigantic jet and was likely part of the same storm. A possible source for such an event could be an intracloud lightning discharge or CG lightning that was not detected by NLDN.

This very interesting observation led to an investigation of rocket-triggered lightning experiments previously performed at the International Center for Lightning Research and Testing (ICLRT) at Camp Blanding, Florida.

2.5 Rocket-Triggered Lightning and V-Bursts

The ICLRT performed rocket triggered lightning (RTL) experiments during the 2016 summer season. A total of 8 VLF stations and 4 ELF/VLF stations were in operation during this period. A map showing the great-circle path propagation path from the ICLRT trigger site to each of the receivers in this study is shown in Figure 2-8.

An example RTL V-burst is shown in Figure 2-9. Event UF16-06 was triggered at the

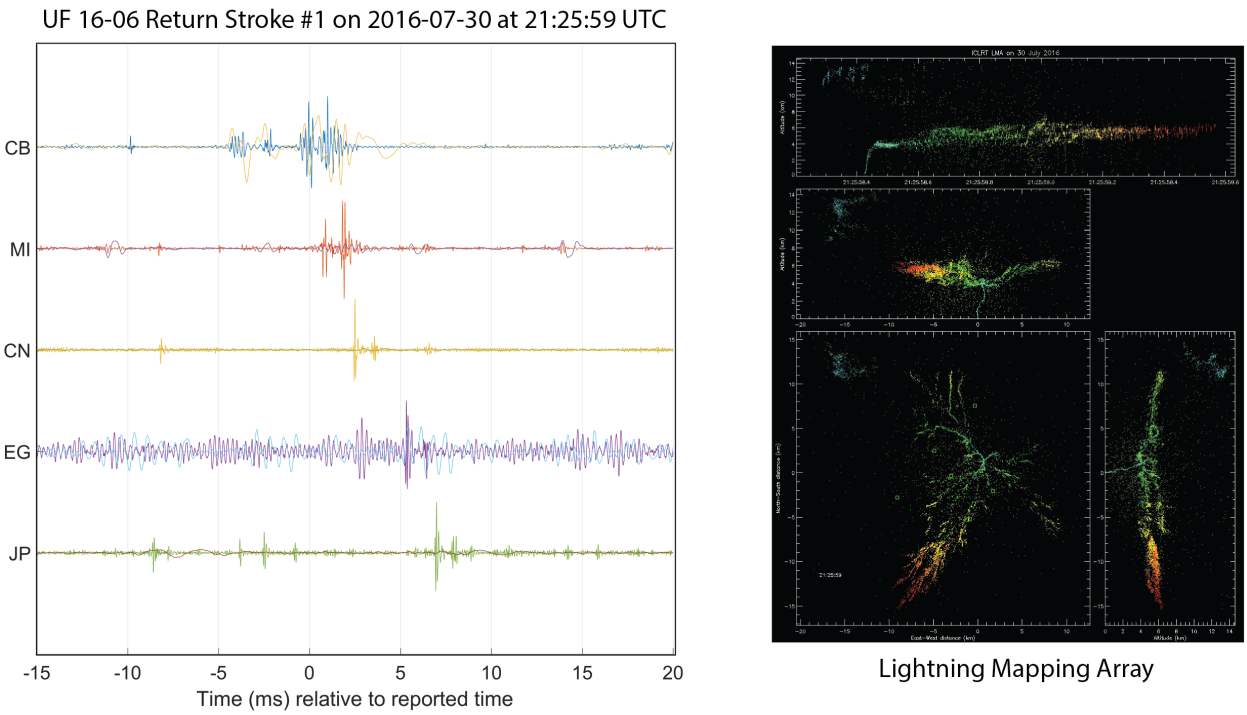

Figure 2-9. Rocket-triggered lightning V-burst. (left) The ELF/VLF transient produced by rocket-triggered lightning event UF 16-05 on 30 July 2016. (right) Lightning mapping array showing the lightning channel geometry at the ICLRT for event UF 16-05.

ICLRT on 30 July 2016 at 21:25:29 UT. The left panel shows the ELF band (150-2,000 Hz) and VLF band (3-15 kHz). The right panel shows the lightning channel geometry as provided by the Lightning Mapping Array (LMA) at the ICLRT. The time axis of the ELF/VLF data is aligned to time zero as the event trigger time. The time-delayed signal is shown propagating up the East-Coast VLF array from Camp Blanding (CB) to Melbourne, FL (MB), Chapel Hill, North Carolina (CN), East Granby, Connecticut (EG), and Jonesport, Maine (JP). These receivers were chosen to illustrate the unique ability the UF VLF array offers to monitor signal propagation along an array path. This event was observed at all global receivers but that data is not shown here.

A lightning flash composed of two return strokes was triggered at the ICLRT on 30 July 2016 at 21:18:09.825 UT and 21:18:09.912 UT respectively. The signal was detected by the UF ELF/VLF radiometers at Arrival Heights and Palmer Station in Antarctica and

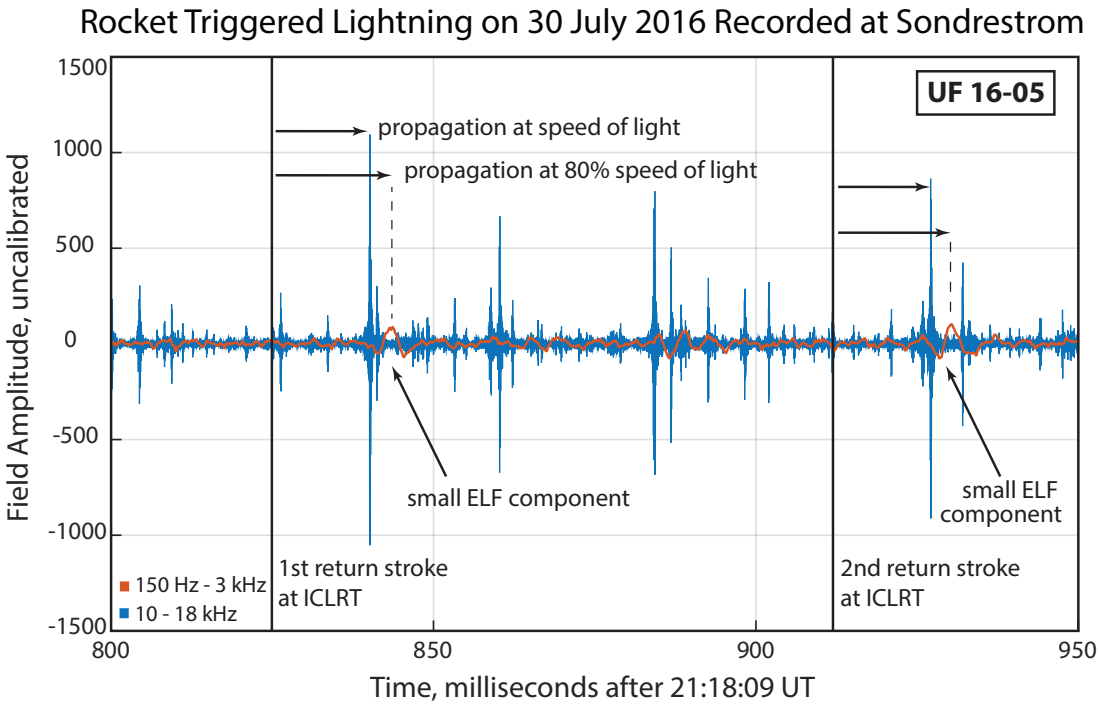

Figure 2-10. Two ELF/VLF transients launched by two return strokes during the UF 16-05 flash on 30 July 2016 and recorded at the ELF/VLF Station in Sondrestrom, Greenland.

in Sondrestrom, Greenland. Figure 2-10 shows the ELF/VLF data recorded at Sondrestrom in separate ELF and VLF bands. A large VLF sferic is clearly identifiable. Interestingly, a small ELF sferic was also detected. We applied the $\mu \pm 5\sigma$ threshold and determined a positive detection of VLF and a negative detection of ELF in both cases. Therefore, these two events were both classified as V-bursts.

In total, all 24 of the 24 rocket-triggered lighting return stroke events in this study produced V-bursts, when analyzed using the $\mu \pm 5\sigma$ detection threshold. Clearly, triggered lightning is strongly associated with V-bursts. At the same time, it is clear that a continuum of ELF energy exists: it is entirely within the realm of possibility that a different lighting return stroke could produce larger ELF components, resulting in an N-burst observation.

2.6 Summary and Discussion

In this chapter, we have presented two examples of sprites associated with N-bursts, and two examples of gigantic jets associated with Q-bursts. It makes logical sense that the longer channels of the gigantic jet, without an associated cloud-to-ground path, would radiate more powerfully in the ELF band, generating a Q-burst. At the same time, it is also logical that the strong cloud-to-ground lightning return stroke associated with the initiation of a sprite could produce the VLF component of the N-burst, while the conducting channels of the sprite itself could produce the ELF component. This perspective is consistent with the observations of sprite currents [*Cummer et al.*, 1998; *Reising et al.*, 1999; *Cummer et al.*, 2006], which were able to separate the N-burst or V-burst produced by the causative lightning flash from the Q-burst produced at ionospheric altitudes at the time of sprite brightening.

Most importantly, however, in this chapter we developed an algorithm for ELF/VLF transient characterization. The $\mu \pm 5\sigma$ threshold appears to work well distinguishing between transients associated with sprites and gigantic jets. As a result of this threshold definition, a new type of ELF/VLF transient was identified – the V-burst – and associated with typical cloud-to-ground and perhaps intracloud lighting discharges.

Certainly, this threshold metric requires further corroboration. Nevertheless, it appears that previous categorizations of ELF/VLF transients associated with TLEs were perhaps errant. Having identified a quantitative method to characterize ELF/VLF transient events in this chapter, the next chapter aims to evaluate the accuracy of the characterization method using a completely different, global data set provided by the ISUAL satellite.

CHAPTER 3
GLOBAL OBSERVATIONS OF ELF/VLF TRANSIENTS

In the previous chapter, a quantitative method for characterizing ELF/VLF transients was presented. As a result of that metric, it was shown that, contrary to the present narrative found in the literature [*Boccippio et al.*, 1995; *Williams*, 1998], gigantic jets tend to produce Q-bursts and sprites tend to produce N-bursts. The metric also helped to identify V-bursts, a new category of ELF/VLF transient associated with more typical lightning flashes. It is not yet clear, however, how well this metric works to identify specific TLEs on an independent data set.

In this chapter, the $\mu \pm 5\sigma$ metric for ELF/VLF transient detection and characterization is applied to a more diverse, global data set obtained from the ISUAL satellite, which identifies the time and location of TLE events observed from space. For each TLE event location and time identified by ISUAL, the ELF/VLF transient detection and characterization method is applied, providing a means to evaluate whether radio-based event identification agrees with the ISUAL team's manual event identification. In the end, the analysis of ELF/VLF observations in conjunction with reports from the ISUAL satellite reinforces the conclusions of Sections 2.2 and 2.3 and suggests that gigantic jets are predominantly associated with Q-bursts and sprites are predominantly associated with N-bursts. Another interesting result of the analysis indicates that elves are observed with roughly 50%-50% V-bursts and N-bursts, indicating that significant VLF (or higher frequency) spectral content is required to produce the event.

This chapter proceeds by describing the experimental context for ISUAL observations, presenting a representative comparison of ELF/VLF transients and ISUAL observations, calculating the average spectral content of ELF/VLF transients observed to be associated with specific types of TLEs, and statistically analyzing the data base. It concludes by reflecting on the observed relationships between TLEs and ELF/VLF transients.

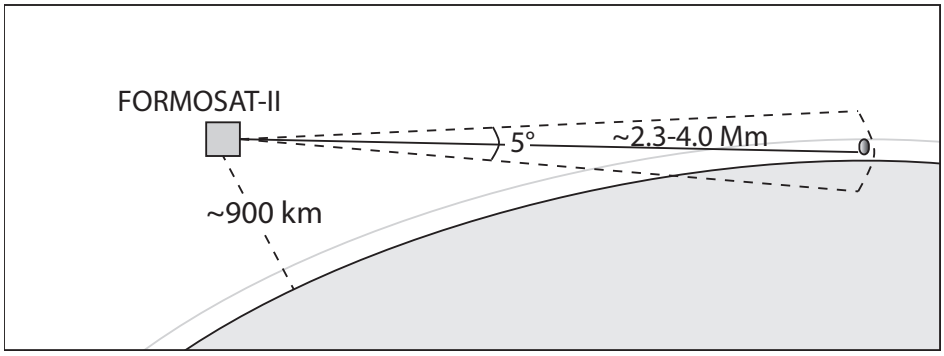

Figure 3-1. A diagram of the ISUAL limb-view of Earth.

3.1 Spaced-Based Observations of TLEs

The Taiwanese National Space Organization satellite, FORMOSAT-II, recorded transient luminous events using the Imager of Sprites and Upper Atmosphere Lightning (ISUAL) payload during the observation period of this study from 2014 to 2016. The satellite was positioned in sun-synchronous orbit and completed 14 complete revolutions about the Earth every day [*Lee et al.*, 2013]. The ISUAL payload consists of a CCD sensor used to photograph the events as well as a set of array and narrowband photometers that are used to trigger the camera and capture faster processes in the event [*Chern et al.*, 2003; *Frey et al.*, 2016]. All instruments cover the same approximate 20° × 5° field of view as is shown in Figure 3-1 [*Chen et al.*, 2008; *Kuo et al.*, 2009]. Events are catalogued with a trigger time, an estimated event initiation time, and an inferred effective ground location. The supplied photograph series shows six sequential snapshots in time at 180 frames per second with 512 x 80 pixel resolution [*Chen et al.*, 2008]. A typical example of a gigantic jet, sprite, and elve observed by ISUAL are shown in Figure 3-2. Note that the typical gigantic jet develops over all 6 frames, while the typical sprite develops over 2-3 frames, and the typical elve occurs during just one frame. The ISUAL team classifies TLEs manually by inspection of the event morphology and development. The data collected by this instrument and analyzed by the ISUAL team provides a long-term repository of upper-atmosphere phenomena over the last fifteen years [*Hsu et al.*, 2017].

The timing and location information associated with ISUAL optical observations of

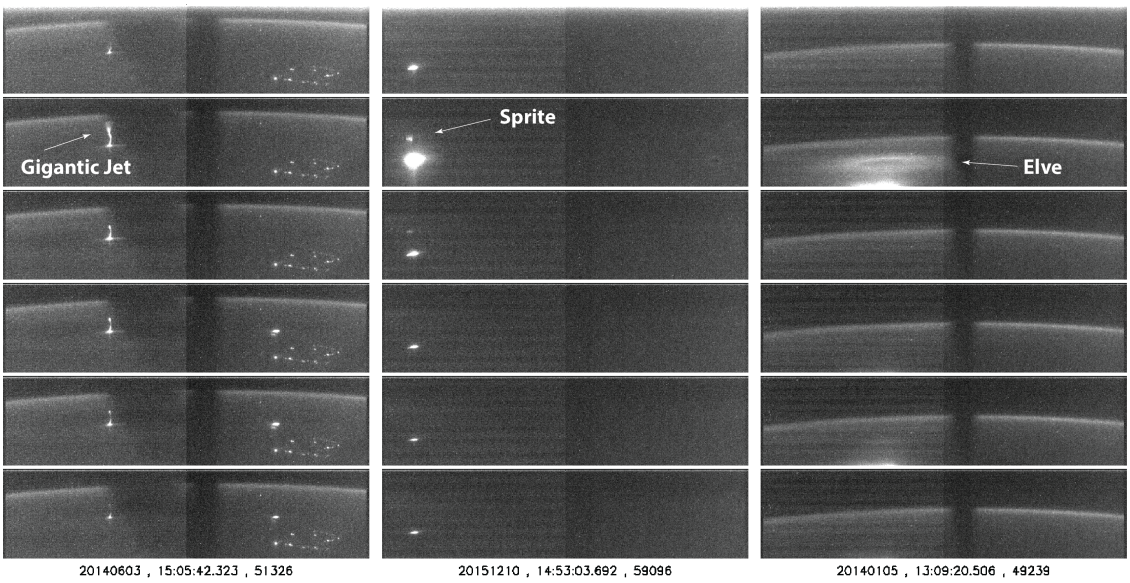

Figure 3-2. Typical Observations of a gigantic jet, sprite, and elve by the ISUAL satellite.

gigantic jets, sprites, elves, and "sprites with elves" are used as a starting point to search for radio bursts in the University of Florida's ground-based, global ELF/VLF receiver array data set. Over 4,900 events were detected by ISUAL during the period between 2014 and 2016 and a total of 19 gigantic jets, 308 sprites, 4,659 elves, and 11 "sprites with elves" were observed. The geographic distribution of these sprites and gigantic jets is shown in Figure 3-3, indicating significant geographic diversity with events identified over the Carribean, South America, Africa, Malaysia, and more.

3.2 Radio Burst Classification of ISUAL-Observed TLEs

A typical example of radio observations made in association with a sprite and a gigantic jet are shown in Figure 3-4. The left-hand column shows data from a sprite on 11 April 2016 occurring at 21:55:12.568 UT over central Africa (4.9°N, 14.49°W), and the right-hand column shows data associated with a gigantic jet on 11 December 2015 occurring at 13:17:40.865 UT over Papua New Guinea (4.18°S, 141.19°W). From top row to bottom we show (1) a photograph of the event provided by ISUAL, (2) low-ELF (5−300 Hz) time domain radio observations, (3) ELF/VLF time domain radio observations filtered to a high-ELF band (150 Hz−1000 Hz) and a VLF band (3−18 kHz), and (4) a

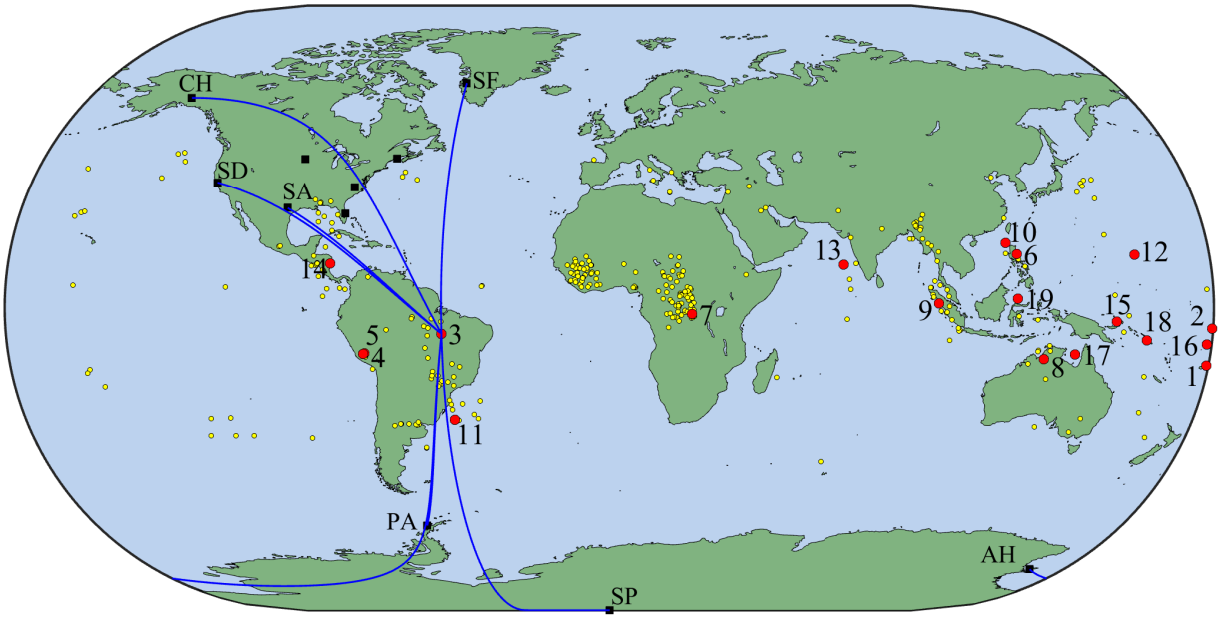

Figure 3-3. The ISUAL-identified gigantic jets during the period 2014 to 2016 are marked as red circles and numbered 1 through 16 on this map. Sprites are marked as yellow circles. University of Florida VLF receivers are shown as black squares.

broadband ELF/VLF spectrogram observed in Sondrestrom, Greenland. For both events, a transient burst of energy is visible in both the low-ELF and the high-ELF bands. The sprite (left) also carries a significant amount of energy in the VLF band while the gigantic jet (right) does not. Applying the $\mu \pm 5\sigma$ metric identifies an N-burst in association with the sprite and a Q-burst in association with the gigantic jet. The difference in spectral content between events is particularly clear in the spectrograms on the bottom row of the figure. The sprite has a large swath of VLF energy content at 20 ms with an accompanying broad pulse in the ELF range that is slightly delayed in time. The gigantic jet case also features this broad pulse of ELF energy at 35 ms, but it does not offer similarly broad spectral content in the VLF range above 3 kHz in the 30−40 ms window.

An example of a V-burst associated with the occurrence of an elve is shown in Figure 3-5. The elve event appears in the second panel of the time series photograph as a large diffuse glow above the illuminated cloud just below the airglow region. Fewer radio observations were available on this day, with only two low-ELF and four ELF/VLF

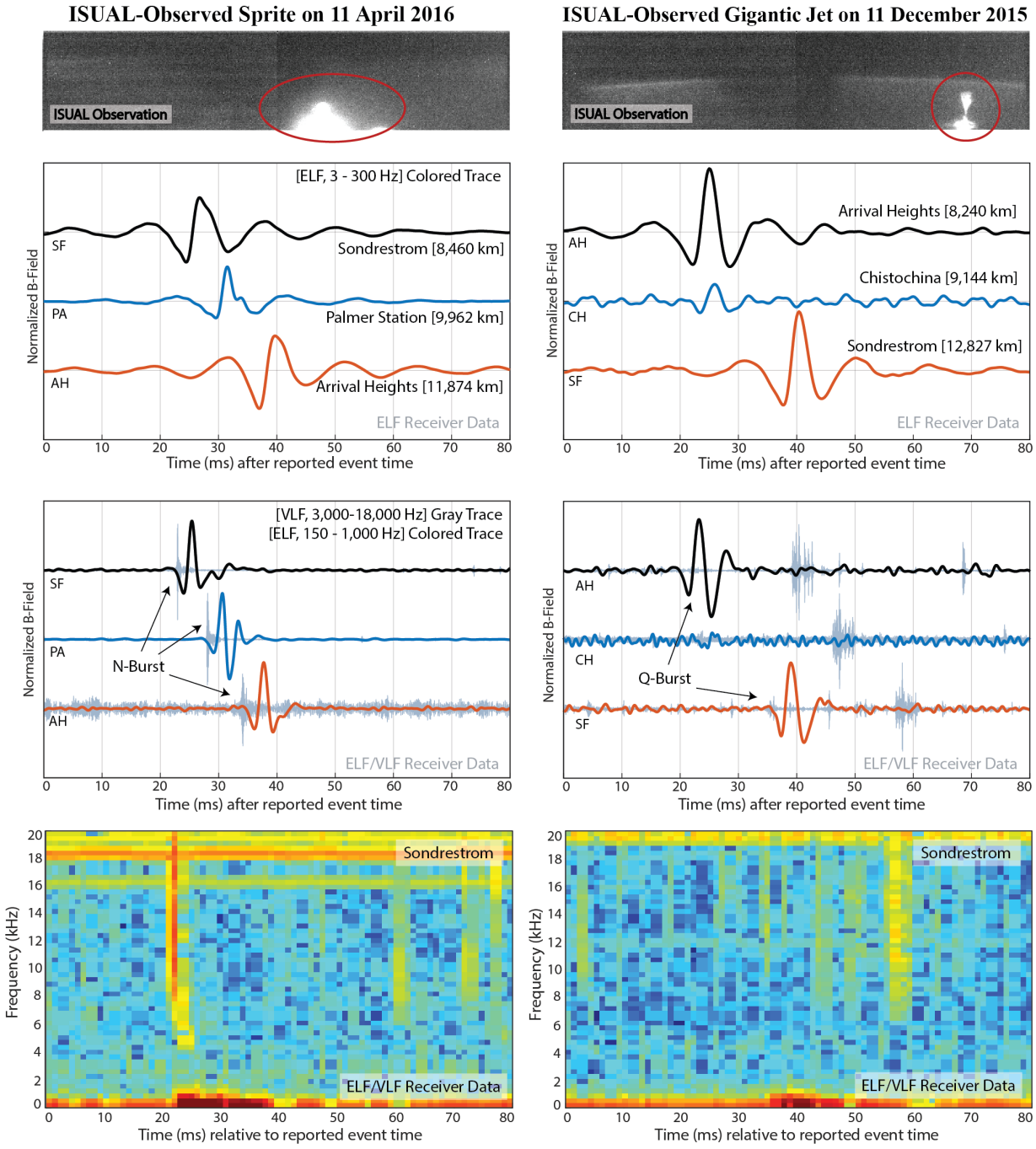

Figure 3-4. An example recording of a Q-burst associated with a gigantic jet and a characteristic N-burst associated with a sprite. Both events were identified by ISUAL and are shown measured by three UF ELF/VLF stations around the globe.

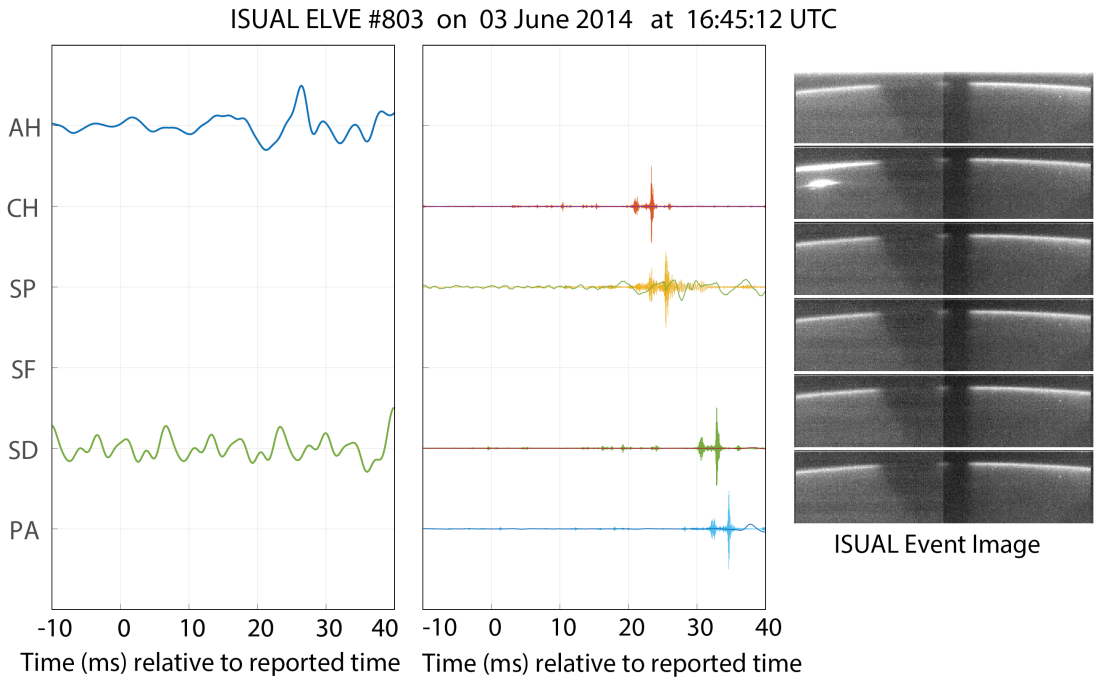

Figure 3-5. An example recording of a V-burst associated with an elve observed by ISUAL.

receivers operational. Nevertheless, a transient burst is evident in the ELF/VLF data at Chistochina, South Pole, Stanford, and Palmer Station. Only a small ELF signal that does not meet the $\mu \pm 5\sigma$ threshold is present at Palmer Station. This radio signature was classified as a V-burst, and is generally representative of the V-bursts associated with elves. A significant percentage of elves were also observed together with N-bursts, however. In those cases, the radio observations are similar to those presented in Figure 3-5, but the ELF components are simply more pronounced. Pointedly, however, the ISUAL observations confirm that in these cases, the ELF components were not accompanied by a visible optical flash in the ionosphere that could be mistaken for a sprite or a gigantic jet. Because we do not expect the elves-related ionospheric disturbance to radiate at ELF frequencies, we interpret these observations as evidence that both the ELF and VLF components of the N-burst were generated by the causative cloud-to-ground lightning return stroke itself.

3.3 Application to the ISUAL Database

Of the over 4,900 events identified by ISUAL, 19 were identified as gigantic jets, 308 as sprites, 4659 as elves, and 11 as sprites and elves. For this study, all of the gigantic jets

Table 3-1. Record of analyzed ISUAL-identified events, UF-confirmed events, and UF-confirmed radio bursts used in this report.

	Total ISUAL TLEs	Selected ISUAL TLEs	Clear Optical Examples		Identifiable Radio Bursts	
	Count	Count (method)	Count	Percent	Count	Percent
Gigantic Jets	19	19 (all)	15	79 %	7	47 %
Sprites	308	108 (Palmer)	55	51 %	37	67 %
Elves	4,659	50 (week)	18	36 %	13	72 %
Sprites+Elves	11	11 (all)	6	55 %	3	50 %

and sprites with elves were selected because there were a small number of these events. A total of 108 of 308 sprites were selected in order to include the sensitive Palmer Station low-ELF observations, which did not become available until May 2015. With over 4,000 elves to choose from, we selected a 1 week period when a large number of the global ELF/VLF receivers were operational, reducing the number of elves analyzed to 50.

From these examples, we identified those events whose white-light morphology was clear and unmistakable (Clear Optical Examples); leaving 15 gigantic jets, 55 sprites, 18 elves, and 6 "sprites with elves." For the remaining events, we determined whether a clear radio burst was observed in ELF/VLF data within the expected time window of arrival at three or more receiver sites (Identifiable Radio Bursts). In the end, a total of 7 gigantic jets, 38 sprites, 13 elves, and 3 "sprites with elves" are selected as the sample set of this study. Table 3-1 shows the number of events that satisfied each stage of the event selection process, lists the number of Clear Optical Examples as a percent of the Selected ISUAL TLEs, and lists the number of Identifiable Radio Bursts as a percent of the Clear Optical Examples that were analyzed.

The Clear Optical Examples with Identifiable Radio Bursts from Table 3-1 were classified as either N-bursts, Q-bursts, or V-bursts based on the relative spectral content in the ELF/VLF radio transient, using the $\mu \pm 5\sigma$ threshold. An event was classified as an N-burst if three or more sites observed the radio transient with ELF content above the $\mu \pm 5\sigma$ threshold and three or more sites observed the radio transient with VLF content

Table 3-2. Distribution of radio bursts associate with TLE observations for optically confirmed events with distinguishable radio signature.

	Bursts	N-Burst		Q-Burst		V-Burst	
	Total	Count	Percent	Count	Percent	Count	Percent
Gigantic Jets	7	0	0 %	7	100 %	0	0 %
Sprites	37	36	97 %	1	3 %	0	0 %
Elves	13	6	46 %	0	0 %	7	54 %
Sprites+Elves	3	3	100 %	0	0%	0	0 %

above the $\mu \pm 5\sigma$ threshold. An event was classified as a Q-burst if three or more sites observed the radio transient with ELF content above the $\mu \pm 5\sigma$ threshold and fewer than three sites observed the radio transient with VLF content above the $\mu \pm 5\sigma$ threshold. A V-burst was registered if fewer than three sites observed the radio transient with ELF content above the $\mu \pm 5\sigma$ threshold and three or more sites observed the radio transient with VLF content above the $\mu \pm 5\sigma$ threshold. The requirement for 3 observations at greatly separated sites to affirm event detection mitigates the impact of potentially significantly different propagation conditions that might occur around the globe. As an example, in many cases, the VLF portion of the signal was nearly absent at the South Pole site due to ice-related VLF attenuation. The support of multiple observations at sites around the globe allow for the event to be properly classified.

The results of this analysis applied to the Clear Optical Examples with Identifiable Radio Bursts are shown in Table 3-2. Gigantic jets are exclusively observed as Q-burst, and sprites are almost exclusively observed as N-bursts, as are "Sprites+Elves." Elves are nearly evenly distributed between N-bursts and V-bursts.

Once again, it makes logical sense that the longer channels of the gigantic jet would radiate more powerfully in the ELF band, generating a Q-burst. It is also still logical that the strong cloud-to-ground lightning return stroke associated with the initiation of a sprite could produce the VLF component of the N-burst, while the conducting channels of the sprite itself could produce the ELF component of the N-burst. Similarly, it is logical that elves are associated with strong VLF content, regardless of the ELF content, and that

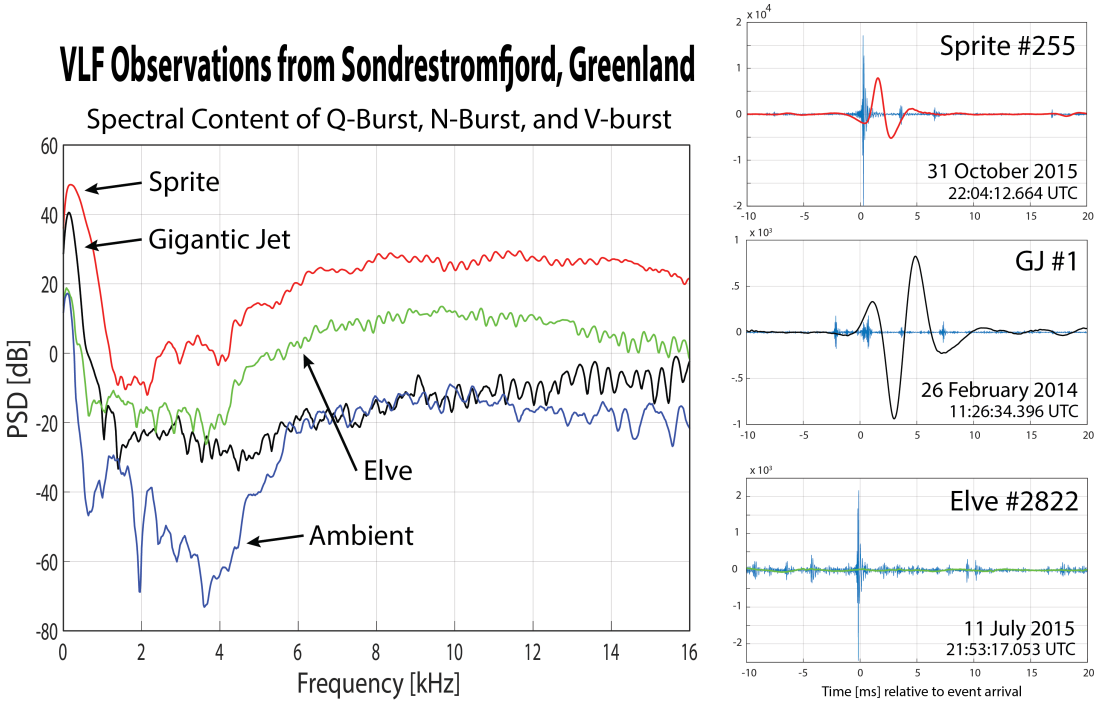

Figure 3-6. ELF/VLF power spectral densities associated with sprites, gigantic jets, and elves, relative to the ambient field. Associated time-domain waveforms are shown in the right panels.

"Sprites+Elves" would be observed as N-bursts due to the presence of the sprite. These more complete observations, for events occurring at vastly different locations around the globe, are perfectly consistent with the conclusions presented in Chapter 2.

We now turn our attention toward determining whether the current ELF/VLF transient detection algorithm can be improved, using ISUAL observations.

3.4 TLE-Associated ELF/VLF Power Spectral Densities

In this section, we evaluate the spectral content of the ELF/VLF transients associated with particular types of TLEs, as observed by ISUAL. Figure 3-6 shows the power spectral density (PSD) from 0 Hz to 16 kHz for four specific ISUAL-identified TLE observations. All four events shown here were observed at the Sondrestromfjord receiver station in Greenland. The time domain waveform for each of the three events is shown to the right of the PSD plot; the ambient case is not shown. The differences between the ELF/VLF transient spectra associated with these TLEs are clear and align with the

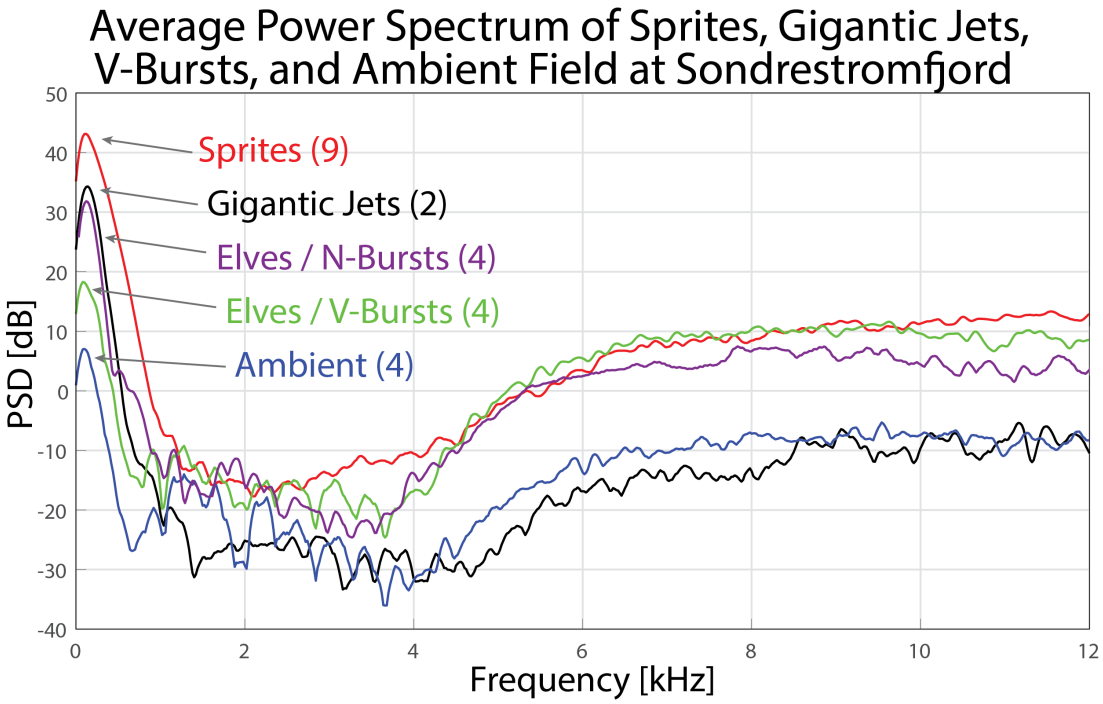

Figure 3-7. Averaged ELF/VLF PSDs for ISUAL-detected sprites, gigantic jets, and elves, compared to the ambient field.

definitions of N-bursts (sprite), Q-bursts (gigantic jet), and V-bursts (elve, in this case). In fact, the $\mu \pm 5\sigma$ threshold corresponds to a PSD threshold of ~14 dB above the ambient. ELF and VLF content for ELF/VLF transient identification and characterization can be clearly evaluated using this metric. For instance, the V-burst is essentially at the same level as the ambient below 1 kHz and approximately 20 dB above the ambient above 5 kHz, the N-burst is approximately 25 dB above the ambient below 1 kHz and approximately 40 dB above the ambient above 5 kHz, and the Q-burst is approximately 20 dB above the ambient below 1 kHz and essentially at the same level as the ambient above 5 kHz. It appears that perhaps even more divisions could be identified in both the ELF and VLF ranges.

The average ELF/VLF spectra detected at Sondrestromfjord and associated with sprites, gigantic jets, and elves by ISUAL are shown in Figure 3-7. Because calculation of the PSD involves an integration, it is necessary to exclude events from the Clear Optical Examples with Identifiable Radio Bursts if the time domain ELF/VLF waveform exhibits interference from another transient within the integration window. While this limitation

reduces the number of included events, the result are still instructive. The 9 sprites clearly produced, on average, an N-burst, with ELF content 35 dB above the ambient and VLF content 20 dB above the ambient. The 2 gigantic jets produced, on average, a Q-burst, with ELF content 25 dB above the ambient, and VLF content at essentially the same level as the ambient. The 4 elves that were visually associated with a V-burst, averaged, unsurprisingly, to a V-burst, with ELF content only 10 dB above the ambient, and VLF content 20 dB above the ambient. Similarly, the 4 elves that were visually associated with an N-burst, averaged, unsurprisingly, to a N-burst, with ELF content 25 dB above the ambient, and VLF content 20 dB above the ambient. These average observations support the conjecture that perhaps more divisions are identifiable in the ELF range, but appear to identify only one threshold in the VLF range. There certainly appears to be a potential way to differentiate N-bursts associated with sprites and those associated with elves, based on the magnitude of ELF content, but to state so with confidence would require a larger sample set with clear optical observations.

For the purposes of this work, we conclude that the PSD analysis shows that the $\mu \pm 5\sigma$ threshold is excellent for detecting and characterizing ELF/VLF transients. It also shows that the PSD method itself does not perform well when ELF/VLF transients overlap and is not ideal for the automatic application to a larger data set. Instead, this work indicates that band-pass filtering to distinct ELF and VLF bandwidths and applying a detection algorithm using the $\mu \pm 5\sigma$ threshold is a superior method for automation. At this point, we recognize that the ELF and VLF bandwidths may be different at different receiver sites, depending on the noise environment. Based on the observations presented thus far, it appears that a low-ELF bandwidth of $5-300$ Hz, a high-ELF bandwidth of $150-1000$ Hz, and a VLF bandwidth of $5-15$ kHz are well suited to avoid noise and interference issues at most receiver sites.

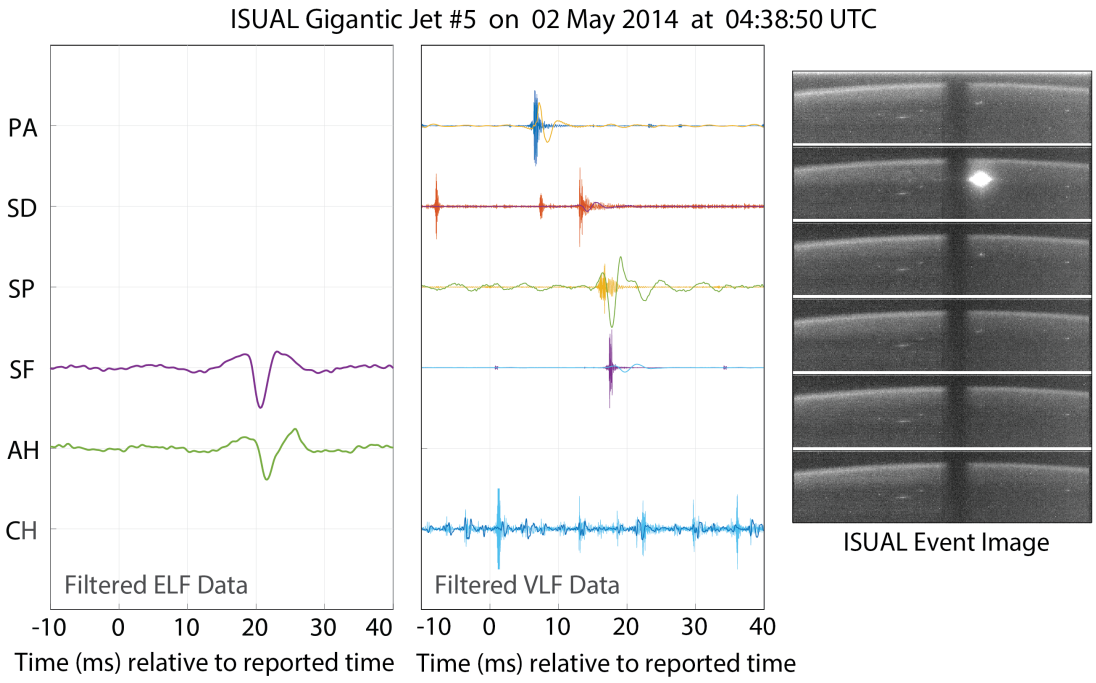

Figure 3-8. An example of a gigantic jet that was identified by ISUAL that was excluded from this study due to morphology and duration considerations.

3.5 Investigation Outliers

To lend credence to these conclusions, it is worth a short investigation into the examples removed from the statistical data set.

Of the 19 gigantic jets identified by ISUAL, all 19 were initially chosen for analysis. Only 15 of the 19 events were clearly gigantic jets. For example, event number 5, shown in Figure 3-8, was rejected from this study due to the lack of clear definition in the event morphology and the uncharacteristically short duration of the event. Normally, a gigantic jet develops over several milliseconds [*Van Der Velde et al.*, 2019] and would appear on multiple frames of the deck of images, as shown in Figure 3-2. Of the 15 remaining events, only 7 events had conclusive radio signatures at the expected time of arrival where the burst was distinguishable above the noise floor at a minimum of three sites. Among the 8 cases for which the event was not classifiable, 3 were excluded because fewer than three receiver sites detected the event and 5 events were excluded because the radio signature was not clear at any site.

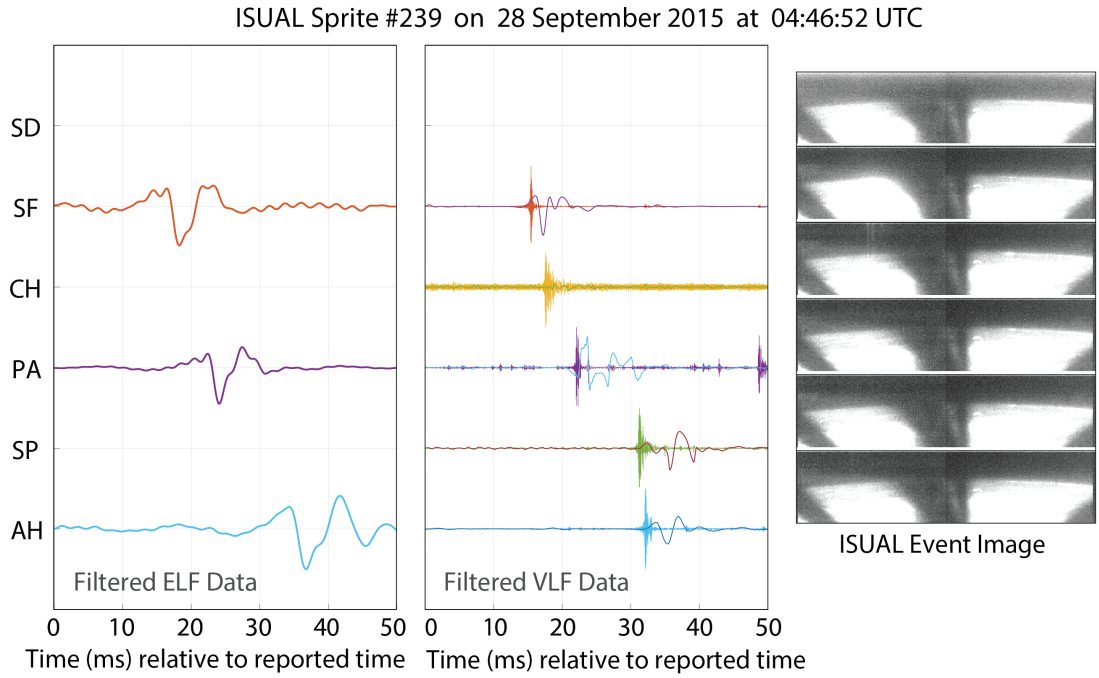

Figure 3-9. An example of a sprite that was identified by ISUAL that was excluded from this study due to morphology considerations.

To maximize the number of low-ELF observations of the 308 sprites identified by ISUAL, 108 sprites were selected for the study at a time after the Palmer Station low-ELF receiver was installed. From these remaining 108 events, 55 events were optically confirmed to be sprites while the remaining 53 events were not clearly identifiable. For instance, event 239 shown in Figure 3-9 was excluded from the study as the event was not clearly identifiable as a sprite. However, the results of the study suggest that this event, which produced an N-burst, may actually be a sprite hidden in the saturated region of the image. Clear radio signatures were identified at a minimum of 3 receiver sites in 37 of the 55 analyzed events.

Of the 4,569 elves identified by ISUAL, only 50 events were selected for analysis. All of the events during the week of 03-10 June 2014 were selected as many receiver sites were in operation at this time. Elves result from the EMP heating of the lightning discharge and are not believed to carry a significant current and are not expected to radiate. Of the 50 selected events, only 18 events were clearly identifiable in the ISUAL white light images.

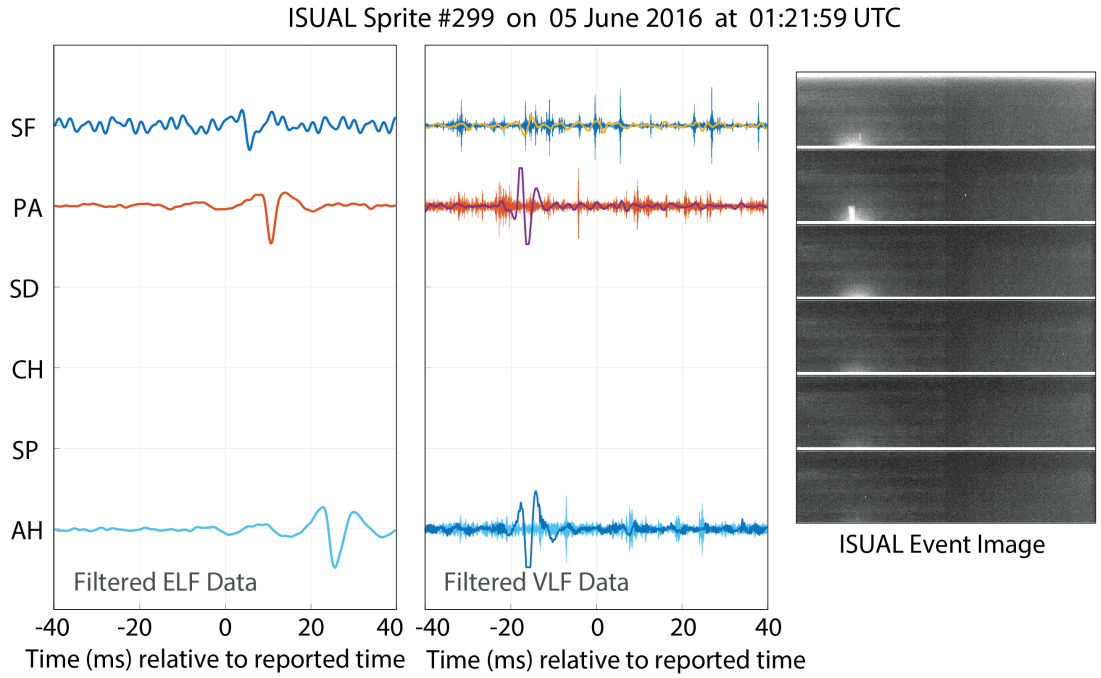

Figure 3-10. The sprite identified by ISUAL that produced a Q-burst.

Of these 18 events, 13 were observed with classifiable ELF/VLF radio bursts at a minimum number of 3 receiver sites.

Of the 11 "sprites with elves" that were observed by ISUAL, only 6 events were clearly identifiable in the white light images, and only 3 events had identifiable ELF/VLF radio bursts. All 3 "sprites with elves" produced N-bursts. This is not a surprising result as N-bursts were overwhelmingly observed with sprites.

Lastly, Figure 3-10 presents the outlier sprite event that was observed as a Q-burst. The white light image is indeed consistent with sprite morphology, and the radio observations are consistent with a Q-burst. At the same time, only three radio receivers were operating for this event, and the radio classification may benefit from additional independent observation locations. Nevertheless, this event may also indicate that although sprites are dominantly associated with N-bursts, some small percentage of sprites might produce ELF/VLF transients detected as Q-bursts. In this context, the delayed sprites discussed in Chapter 1 become important. While the causative lightning return stroke could produce a V-burst or an N-burst, the optical brightening of the sprite may align with

the observed Q-burst. For this particular case, we inspected the data 200 ms preceding the event for a V-burst or N-burst that triangulates to the same approximate location and found 3 V-bursts at −57 ms, −96 ms, −102 ms. Perhaps the delayed sprite interpretation is correct in this case, but sprites are produced by active thunderstorms, and it would not be unusual for such a thunderstorm to generate several V-bursts in this time frame. Therefore, until better information is available, we have decided to classify the ELF/VLF transient associated with this sprite as a Q-burst.

3.6 Summary of ISUAL and ELF/VLF Observations

The statistics on ELF/VLF radio observations of satellite-detected transient luminous events presented herein confirm and expand upon the conclusions presented in Sections 2.2 and 2.3. Gigantic jets radiate almost exclusively in the ELF band resulting in a high number of observed Q-bursts. In this study, Q-bursts were observed almost 1-to-1 with gigantic jets. Sprites are primarily associated with N-bursts but have also been observed on one occasion in association with a Q-burst. In this study, 97% of sprites produced N-bursts. Interestingly, both N-bursts and V-bursts were observed in association with elves. This is not unexpected, as elves are produced by heating of the ionosphere by the lighting electromangetic pulse, and this heating is more efficient at higher VLF frequencies.

Having identified the best ELF/VLF transient characterization technique to apply to large data sets, the next chapter analyzes an entire week of ELF/VLF transient observations and quantitatively evaluates their relative contributions to the Schumann Band.

CHAPTER 4
ANALYSIS OF SCHUMANN BAND EXCITATION

In Chapters 2 and 3, a method was identified for the detection and classification of ELF/VLF transients. The method was applied to show that Q-bursts are strongly associated with gigantic jets, N-bursts are strongly associated with sprites, and V-bursts are strongly associated with typical lightning and elves-related lightning, without regard to whether the lightning consisted of intra-cloud or cloud-to-ground discharges. Some complications were identified, particularly when the radio signatures for multiple events overlap, or when a sprite is significantly delayed from the causative lightning flash. These complications notwithstanding, the identified detection and classification algorithm appears to be generally reliable, and it can be automated.

In this chapter we automate the detection and classification algorithm and apply the technique to a 1-week-long data set from the University of Florida's global ELF/VLF receiver array. All detected ELF/VLF radio transients are characterized as either a Q-burst, an N-burst, or a V-burst, and an analysis of global occurrence rates ensues. The work leverages Vaisala's GLD360 data set, which provides global lightning geolocation and timing information. The GLD360 data set is also used to estimate the distance to the source for an observed event, allowing the estimation of the power radiated into the Earth-ionosphere waveguide by the event's source. As a result, we are able to estimate the relative contribution of sprite events, gigantic jet events, and regular lightning events to the Schumann Resonance Band below 50 Hz.

4.1 Description of the Experiment

The University of Florida's global ELF/VLF receiver array (see Figure 1-18) has recorded ELF and ELF/VLF data sets nearly continuously since 2015. For this study, one week of data from the array on 4−10 August 2016 was selected because the largest number of receivers were operating as expected. The ELF/VLF data set is used for transient signal detection and classification. The ELF data set is then used to estimate the excitation of the Schumann Cavity.

Analysis is greatly simplified by use of Vaisala's GLD360 data set. Vaisala's National Lightning Detection Network (NLDN) has provided lightning detection services with high accuracy in the United States for over three decades. The NLDN has recently been expanded to provide coverage around the globe with the GLD360 system. GLD360 provides a detection efficiency of 80% in the Northern Hemisphere but offers substantially reduced efficiency in the Southern Hemisphere. The GLD360 data set provides information on the lightning type, strength, and polarity, as well as an inferred location within 2.5 km and timing within 1 µs [*Said et al.*, 2013]. It registers events using observations in the 5−15 kHz band, but then provides geolocation analysis using a waveform bank that extends down to 800 Hz [*Said et al.*, 2010]. Vaisala provided a list of every event detected around the world for the week of 4−10 August 2016.

ELF/VLF transients detected by UF's global ELF/VLF receiver array are associated with a GLD360 return stroke, yielding the location and timing of the source. This information enables the algorithm to account for the attenuation and propagation of the signal and better estimate the energy injected into the Schumann Cavity.

4.2 Event Detection and Classification

The essential components of the detection and classification algorithm described in the previous chapters is maintained here, with some modifications for practical implementation.

UF's global ELF/VLF receiver array data set is first used to identify ELF/VLF transients. The process is depicted graphically in Figure 4-1. The ELF/VLF data from each site is filtered to a high-ELF band of 150 Hz−2 kHz and a VLF band from 3−15 kHz. For each band, a moving 1-minute average (μ) and 1-minute standard deviation (σ) are calculated and used to identify impulses. Signal samples that exceed the $\mu \pm 5\sigma$ threshold are registered as potential detections. Each data sample that exceeds the $\mu \pm 5\sigma$ threshold is then associated with an impulse (there are likely to be multiple samples per impulse), and the timing of the impulse is estimated by finding the sample with the largest deviation

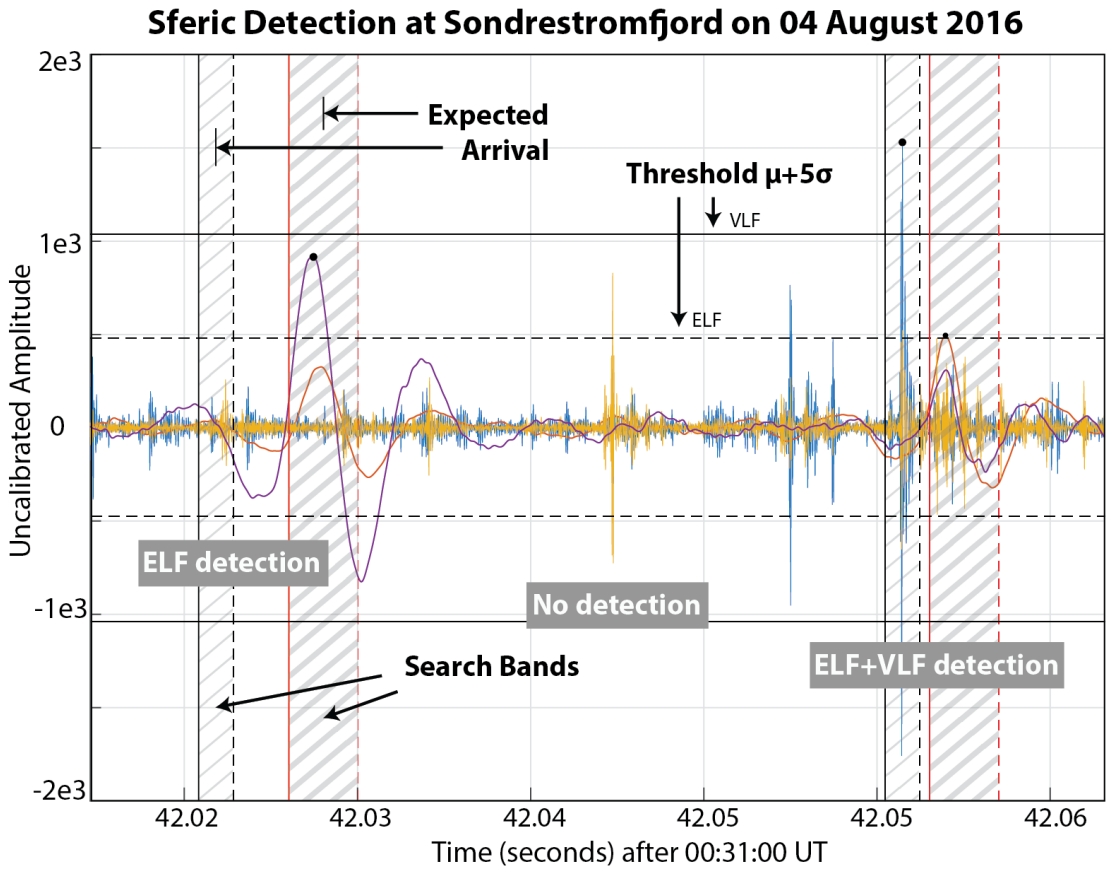

Figure 4-1. Single-site sferic detection process at the Sondrestrom VLF station.

from the mean within N ms ($N = 5$ ms for VLF and 10 ms for high-ELF). Each resulting impulse time is recorded for both high-ELF and VLF bands.

In Figure 4-1, the VLF amplitude threshold is shown as a solid horizontal line above and below the mean. The ELF amplitude threshold is shown as a dashed horizontal line above and below the high-ELF mean. The expected arrival time window for the VLF portion of the signal is marked by light hatching. The expected arrival window for the high-ELF portion of the signal is delayed slightly in time and is marked by heavier hatching. The first of the two sferics highlighted contains significant ELF energy, with the peak field marked by a black dot, but does not register VLF energy. The second highlighted sferic contains both ELF and VLF band energy, with the peaks of both fields marked with a black dot. Single-site classification of these events would register a Q-burst and an N-burst. Multi-site classification depends on the detection of high-ELF and VLF

energy at all of the receiver sites. Note that in between these two events are sferics which are clearly above the noise floor, but do not surpass the detection threshold used in this study and are therefore not considered in this analysis.

In previous chapters, this analysis was performed on the transverse fields, the calculation of which involved rotating the signals in post-processing. For large data sets, it is not tractable to digitally rotate and calculate the transverse field for every individual sferic. For this reason, the algorithm is applied separately to the the North-South and East-West channels. While this method reduces the detection efficiency slightly for signals arriving from, say, 45° (plus integer multiples of 90°), we do not consider this to be a major problem. One could rotate the signals 45°, repeat the analysis, and take the union of the results, but this was not done for this study.

Once the high-ELF and VLF transients have been identified at each site in the UF network and the event arrival times are logged, the GLD360 timing data is leveraged to perform single-site and multi-site event classification analysis. For each detected event listed in the GLD360 data base, the expected time of arrival is calculated for each ELF/VLF receiver site using the GLD360 source timing and accounting for a propagation velocity of 99% the speed of light for VLF and 80% the speed of light for high-ELF. The source to receiver distance is calculated using the GLD360 source location and the known receiver location. A detection is registered for a given GLD360 event when the predicted time of arrival is within 1 ms of the independently measured transient detection for the VLF band and within 2 ms for the high-ELF band. Observation windows containing more than one event are discarded. These selection windows account for any variation in the propagation speed and any inaccuracies in the GLD360 timing and location reporting. A 1 ms delay at VLF amounts to a 300 km shift in ground distance. A 2 ms delay at ELF amounts to a 480 km shift in ground distance. An event is only successfully categorized if it has been detected with proper timing at the majority of sites.

Having completed the description of the detection algorithm, we now describe our

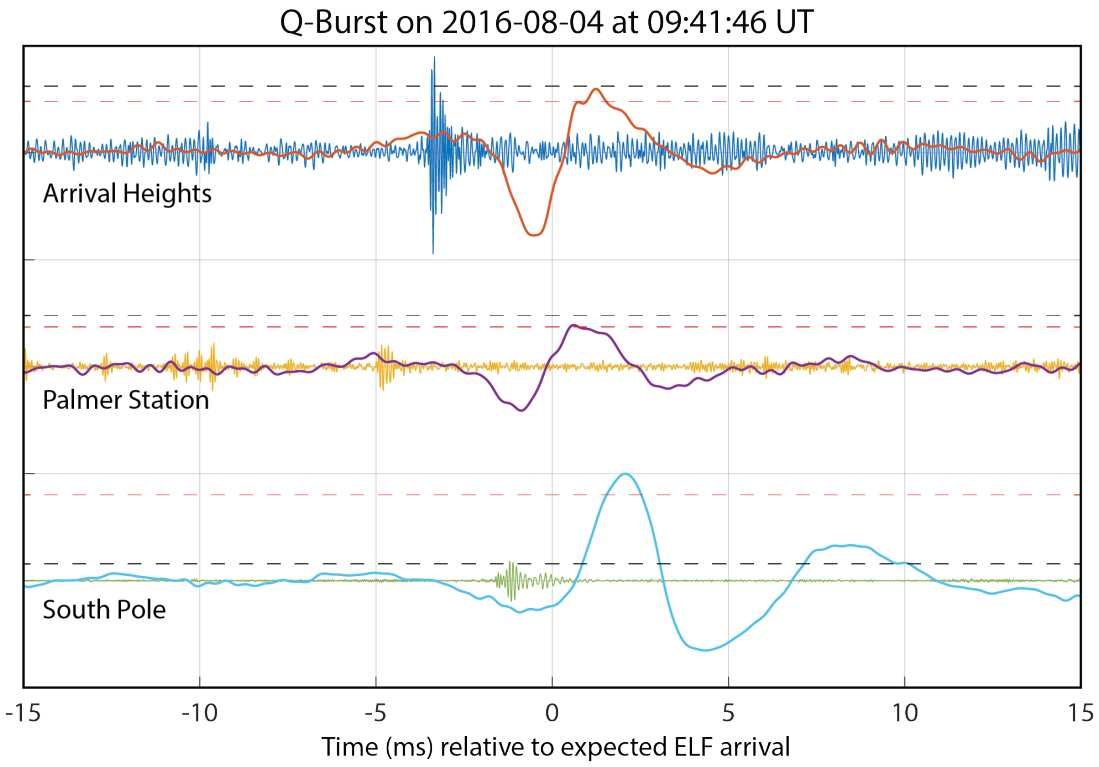

Figure 4-2. Q-Burst detection with GLD360 timing and location information

quality control efforts. An inspection of classified events was manually performed across the one week of observations. For each type of burst, 100 events were randomly selected to confirm the automated processing classification. Events were confirmed to be correctly classified when the event arrived in the observation window with correct triangulation timing.

An example of a correctly classified Q-burst is shown in Figure 4-2. The propagation delay to the receiver, assuming an 80% speed of light propagation velocity, has been removed from the timing of the signal. Notice that there is a detectable ELF component across all three sites. The VLF component at Arrival Heights appears near the arrival time of the ELF component, but it does not follow the event across multiple sites. Because the majority of sites register no VLF energy and the majority of sites register high-ELF energy with the right timing, we determine that this event has been properly classified as a Q-burst.

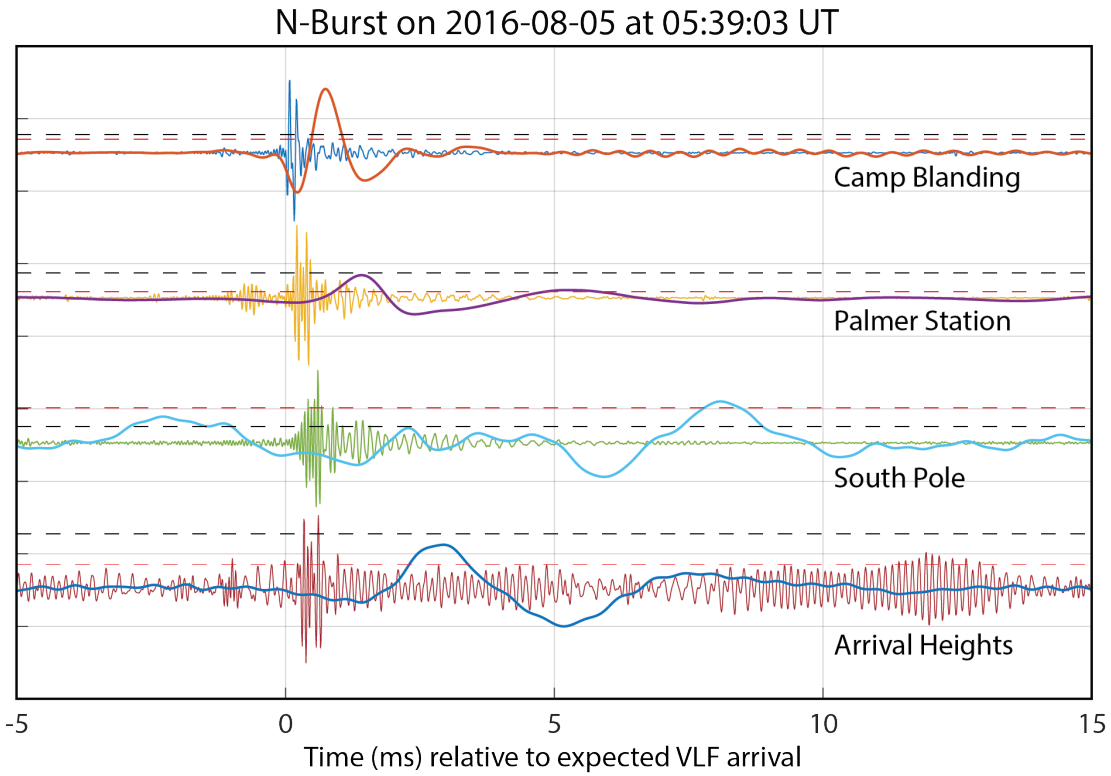

Figure 4-3. N-Burst detection with GLD360 timing and location information

An example of a properly classified N-burst is shown in Figure 4-3. In this case, the VLF propagation delay from source to receiver is subtracted at each site, so that some accumulating delay in the high-ELF band is expected. Events are sorted by their distance from the event with the closest site here being Camp Blanding, Florida and the furthest being Arrival Heights, Antarctica. A VLF sferic is detected across all 4 sites. All but one site (South Pole) shows a detectable high-ELF component as well. Because the majority of sites register VLF energy with the right timing, and the majority of sites register high-ELF energy with the right timing, we determine that this event has been properly classified as an N-burst. Note that single-site observations at South Pole would not have properly characterized this event.

An exemplary V-burst is shown in Figure 4-4. The speed of light delay is subtracted from the timing of all signals. A significant VLF component is distinguishable at all sites with the proper timing, and an ELF component is not detected at any site. Because the

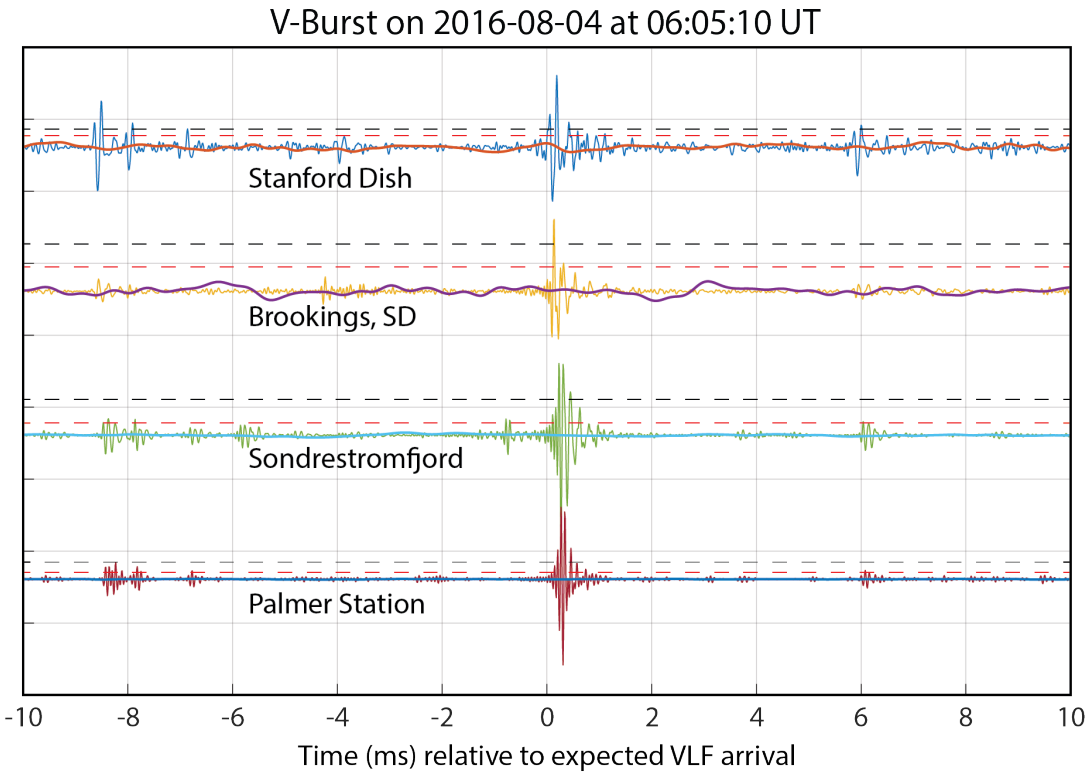

Figure 4-4. V-Burst detection with GLD360 timing and location information

majority of sites register VLF energy with the right timing, and the majority of sites do not register any high-ELF energy, we determine that this event has been properly classified as a V-burst.

In rare cases, however, some transients arrive within the proper window of arrival, but clearly do not triangulate to the same source. This phenomenon is depicted in Figure 4-5. Three ELF pulses appear above the detection threshold within the ±2 ms time window, but they do not have the proper alignment to triangulate to the GLD360 source location. The data is shown sorted in order of distance from source from top to bottom, and the high-ELF propagation delay has been removed. It is likely that an unrelated transient coincidentally produced a high-ELF pulse at Brookings within the observation window. As a result, the algorithm detected a Q-burst, but rather than a 3-station detection, it is actually a 2-station detection, which is still technically a Q-burst. We highlight this case because the pulses do not seem to perfectly triangulate to the GLD360 source location,

raising some concern, but not enough concern to exclude from the database.

Of the 100 Q-bursts selected, 94 were confirmed to be correctly identified, although 20 had triangulation timing issues consistent with the example shown in Figure 4-5, and 6 appeared to be N-bursts by visual inspection. Of the N-bursts randomly sampled, 100 were confirmed to be correctly identified, although 8 events had triangulation timing issues. Of the 100 V-bursts analyzed, 100 were confirmed to be correctly identified, although 4 events had triangulation timing issues.

Overall, these are excellent detection results, although some attention must be paid to the triangulation issues raised. Additionally, we determine that single site event classification is not advisable. An event that contains both ELF and VLF band content at a single site may appear to be an N-burst, but it is possible that the components do not track to the same source location. Multiple station observations are required to correctly classify events, and a minimum number of 3 stations is highly recommended.

Having described the detection and classification algorithm and evaluated its performance using spot checks, the next section presents occurrence rate results.

4.3 ELF/VLF Transient Occurrence Rates

With the detection algorithm in place, the burst occurrence rates can be calculated. A summary of single-station results applying this classification scheme over one 24-hour period of data on 04 August 2016 at each site is reported in Table 4-1. Classifying events based on single site observations can be misleading, and that is the point of including this table. Table 4-2 shows the total number of bursts that were identified during the week using the multi-station analysis. Comparing the "04" row with the numbers in Table 4-1 reveals enormous discrepancies. Q-bursts are over-estimated by a factor of 10 or 20 at some sites; N-bursts are over-estimated by a factor of 4 in some cases. Multi-site detection is key for the accurate classification of these bursts.

Table 4-2 summarizes the event detection findings using multi-station analysis for the week. The last row shows the average number of bursts per day by burst type. The results

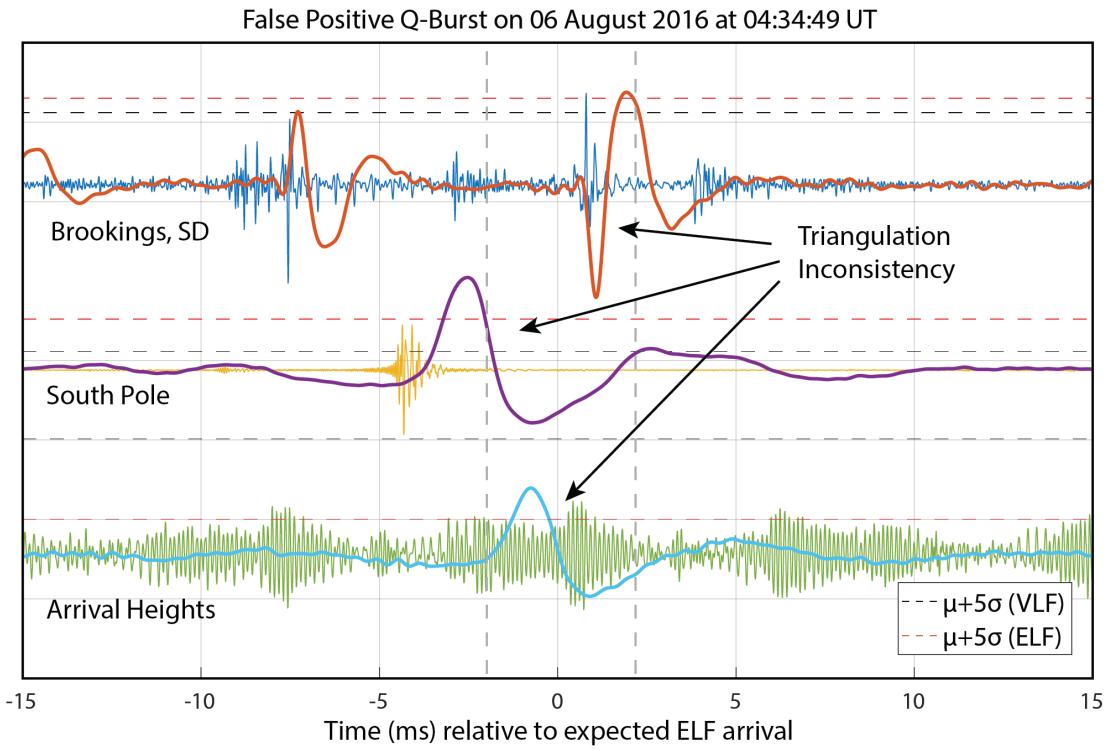

Figure 4-5. Q-Burst false positive detection with GLD360 timing and location information.

closely match reported occurrence rates from *Ogawa and Tanaka* [1967]. On average, 3,054 Q-bursts (2.1 per minute), 71,426 N-bursts (49.6 per minute), and 2,054,870 V-bursts (23.8 per second) are observed daily. It is clear that V-bursts occur far more frequently than N-bursts and Q-bursts. V-bursts are observed approximately 29 time more frequently than N-bursts, and N-bursts are observed approximately 23 times more frequently than Q-Bursts. At the same time, many more events remain unclassified. One might be tempted to multiply the observed rate for classified events by the total number of events (classified+unclassified), which yields 9,479 Q-bursts (6.6 per minute), 221,684 N-bursts

Table 4-1. Distribution of ELF/VLF energy identified at six stations on 04 August 2016.

	AH	CH	PA	SD	SF	SP
ELF Only	37,614	69,420	28,494	23,535	29,260	40,751
ELF + VLF	32,151	60,153	38,464	217,871	135,646	26,831
VLF Only	1,955,178	1,588,069	1,972,399	2,033,773	1,212,190	1,238,403
Not Classified	4,123,735	4,567,897	4,109,321	3,873,499	4,654,536	4,842,693
Total	6,148,678	6,285,359	6,148,678	6,148,678	6,031,632	6,148,678

Table 4-2. Distribution of ELF/VLF energy detected at multiple sites on 04 August 2016.

	Q-Burst		N-Burst		V-Burst		Not Classified	
	Count	Percent	Count	Percent	Count	Percent	Count	Percent
04	3,323	0.05 %	54,125	0.86 %	2,051,196	37.63 %	4,176,715	66.45 %
05	2,492	0.04 %	51,937	0.83 %	2,013,401	32.36 %	4,154,071	66.77 %
06	3,550	0.05 %	80,729	1.09 %	2,224,812	29.90 %	5,116,010	68.90 %
07	2,790	0.05 %	69,736	1.03 %	2,075,794	30.59 %	4,637,022	68.34 %
08	3,093	0.05 %	97,742	1.62 %	1,965,255	32.60 %	3,963,257	65.73 %
09	2,477	0.05 %	74,569	1.17 %	1,843,739	29.11 %	4,412,731	69.67 %
10	3,656	0.05 %	71,144	0.99 %	2,209,815	30.77 %	4,896,718	68.19 %
Avg	3,054	.05 %	71,426	1.08 %	2,054,870	31.09 %	4,479,503	67.78 %

(153.9 per minute), and 6,377,690 V-bursts (73.8 per second). Such an analysis is likely valid for V-bursts, where the primary reason for rejection is simply because its event window overlapped with another event's. For N-bursts and Q-bursts, rejection occurs more frequently when the signals are below the ELF detection threshold, in which the rejection is valid. For this reason, we estimate the occurrence rate of Q-bursts to be 2.1 per minute, N-bursts to be 49.6 per minute, and V-bursts 73.8 per second.

These observations compare reasonably well with experimental observations of TLE occurrence rates. For example, lightning is estimated to occur 50−100 times per second [*Rakov and Uman*, 2003], elves ∼35−72 per minute [*Chen et al.*, 2008; *Hsu et al.*, 2009], sprites 0.5−2.8 per minute [*Sato and Fukunishi*, 2003; *Ignaccolo et al.*, 2006; *Chen et al.*, 2008; *Hsu et al.*, 2009], and gigantic jets 0.01 per minute [*Chen et al.*, 2008]. If one assumes that half of the elves are N-bursts and the other half V-bursts, that 100% of the lightning produces V-bursts, that 100% of the sprites produce N-bursts, and that 100% of the gigantic jets produce Q-bursts, these numbers yield: 51-101 V-bursts per second, 19 to 39 N-burst per minute and 0.01 Q-bursts per minute. While the V-burst and N-burst occurrence rates are reasonably close to these values, the Q-burst occurrence rate is about 100 times higher than this estimate. *Chen et al.* [2008] based their estimates on only 13 gigantic jet observations, however. Based on the Q-burst observations presented here, either the occurrence rate of gigantic jets has been significantly underestimated or other events, such as delayed sprites that produce Q-burst-like signatures, play a more prominent

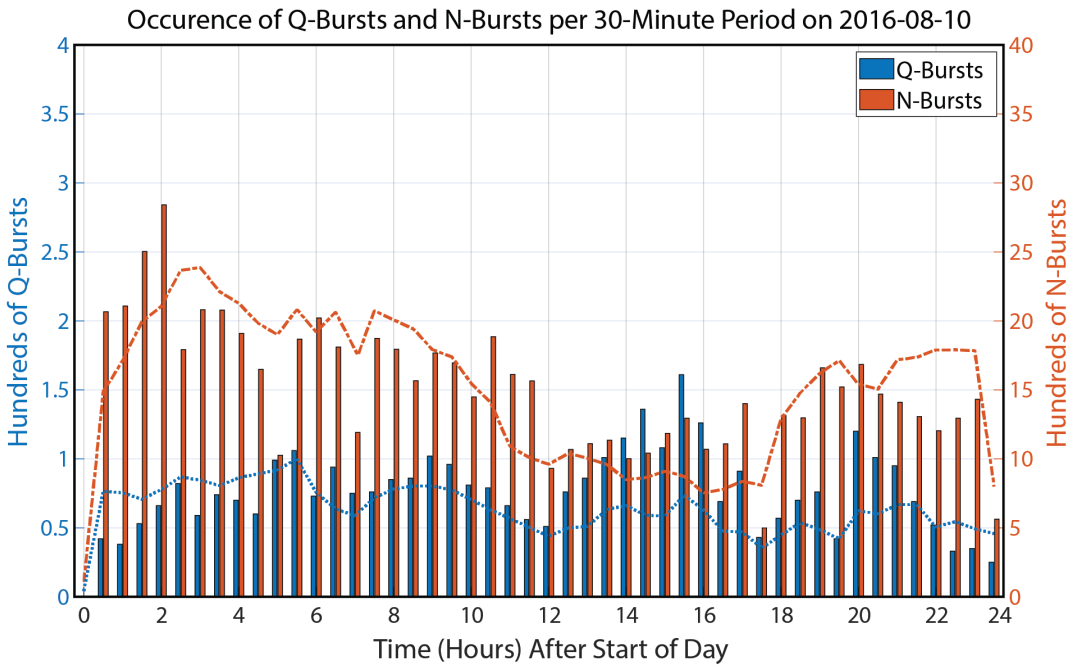

Figure 4-6. Rate of Q-Burst and V-Burst occurrence over 24 hours on 10 August, 2016.

role in these statistics than expected.

Additionally, the GLD360 detection algorithm supports the argument that the Q-burst detection figures above are minimum figures. GLD360 detects events using a 5−15 kHz signal bandwidth [*Said et al.*, 2010]. Q-bursts are limited to frequencies below 3 kHz and are therefore expected to be detected less frequently by GLD360. Some energy above 5 kHz is detected above the GLD360 threshold (but below the $\mu \pm 5\sigma$ VLF threshold), allowing for the detection of some Q-bursts, but not all.

A visualization of the occurrence rates of Q-bursts, N-bursts, and V-bursts is provided in Figures 4-6 and 4-7. Each bar in the graphs represents the total number of events observed during the half hour period. Week-long superposed-epoch averages are shown using dotted traces. Figures 4-6 shows that the number of Q-bursts does not vary significantly as a function of time of day. N-burst occurrence rates exhibit a strong diurnal variation, however. A clear increase in occurrence rates between 0000 and 0600 UTC and 1800 and 2400 UTC is observed in Figure 4-6. There is a clear decrease of N-bursts between the hours of 1200 and 1800 UTC.

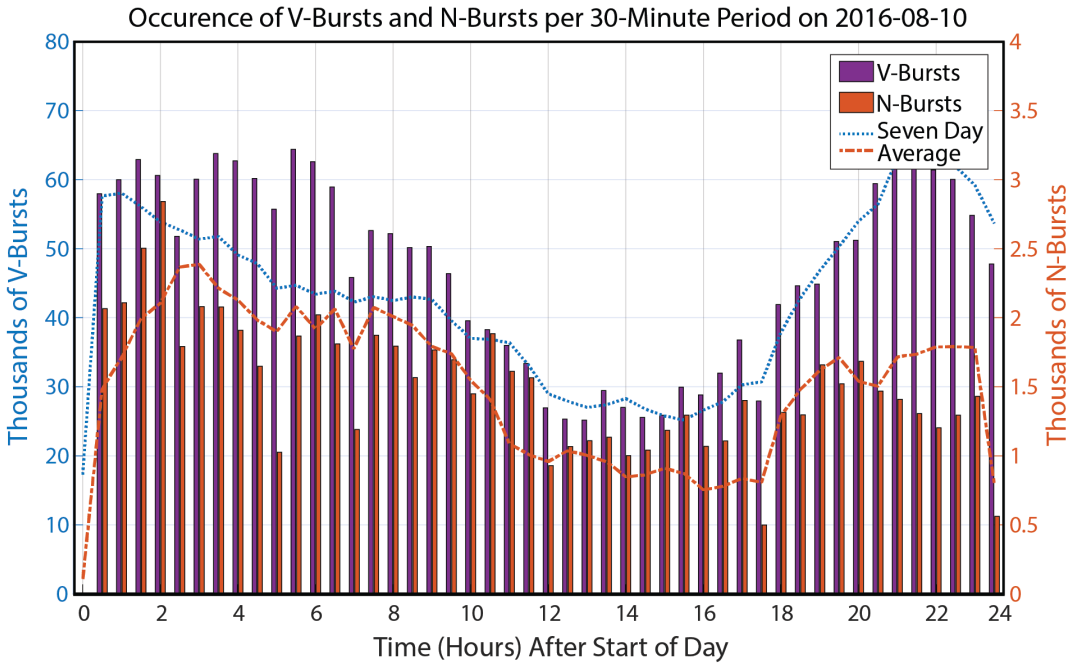

Figure 4-7. Rate of Q-Burst and V-Burst occurrence over 24 hours on 10 August, 2016.

Figure 4-7 shows the number of V-bursts and N-bursts per 30-minute period throughout the day. Both V-bursts and N-bursts exhibit a strong diurnal variation and respond similarly at the same time of day. This similarity may be due to the types of sources that produce each burst type. As discussed in Chapter 4, N-bursts and V-bursts are both closely related to lightning events. The occurrence rates of natural CG lightning is known to vary diurnally according to the time of day of peak lightning activity in the so-called "lightning chimneys" in Africa, Asia, and the Americas [*Williams*, 1992]. Q-bursts, on the other hand, appear to be special events that do not exhibit a strong diurnal variation.

Now that the occurrence rates of Q-bursts, N-bursts, and V-bursts is well documented and understood, the amount of energy injected into the waveguide by each burst type can be evaluated. The focus of the following section is the impact of each type of radio bursts and thereby their associated sources in driving the Schumann Resonances.

4.4 Schumann Band Excitation: Theory

Having identified and classified the ELF/VLF transients of interest to this study, we now determine how to calculate the energy that each transient injects into the Schumann Cavity below 50 Hz. Because the events are generally different distances from the receiver, one must discount the effects of attenuation and spreading. To do this, the fields are modeled as TEM components excited equally in all directions in the earth-ionosphere waveguide by a vertical electric dipole source. This section shows how ELF transient measurements at the receiver can be used to approximate the Power and Energy injected into the waveguide at a normalizing distance of 1 km distance from the source.

As discussed in Section 1.5, below 50 Hz, ELF waves propagate in the TEM mode, which can be simplified from the equations given in Section 1.5 as:

$$E_r^{\mathrm{TEM}}(\omega) = \frac{S_0^{0.5}\Delta_0(z)Ids(\omega)}{\sqrt{D\lambda}h}\sqrt{\frac{\mu_0}{\epsilon_0}}\sqrt{\frac{D/a}{\sin(D/a)}}G_0(z)G_0(z_s)\Lambda_0\exp(i\pi/4+ik_0DS_0) \quad (4\text{-}1)$$

$$H_\phi^{\mathrm{TEM}}(\omega) = \frac{S_0^{0.5}Ids(\omega)}{\mu_0\sqrt{D\lambda}h}\sqrt{\frac{D/a}{\sin(D/a)}}G_0(z)G_0(z_s)\Lambda_0\exp(i\pi/4+ik_0DS_0) \quad (4\text{-}2)$$

The Poynting Flux for such a wave is:

$$\begin{aligned} S_\theta^{\mathrm{TEM}}(\omega) &= E_r(\omega)H_\phi^*(\omega) \\ &= \frac{|S_0|\Delta_0(z)|Ids(\omega)|^2}{\mu_0 D\lambda h^2}\sqrt{\frac{\mu_0}{\epsilon_0}}\left(\frac{D/a}{\sin(D/a)}\right)|G_0(z)|^2|G_0(z_s)|^2|\Lambda_0|^2e^{-2\alpha D} \end{aligned} \quad (4\text{-}3)$$

This expression is proportional to the magnetic field intensity, which is:

$$|H_\phi^{\mathrm{TEM}}(\omega)|^2 = \frac{|S_0||Ids(\omega)|^2}{\mu_0^2 D\lambda h^2}\left(\frac{D/a}{\sin(D/a)}\right)|G_0(z)|^2|G_0(z_s)|^2|\Lambda_0|^2\exp(-2k_0\Im\{S_0\}D) \quad (4\text{-}4)$$

The expression above can be manipulated to express the magnetic field intensity at 1 km distance ($D_{1\mathrm{km}}$) given magnetic field intensity measurements at the receiver (D_{rcv}):

$$|H_\phi^{\mathrm{TEM}}(\omega, D_{1\mathrm{km}})|^2 = |H_\phi^{\mathrm{TEM}}(\omega, D_{\mathrm{rcv}})|^2\frac{\sin(D_{\mathrm{rcv}}/a)}{\sin(D_{1\mathrm{km}}/a)}\exp(2\alpha(D_{\mathrm{rcv}}-D_{1\mathrm{km}})) \quad (4\text{-}5)$$

where the attenuation rate α is given as a function of frequency by *Galejs et al.* [1972] in

Figure 7.2. In the ELF band below 50 Hz the signal attenuates at approximately 0.5 dB per Mm [*Galejs et al.*, 1972, p. 91]. Because the Poynting Flux is proportional to the magnetic field intensity, the Power radiated into the waveguide at 1 km distance from the source is proportional to the integral of the magnetic field intensity over the cross-sectional area of the waveguide at 1 km distance:

$$P(\omega, D_{1\text{km}}) = \int S_\theta(\omega, D_{1\text{km}}) dA \tag{4-6}$$

which at 1 km distance is well approximated by:

$$P(\omega, D_{1\text{km}}) = S_\theta(\omega, D_{1\text{km}}) 2\pi D_{1\text{km}} h \tag{4-7}$$

Thus, the power radiated into the waveguide is:

$$P(\omega, D_{1\text{km}}) \propto |H_\phi^{\text{TEM}}(\omega, D_{\text{rcv}})|^2 \frac{\sin(D_{\text{rcv}}/a)}{\sin(D_{1\text{km}}/a)} \exp(2\alpha(D_{\text{rcv}} - D_{1\text{km}})) 2\pi D_{1\text{km}} h \tag{4-8}$$

Which can be re-expressed to highlight only the terms that depend on distance:

$$P(\omega, D_{1\text{km}}) = K \left| H_\phi^{\text{TEM}}(\omega, D_{\text{rcv}}) \right|^2 \sin\left(\frac{D_{\text{rcv}}}{a}\right) e^{2\alpha D_{\text{rcv}}} \tag{4-9}$$

where K is a constant that accounts for all of the terms identified above and receiver calibration factors, for instance. The energy radiated into the waveguide is simply the integral of Equation 4-9 with frequency ω. It is easier to deal with time integration in our case, however. By application of Rayleigh's Theorem [*Bracewell*, 1986, p.112] we obtain:

$$W(D_{1\text{km}}) = K \sin\left(\frac{D_{\text{rcv}}}{a}\right) e^{2\alpha D_{\text{rcv}}} \int \left| H_\phi^{\text{TEM}}(t, D_{\text{rcv}}) \right|^2 dt \tag{4-10}$$

where we have assumed the signal $H_\phi(t)$ is band-limited to 5−50 Hz and the time integration is performed over 200 ms. The 200 ms time integration effectively includes frequencies down to 5 Hz in the integration. Significant rejection of interfering signals is obtained by integrating over a shorter period of time, however. Far fewer overlapping events were observed with an integration window of 100 ms, which effectively allows integration

down to 10 Hz. In practice, we did not notice a significant difference in our results, and have selected a 100 ms integration window to limit the rejection of overlapping events.

4.5 Schumann Band Excitation: Observations

Each burst is processed in the same manner to calculate the total energy injected into the waveguide by burst type. For a given event, the low-ELF receiver data (0−500 Hz bandwidth) is first digitally rotated to produce the transverse and radially directed components of the field.

The transverse field is low-pass filtered at 50 Hz to focus on the first 7 modes of the Schumann resonance and avoid power line hum interference in the signal integration. The receiver naturally implements a high-pass filter at 5 Hz, resulting in a signal with a flat response between 5 and 50 Hz. A 100 ms window is then applied to isolate the event. As mentioned in the previous section, a 200 ms window is preferred at this step, but the reduction in the number of overlapping events with 100 ms integration time is a practical trade-off to make. Lastly, the signal is squared and integrated according to equation 4-10 in order to calculate the total energy injected into the waveguide for the event. An α of 0.5 dB/Mm is employed, and the distance from the source to the receiver is determined using the GLD360 data set.

This process is applied across all events analyzed in the study using the Arrival Heights ELF receiver. This receiver site provides dual channel support over the entire week of observations with a high signal-to-noise ratio and low levels of local interference, aiding in the automation process.

The distribution of energy deposited into the Schumann Cavity by all Q-bursts observed at Arrival Heights on 07 August 2016 is shown in Figure 4-8. The energy is expressed on natural log scale in relative units, and the counts are distributed across 50 bins. The distribution is clearly log-normal, and the log-normal mean, which is the linear-scale median, and standard deviation are given on the plot.

In fact, the distribution of energy for each type of burst exhibits a log-normal

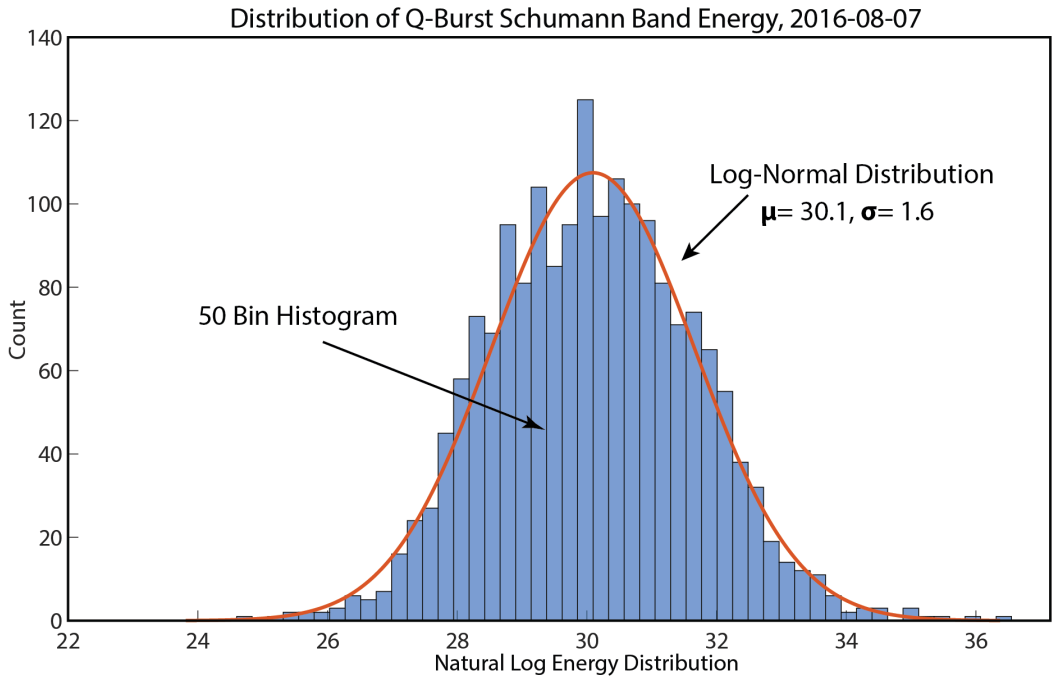

Figure 4-8. Distribution of total Q-burst energy on 07 August 2016

distribution. The distributions for each event type for the entire week of observations is shown in Figure 4-9. For each event type, the log-normal probability density function is plotted given the μ and σ calculated from the data. Note that the V-bursts distribution is narrower in energy while the Q-burst and N-burst distributions tend to be broader in energy: Q-bursts and N-bursts appear over a wider range of energies, while the energies associated with V-bursts are more consolidated. It is clear that Q-bursts and N-bursts contribute significantly more energy into the waveguide below 50 Hz *per burst* than V-bursts.

The log-normal distribution is fairly common: the logarithm of the data exhibits the familiar Gaussian-shaped normal distribution. The log-normal distribution can be described by parameters μ and σ on the natural log scale, and these values must be converted to the mean and standard deviation of the underlying distribution on linear scale. This information is conveyed in Figure 4-10. Note that the mean in the normal distribution corresponds to the median in the log-normal distribution.

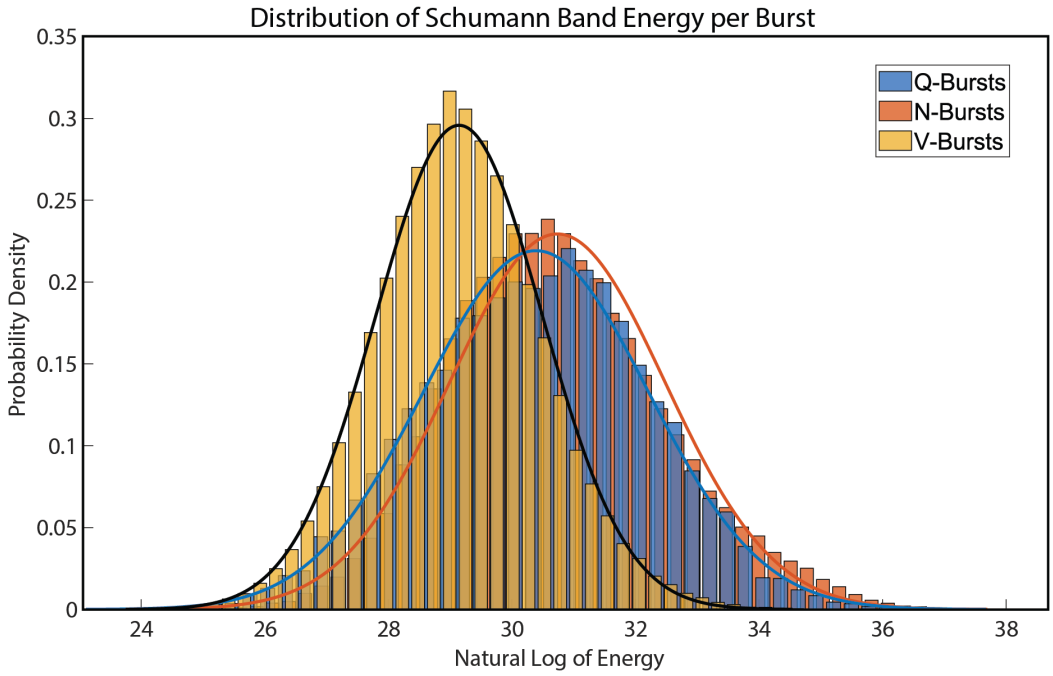

Figure 4-9. Distribution of energy injected into waveguide by burst type.

The distribution of energy associated with Q-bursts at Arrival Heights is plotted for each half hour of the day observed on 07 August 2016 in Figures 4-11. The distribution remains log-normal within each half hour of the day. Every event in each half hour is plotted vertically on the logarithmic scale and the mean (μ) and standard deviation (σ) of the log energy values are shown as bold traces. Figure 4-11 shows the diurnal variation (or lack thereof) in the distribution of Q-bursts over a 24 hour period.

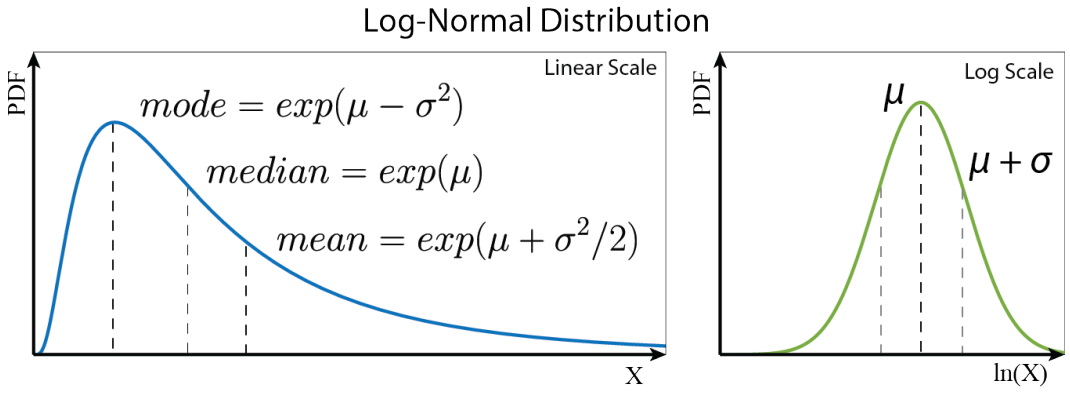

Figure 4-10. Visualization of the log-normal distribution.

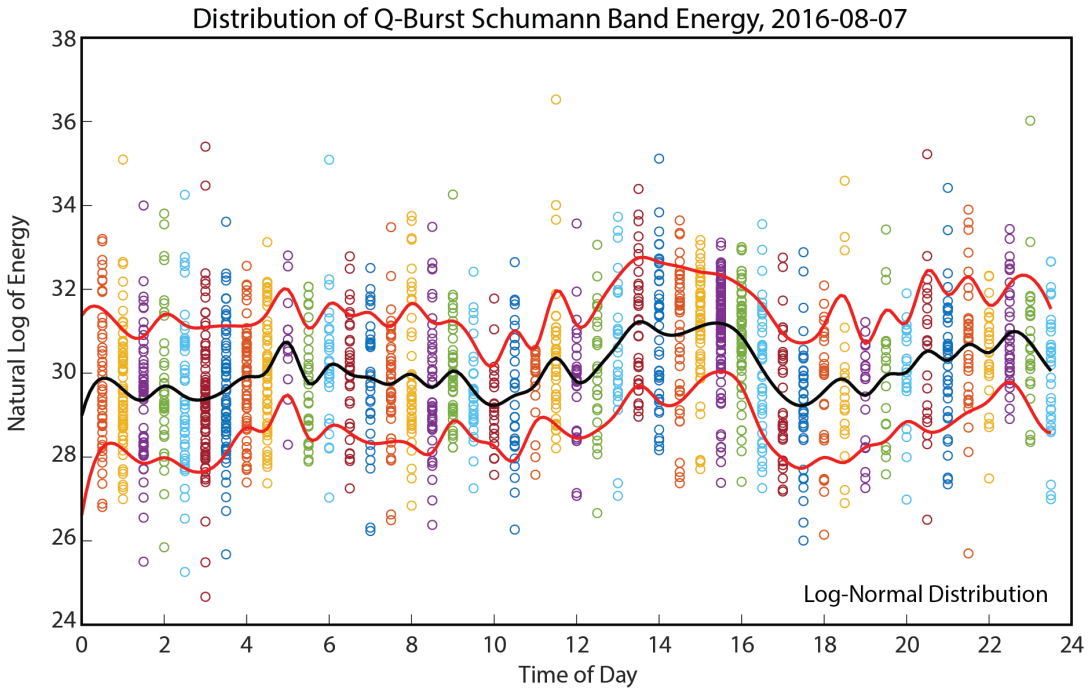

Figure 4-11. Diurnal variation in the distribution of Q-burst energy on 07 August 2016.

Figure 4-12 shows superposed epoch averages of the 24-hour variation of energy for all three types of events. Instead of plotting every event for each 30-minute period, the mean and standard deviations are plotted. Note, the energy per burst contributed to the band by Q-bursts and N-bursts is comparable, while the energy contributed by V-bursts is almost a factor of 10 below the median of Q-burst and N-burst energy. None of these traces exhibit a significant diurnal variation in the energy *per burst* injected in to the waveguide.

Now that burst occurrence rates are well understood and the energy radiated per burst is calculated, the total energy injected into the earth-ionosphere waveguide can be approximated. Recall that events can be detected in cases when the energy cannot be confidently evaluated; in order to account for these cases, we apply the observed event energy statistics to them.

Figure 4-13 shows the superposed epoch average of total energy injected into the Schumann Cavity per half-hour period by Q-bursts, N-bursts, and V-bursts over 24-hours. The mean energy per burst-type, calculated on a linear scale, for a given 30-minute period

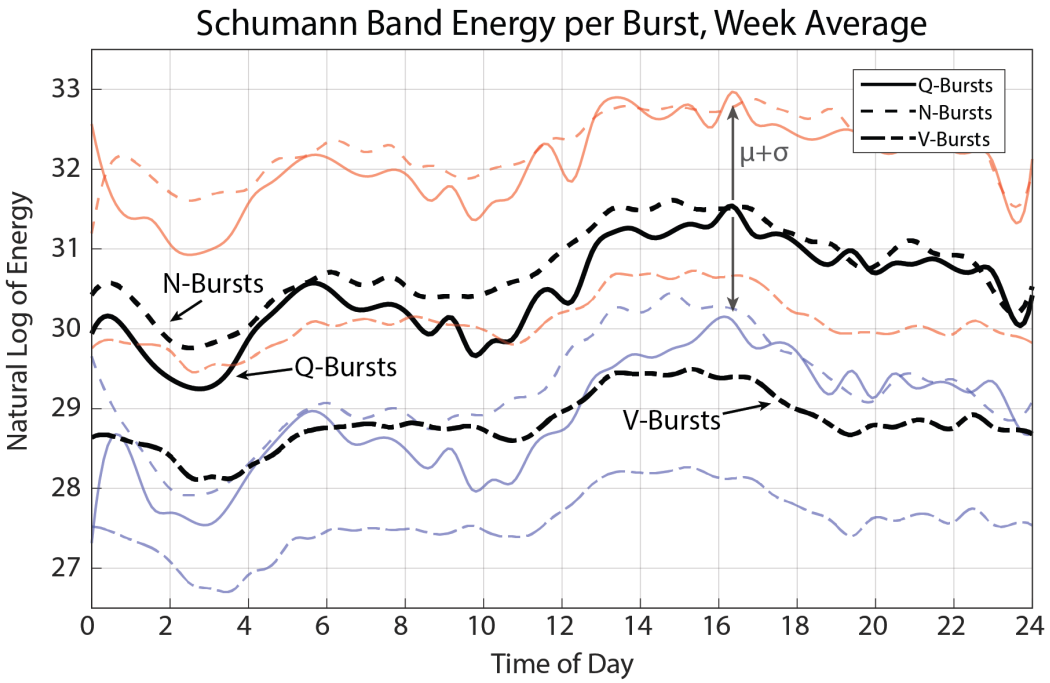

Figure 4-12. Distribution of burst energy over week of 04 August 2016.

is multiplied by the burst occurrence rate to produce the average total energy in the 30-minute period. The results are displayed on a log scale.

Figure 4-14 plots the same information as a percent of total energy injected into the Schumann Band below 50 Hz. On average, V-bursts contribute 76% of the total energy observed in the Schumann band, 23% is due to N-bursts, and 1% due to Q-bursts. The maximum N-burst energy occurs at the daily minimum of V-burst energy between 0600 and 0800 UT. A valley forms in the N-burst energy between 1200 and 1800 during which time the V-burst energy plateaus. The Q-burst energy remains relatively constant throughout the day, contributing less than a few percent of the daily observed energy.

The total energy contributed by burst type over the one week study is shown in Figures 4-15 and 4-16. Figure 4-15 shows the total energy injected into the system over 7 days. The linear average energy for each burst type in a 30-minute period calculated at Arrival heights is scaled by the rate of occurrence of the same burst type recorded across all sites. This is done over 7 days and is shown on log scale. Figure 4-16 provides this same

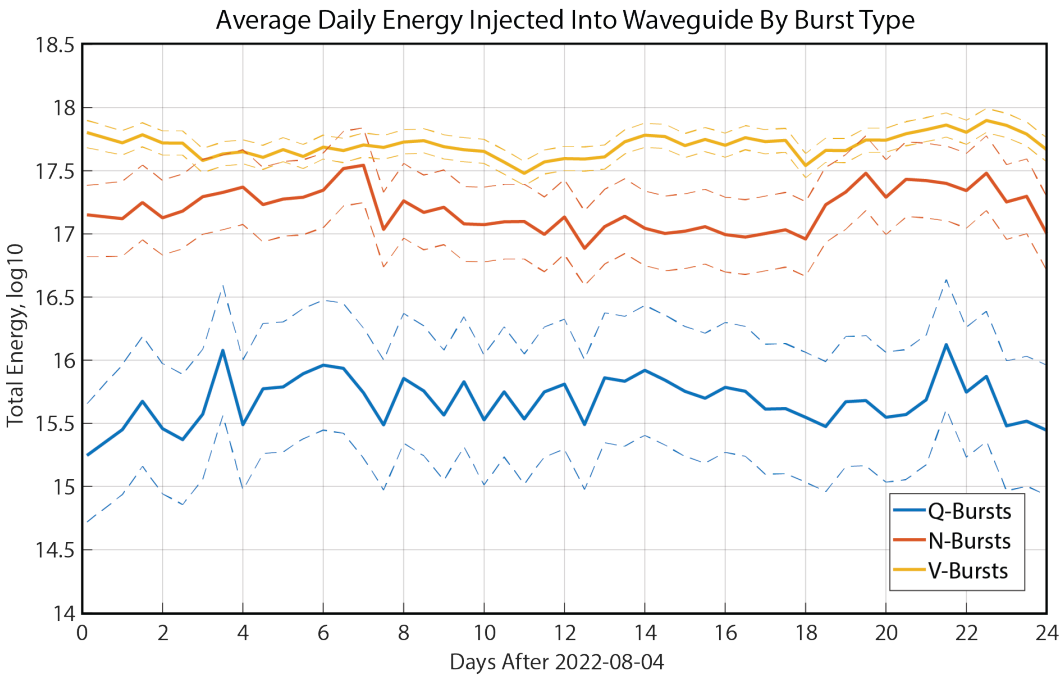

Figure 4-13. Superposed epoch average total energy injected into waveguide by burst type.

information as a percent of total energy observed below 50 Hz over the week.

On average, V-bursts contribute 76% of the total energy injected into the Schumann Cavity, N-bursts contribute 23%, and Q-burst contribute 1%. V-bursts are responsible for more than 50% of the energy in the Schumann Band >23 hours per day, while N-bursts are responsible for more than 50% of the energy for ∼47 minutes per day. N-bursts are responsible for more than 40% of the total injected energy for over 2 hours per day. Q-bursts, while rare, typically contribute 1% of the total injected energy, and for over 4 minutes per day contribute more than 10% of the total energy budget to the Schumann Band.

4.6 Summary of Schumann Band Excitation

In this chapter, we demonstrate that V-bursts occur far more frequently than N-bursts (23:1) and Q-bursts (644:1). Q-bursts and N-bursts contribute more energy per burst to the Schumann Cavity, however. Nevertheless, V-bursts contribute more total energy in the Schumann band than both of these sources combined (∼76%). The impact of N-bursts in driving the Schumann Resonances is significant, however: ∼23% of the total

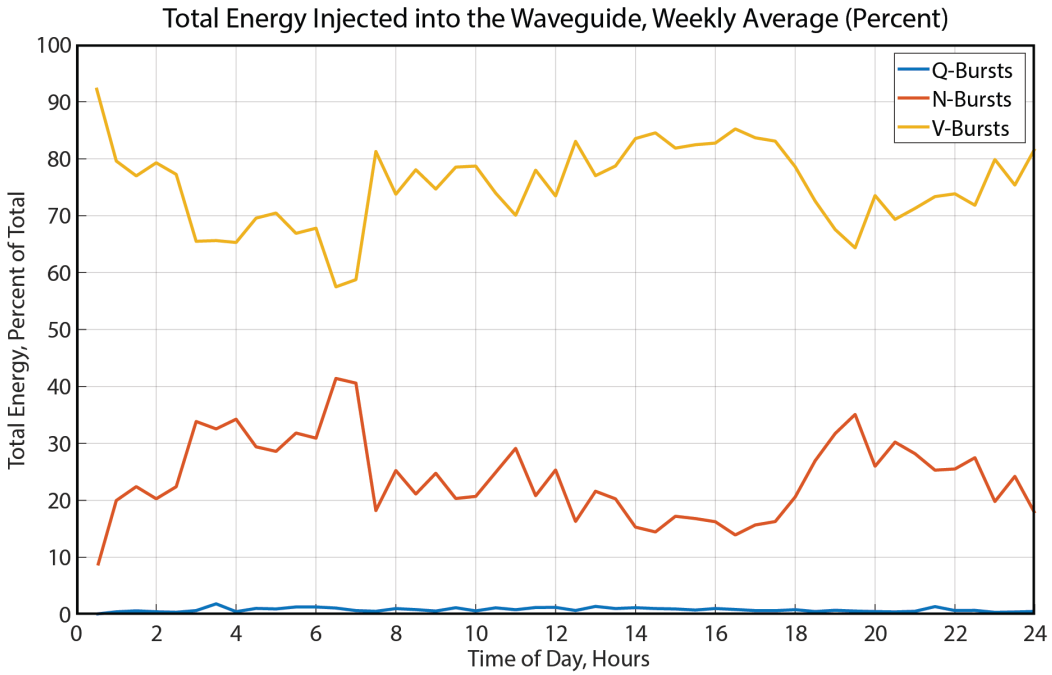

Figure 4-14. One week average total energy injected into waveguide by burst type as a percent of the total energy injected.

energy in the Schumann Band is sourced by N-bursts and for brief periods of time, N-bursts are the dominant source of energy in the band.

If, as Figure 3-7 suggests, elves-related N-bursts are 10−15 dB weaker in the ELF band than sprite-related N-bursts, and if elves occur 10 times more frequently than sprites [*Ignaccolo et al.*, 2006; *Chen et al.*, 2008; *Hsu et al.*, 2009], then one can argue that gigantic jets are responsible for 1% of the Schumann energy budget, sprites 5−8%, elves-related lightning 15−18%, and non-TLE-related lightning 76%. Lightning, elves-related lightning, and sprites are thus significant contributors to the Global Electric Circuit, while gigantic jets, though beautiful, are rare enough to contribute only a small fraction to the AC energy budget.

If one accepts the relationships between TLEs and ELF/VLF transients established in Chapters 2 and 3, it appears that lightning indeed drives the Schumann Resonances most of the time, but sprites and elves-related lightning are important contributors as well.

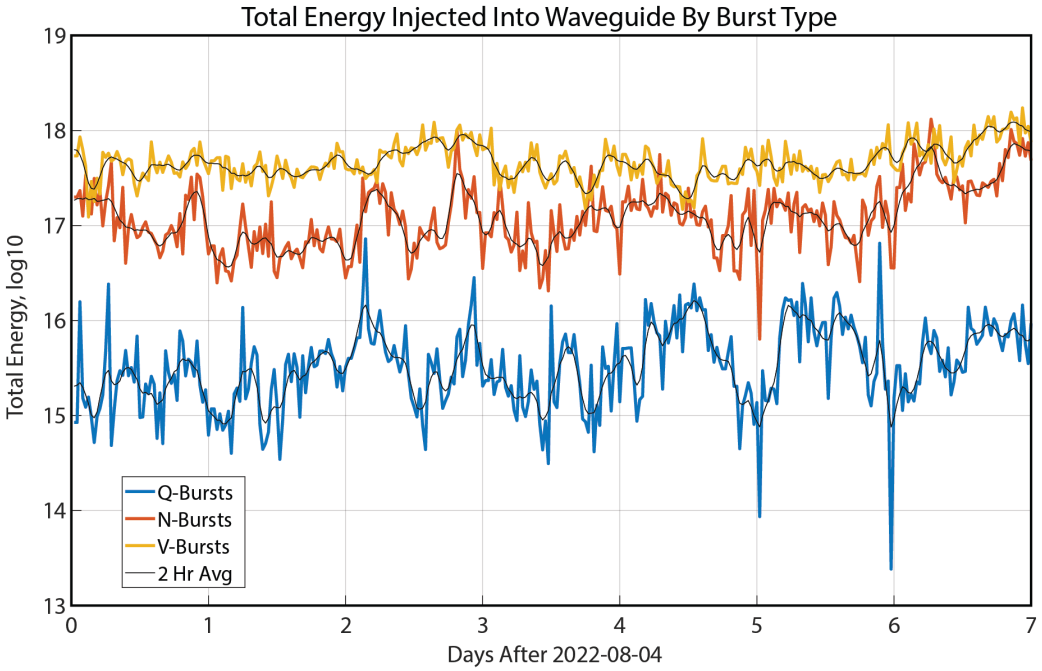

Figure 4-15. One week total energy injected into waveguide by burst typee.

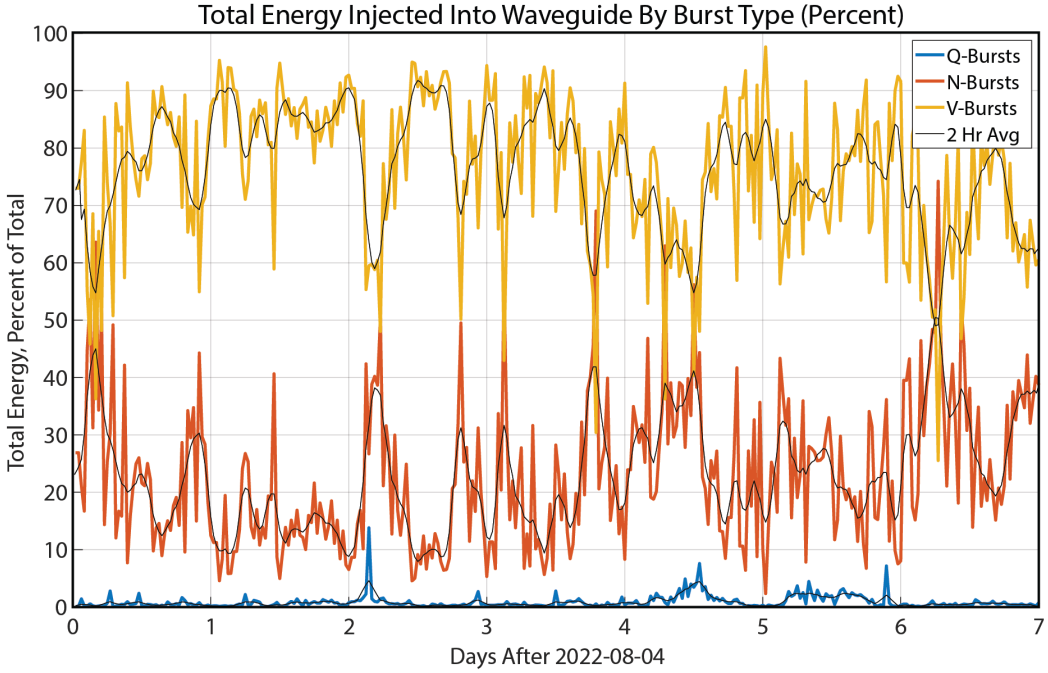

Figure 4-16. One week percent energy injected into waveguide by burst type.

CHAPTER 5
SUMMARY AND SUGGESTIONS FOR FUTURE WORK

5.1 Summary of Contributions

In this work, a new metric for the automatic detection and characterization of ELF/VLF radio bursts is presented and implemented. Gigantic jets are shown to be strongly associated to Q-burts, sprites are shown to be strongly linked with N-bursts, as are elves, and V-bursts were observed in association with CG lightning and elves-producing lightning. A week of observations are used to evaluate the occurrence rates of Q-bursts, N-bursts, and V-bursts, as well as the energy injected into the waveguide by each type of transient. These observations have a serious impact on the current state of understanding of the drivers of the Schumann Resonances and on the role of TLEs in the DC and AC Global Electric Circuit. The observations presented herein stress the surprisingly important role of sprites and sprite-related lightning as drivers of the Schumann Resonances, in addition to lightning.

This work illustrates the importance of dual ELF and VLF observations for proper classification of radio bursts and for more accurate identification of the types of sources that are likely to produce such radio bursts. We draw a distinction between events with an ELF component but no VLF component (Q-bursts) and those events which contain both ELF and VLF components (N-bursts), and identify a new type of transient with only VLF content (V-bursts).

The occurrence rates of Q-bursts, N-bursts, and V-bursts are calculated over the span of one week. V-bursts occur far more frequently than N-bursts and Q-bursts, by a factor of 28 and more than 600, respectively. V-bursts also contribute more total energy on average to the Schumann Band compared to Q-bursts and N-bursts despite the fact that the average V-burst contains far less ELF content. It was shown that while V-bursts contribute 76% of the the total energy injected into the Earth-ionosphere waveguide observed in Schumann Band, N-bursts contribute 23% on average, while Q-bursts contribute only $\sim$1%.

5.2 Suggestions for Future Work

The research presented herein has a raised a number of interesting questions, the answers to which are beyond the scope of this dissertation.

5.2.1 Delayed Sprites

In rare cases, the sprite onset is delayed in time from the causative lightning return stroke [*Li et al.*, 2008; *Lu et al.*, 2013; *Soula et al.*, 2015; *Wang et al.*, 2017]. Past work has shown that the sprite current itself radiates a delayed slow tail ELF pulse after the arrival of the wave launched by the initial return stroke [*Cummer et al.*, 1998; *Cummer*, 2003]. The present study was unable to uniquely identify these events in the ELF/VLF transient data. One sprite-related Q-burst was observed and presented, and for this case, several V-bursts were observed within 100 ms preceding the optical sprite detection and Q-burst. It was not possible to determine whether any of the V-bursts were directly associated with the sprite and Q-burst.

Detailed optical detection of a delayed sprite together with global radio observations would allow radio scientists to distinguish the radiation from the lightning channel and the sprite tendril. It is believed that delayed sprites are a result of the slow but strong currents in continuing current associated with powerful +CGs [*Bell et al.*, 1998; *Reising et al.*, 1999; *Cummer and Füllekrug*, 2001; *Cummer*, 2003], however some debate remains. These observations would allow for conclusive results to be drawn regarding the mechanism for ELF transient generating sources observed in association with sprites.

This understanding may also impact the observations in this work. Elves-producing lighting was shown to produce both N-bursts and V-bursts in relatively equal amounts. It is possible that in the cases where an N-burst was observed a time-delayed or spatially separated sprite was produced but not observed. If it is shown that the sprite does not radiate, perhaps there is a broad class of powerful lighting which produces sprites in some cases and elves in others.

5.2.2 Reverse-Looking ISUAL/Radio Statistics

In this work, the ISUAL data set was used as a reference to identify radio bursts in ELF/VLF data. This "forward-looking" analysis created an association between TLEs and their associated radio bursts. At the same time, given an ELF/VLF transient observation, we are not able to determine whether any TLE occurred or not. The present analysis cannot even offer a probability of occurrence.

It would be interesting to perform a "reverse-looking" experiment in which the radio data is used to identify and locate radio bursts that are compared against the observations of ISUAL. If a Q-burst, for example, triangulated to an area being monitored by the ISUAL satellite, how often does the instrument observe a gigantic jet or other TLE? Such observations would increase confidence in the observations made in this work and identify potential new sources of ELF energy (drivers of the SR).

5.2.3 Burst Rate Statistics: Seasonal Variations and Solar Cycle Variations

The statistics reported in Chapter 4 illustrate the variation in occurrence of bursts and, subsequently, the energy injected into the Earth-ionosphere waveguide by event type over the course of a week. It would be interesting to extend this study over the course of a complete year to investigate seasonal variations, and over the course of a solar cycle to evaluate the correlation between burst occurrence and solar irradiation. This investigation would further our understanding of the sun-Earth connection in regards to the coupling between the lower atmosphere below 100 km and the magnetosphere. Even 30-minute observations performed periodically throughout the day could address these issues. Observations could be expanded over an entire solar cycle for a more complete look at space-weather dependence.

Similar work was performed by *Williams* [1992] for which lightning occurrence rates, observed as variation in Schumann Resonances, were used as a proxy for global atmospheric temperatures. This idea could readily be extended to TLE observations as a proxy for temperatures or ionospheric conditions. While it is widely believed that lightning

source properties are the most important indicator of sprite and elve production, the effect of the ionospheric pre-conditions could also be important. The statistical effect of the ionosphere on sprite and elve production can be investigated in this type of study and may help to answer questions such as: do sprites and elves appear more often in periods of high solar activity or in quiescent periods?

5.2.4 Missing Links in The GEC Model

This work highlights the importance of TLEs in supporting the AC and DC Global Electric Circuit. A direct comparison of total burst energy in the Schumann Band and total integrated energy in the Schumann Band should correspond very effectively. Any variation in these two quantities could be attributed to either the detection threshold or the search window. Perhaps the $\mu \pm 5\sigma$ threshold prevents some key information from the coming to light in the study. Perhaps a galactic event could play a role in driving the Schumann Resonances, but does not produce the large ELF transient burst detected here. The comparison between total burst energy and the Schumann Resonances themselves suggested above will help to close the gap in this knowledge.

Past work [*Nickolaenko and Schekotov*, 2011] has suggested that extragalactic gamma ray bursts may excite the Schumann Resonance. Continual testing of the $\mu \pm 5\sigma$ threshold and 3 kHz frequency band cutoff could uncover further intricacies. The RTL dataset could be used to address this issue as some ELF component was detected, but the amount of energy in this band was determined to be insignificant in the context of the current study.

Andersen, J. B., History of communications/radio wave propagation from marconi to mimo, *IEEE Communications*, *55*, 6–10, 2017.

Appleton, E. V., The existence of more than one ionised layer in the upper atmosphere, *Nature*, *120*, 330, 1927.

Appleton, E. V., *Nobel Lectures in Physics 1942-1962*, Elsevier Publishing Company, 1964.

Appleton, E. V., and M. A. F. Barnett, Local reflection of wireless waves from the upper atmosphere, *Nature*, *115*, 333–334, 1925a.

Appleton, E. V., and M. A. F. Barnett, On some direct evidence for downward atmospheric reflection of electric rays, *Proceedings of the Royal Society of London. Series*, *109*, 621–641, 1925b.

Appleton, E. V., and F. W. Chapman, On the nature of atmospherics. iv, *Proceedings of the Royal Society of London*, *158*, 1–22, 1937.

Balser, M., and C. A. Wagner, Observations of earth-ionosphere cavity resonances, *Nature*, *188*, 638–641, 1960.

Balser, M., and C. A. Wagner, On frequency variations of the earth-ionosphere cavity modes, *Journal of Geophysical Research*, *67*, 4081–4083, 1962.

Barrington-Leigh, C. P., U. S. Inan, and M. Stanley, Identification of sprites and elves with intensified video and broadband array photometry, *Journal of Geophysical Research*, *106*, 1741–1750, 2001.

Bell, T. F., S. C. Reising, and U. S. Inan, Intense continuing currents following positive cloud-to-ground lightning associated with red sprites, *Geophysical Research Letters*, *25*, 1285–1288, 1998.

Berger, K., Novel observations on lightning discharges: Results of research on mount san salvatore, *Journal of The Franklin Institute*, *283*, 478–525, 1967.

Berger, K., Parameters of lightning flashes, *Electra*, *80*, 223–237, 1975.

Bering III, E. A., A. A. Few, and J. R. Benbrook, The global electric circuit, *Physics Today*, pp. 24–19, 1998.

Boccippio, D. J., E. R. Williams, S. J. Heckman, W. A. Lyons, I. T. Baker, and R. Boldi, Sprites, elf transients, and positive ground strokes, *Science*, *269*, 1088–1091, 1995.

Boeck, W. L., O. H. Vaughan, R. Blakeslee, B. Vonnegut, and M. Brook, Lightning induced brightening in the airglow layer, *Geophysical Research Letters*, *19*, 99–102, 1992.

Boys, C. V., Progressive lightning, *Nature*, *118*, 749–750, 1926.

Bracewell, R. N., *The Fourier transform and its applications*, McGraw-hill New York, 1986.

Brooks, M., *Sferics from the Encylopdeia of Science and Technology*, New York: McGraw Hill, 1992.

Budden, K. G., *The Wave-Guide Mode Theory of Wave Propagation*, Logos Press, 1961.

Burke, C., and D. Jones, Global radiolocation in the lower elf frequency band, *Journal of Geophysical Research: Atmospheres*, *100*, 26,263–26,271, 1995.

Burrows, C. R., The history of radio wave propagation up to the end of world war i, *Proceedings of the IRE*, *50*, 682–684, 1962.

Chalmers, J. A., *Atmospheric Electricity*, International Series of Monographs in Natural Philosophy, 1967.

Chapman, F. W., D. L. Jones, J. D. W. Todd, and R. A. Challinor, Observations on the propagation constant of the earth-ionosphere wave-quide in the frequency band 8 c/s to 16 kc/s, *Radio Science*, *1*, 1273–1282, 1966.

Chen, A. B., C.-L. Kuo, Y.-J. Lee, and H.-T. Su, Global distributions and occurrence rates of transient luminous events, *Journal of Geophysical Research: Space Physics*, *113*, 2008.

Chern, J. L., R. R. Hsu, S. B. Mende, and H. Fukunishi, Global survey of upper atmospheric transient luminous events on the rocsat-2 satellite, *Journal of Atmospheric and Solar-Terrestrial Physics*, *65*, 647–659, 2003.

Cummer, S. A., Lightning and ionospheric remote sensing using vlf/elf radio atmospherics, Ph.D. thesis, Stanford University, 1997.

Cummer, S. A., Current moment in sprite-producing lightning, *Journal of Atmospheric and Solar-Terrestrial Physics*, *65*, 499–508, 2003.

Cummer, S. A., Quantification of the troposphere-to-ionosphere charge transfer in a gigantic jet, *Nature Geoscience*, *2*, 617–620, 2009.

Cummer, S. A., and M. Füllekrug, Unusually intense continuing current in lightning produces delayed mesospheric breakdown, *Geophysical Research Letters*, *28*, 495–498, 2001.

Cummer, S. A., and U. Inan, Measurement of charge transfer in sprite-producing lightning using elf radio atmospherics, *Geophysical Research Letters*, *24*, 1731–1734, 1997.

Cummer, S. A., and U. S. Inan, Ionospheric e region remote sensing with elf radio atmospherics, *Radio Science*, *35*, 1437–1444, 2000.

Cummer, S. A., U. S. Inan, T. F. Bell, and C. P. Barrington-Leigh, Elf radiation produced by electrical currents in sprites, *Geophysical Research Letters*, *25*, 1281–1284, 1998.

Cummer, S. A., H. U. Frey, S. B. Mende, R. R. Hsu, H. T. Su, A. B. Chen, H. Fukunishi, and Y. Takahashi, Simultaneous radio and satellite optical measurements of high-altitude sprite current and lightning continuing current, *Journal of Geophysical Research: Space Physics*, *111*, 2006.

Davies, K., *Ionospheric Radio*, Peter Peregrinus Ltd, 1990.

de Forest, L., Recent developments in the work of the federal telegraph company, *Proceedings of the Institute of Radio Engineers*, pp. 37–51, 1912.

Dwyer, J. R., and M. A. Uman, The physics of lightning, *Physics Reports*, *534*, 147–241, 2014.

Eccles, W. H., On the diurnal variations of the electric waves occurring in nature, and on the propagation of electric waves round the bend of the earth, *Proceedings of the Royal Society of London*, *87*, 79–99, 1912.

Franz, R. C., R. J. Nemzek, and J. R. Winckler, Television image of a large upward electrical discharge above a thunderstorm system, *Science*, *249*, 48–51, 1990.

Frey, H. U., S. B. Mende, S. E. Harris, and H. Heetderks, The imager for sprites and upper atmospheric lightning (isual), *Journal of Geophysical Research: Space Physics*, *121*, 8134–8145, 2016.

Fukunishi, H., Y. Takakashi, M. Kubota, and K. Sakanoi, Elves: Lightning-induced transient luminous events in the lower-ionosphere, *Geophysical Research Letters*, *23*, 2157–2160, 1996.

Fullekrug, M., Schumann resonances in magnetic field components, *Journal of Atmospheric and Terrestrial Physics*, *57*, 479–484, 1996.

Fullekrug, M., Detection of thirteen resonances of radio waves from particularly intense lightning discharges, *Geophysical Research Letters*, *32*, 2005.

Fullekrug, M., and A. C. Fraser-Smith, Further evidence for a global correlation of the earth-ionosphere cavity resonances, *Geophysical Research Letters*, *23*, 2773–2776, 1996.

Füllekrug, M., and S. Constable, Global triangulation of intense lightning discharges, *Geophysical Research Letters*, *27*, 333–336, 2000.

Füllekrug, M., and M. J. Rycroft, The contribution of sprites to the global atmospheric electric circuit, *Earth, Planets and Space*, *58*, 1193–1196, 2006.

Füllekrug, M., N. Smith, A. Mezentsev, R. Watson, I. Astin, S. Gaffet, A. Evans, and M. Rycroft, Classifying onset durations of early vlf events: Scattered field analysis and new insights, *Radio Science*, *50*, 1141–1149, 2015.

Galejs, J., A. L. Cullen, V. A. Fock, and J. R. Wait, *Terrestrial Propagation of Long Electromagnetic Waves*, Pergamon Press, 1972.

Gardiner, G. W., Origin of the term ionosphere, *Nature*, *224*, 1096, 1969.

Gauss, C. F., *Allgemeine Theorie des Erdmagnetismus*, Resultate aus den Beobachtungen des Magnetischen Vereins im Jahre 1838, 1839.

Glassmeier, K.-H., and B. T. Tsurutani, Carl friedrich gauss – general theory of terrestrial magnetism – a revised translation of the german text, *History of Geo- and Space Sciences*, *5*, 11–62, 2014.

Guha, A., E. Williams, R. Boldi, and G. Satori, Aliasing of the schumann resonance background signal by sprite-associated q-bursts, *Journal of Atmospheric and Solar-Terrestrial Physics*, *165*, 25–37, 2017.

Harrison, R. G., The carnegie curve, *Surveys in Geophysics*, *34*, 209–232, 2012.

Heaviside, O., On operators in physical mathematics. part i, *Proceedings of the Royal Society of London*, *52*, 504–529, 1892.

Heaviside, O., *Electromagnetic Theory I*, The Electrician, 1893a.

Heaviside, O., On operators in physical mathematics. part ii, *Proceedings of the Royal Society of London*, *54*, 105–143, 1893b.

Heaviside, O., *TELEGRAPHY THEORY from The New Volumes of the Encylopaedia Britannica, The Tenth Edition, Volume IX, Forming Volume XXXIII of the Complete Work*, vol. 9, 10 ed., Adam and Charles Black, 1902.

Hepburn, F., Atmospherics with very low-frequency components, *Nature*, *171*, 837–838, 1953.

Hepburn, F., Atmospheric waveforms with very low-frequency components below 1 kc/s known as slow tails, *Journal of Atmospheric and Terrestrial Physics*, *10*, 266–287, 1957.

Hertz, H., *Electric Waves*, Dover Publications, Inc., 1893.

Holzer, R. E., and O. E. Deal, Low audio-frequency electromagnetic signals of natural origin, *Nature*, *177*, 536–537, 1956.

Houston Jr, R., The effect of certain solar radiations on the lower ionosphere, *Journal of Atmospheric and Terrestrial Physics*, *12*, 225–235, 1958.

Hsu, R., A. B. Chen, C. Kuo, H. Su, H. Frey, S. Mende, Y. Takahashi, and L. Lee, On the global occurrence and impacts of transient luminous events (tles), *AIP Conference Proceedings*, *1118*, 99–107, 2009.

Hsu, R. R., S. H. T., C. A. B., and K. C. L., Selected results from the isual/formosat2 mission, *Terrestrial Atmospheric and Oceanic Sciences*, *28*, 525–544, 2017.

Hu, W., S. A. Cummer, and W. A. Lyons, Testing sprite initiation theory using lightning measurements and modeled electromagnetic fields, *Journal of Geophysical Research: Atmospheres*, *112*, 2007.

Ignaccolo, M., T. Farges, A. Mika, T. H. Allin, O. Chanrion, E. Blanc, T. Neubert, A. C. Fraser-Smith, and M. Füllekrug, The planetary rate of sprite events, *Geophysical Research Letters*, *33*, 2006.

Inan, U. S., N. G. Lehtinen, R. Moore, K. Hurley, S. Boggs, D. Smith, and G. Fishman, Massive disturbance of the daytime lower ionosphere by the giant γ-ray flare from magnetar sgr 1806–20, *Geophysical research letters*, *34*, 2007.

Jansky, J., and V. P. Pasko, Charge balance and ionospheric potential dynamics in time-dependent global electric circuit model, *Journal of Geophysical Research: Space Physics*, *119*, 10,184–10,203, 2014.

Kennelly, A. E., On the elevation of the electrically-conducting strata of the earth's atmosphere, *Electrical World and Engineer*, *39*, 473, 1902.

Koochak, Z., and A. Fraser-Smith, Single-station lightning location using azimuth and time of arrival of sferics, *Radio Science*, *55*, 2020.

Kotovsky, D. A., Response of the nighttime upper mesosphere to electric field changes produced by lightning discharges, Ph.D. thesis, The University of Florida, 2016.

Krehbiel, P. R., J. A. Riousset, V. P. Pasko, R. J. Thomas, W. Rison, M. A. Stanley, and H. E. Edens, Upward electrical discharges from thunderstorms, *Nature Geoscience*, *1*, 233–237, 2008.

Kuo, C.-L., et al., Discharge processes, electric field, and electron energy in isual-recorded gigantic jets, *Journal of Geophysical Research: Space Physics*, *114*, 2009.

Lee, L.-C., G.-S. Chang, and T. Nan-Hong, Space programs in taiwan, *Nuclear Physics B - Proceedings Supplements*, *243*, 74–82, 2013.

Li, J., and S. Cummer, Estimation of electric charge in sprites from optical and radio observations, *Journal of Geophysical Research: Space Physics*, *116*, 2011.

Li, J., and S. A. Cummer, Measurement of sprite streamer acceleration and deceleration, *Geophysical Research Letters*, *36*, 2009.

Li, J., S. A. Cummer, W. A. Lyons, and T. E. Nelson, Coordinated analysis of delayed sprites with high-speed images and remote electromagnetic fields, *Journal of Geophysical Research: Atmospheres*, *113*, 2008.

Liu, N., Model of sprite luminous trail caused by increasing streamer current, *Geophysical Research Letters*, *37*, 2010.

Lu, G., S. A. Cummer, W. A. Lyons, and P. R. Krehbiel, Lightning development associated with two negative gigantic jets, *Geophysical Research Letters*, *38*, 2011.

Lu, G., S. A. Cummer, J. Li, L. Zigoneanu, and W. A. Lyons, Coordinated observations of sprites and in-cloud lightning flash structure, *Journal of Geophysical Research: Atmospheres*, *118*, 6607–6632, 2013.

Lyons, W. A., Characteristics of luminous structures in the stratosphere above thunderstorms as imaged by low-light video, *Geophysical Research Letters*, *21*, 875–878, 1994.

Lyons, W. A., Sprite observations above the u.s. high plains in relation to their parent thunderstorm systems, *Journal of Geophysical Research*, *101*, 29,641, 1996.

Lyons, W. A., T. E. Nelson, R. A. Armstrong, V. P. Pasko, and M. A. Stanley, Upward electrical discharges from thunderstorm tops, *Bulletin of the American Meteorological Society*, *84*, 445–454, 2003.

Malan, D. J., Sur les decharges orageuses dans la haute atmosphere, *Comptes rendus de l'Académie des Sciences*, *205*, 812–813, 1937.

Marconi, D., *My Father, Marconi*, McGraw Hill Book Company, Inc., 1962.

Marconi, G., *Wireless Telegraphic Communications*, 1909.

Maxwell, J. C., *A Treatise on Electricity and Magnetism*, Clarenden Press, 1873.

McRae, W. M., and N. R. Thomson, Solar flare induced ionospheric d-region enhancements from vlf phase and amplitude observations, *Journal of Atmospheric and Solar-Terrestrial Physics*, *66*, 77–87, 2004.

Mimno, H. R., The physics of the ionosphere, *Review of Modern Physics*, *9*, 1937.

Mitchell, M. F., Very low frequency remote sensing of the lower ionosphere, Ph.D. thesis, The University of Florida, 2015.

Moore, R., and H. Burch, The d region response to the august 2017 total solar eclipse and coincident solar flare, *Geophysical Research Letters*, *45*, 13–192, 2018.

Nickolaenko, A. P., and A. Y. Schekotov, Elf q-burst caused by extragalactic gamma ray burst, in *2011 XXXth URSI General Assembly and Scientific Symposium*, pp. 1–4, 2011.

Nickolaenko, A. P., M. Hayakawa, and Y. Hobara, Q-bursts: Natural elf radio transients, *Surveys in Geophysics*, *31*, 409–425, 2010.

Nicolet, M., and A. Aikin, The formation of the d region of the ionosphere, *Journal of Geophysical Research*, *65*, 1469–1483, 1960.

Ogawa, T., Fair-weather electricity, *Journal of Geophysical Research: Atmospheres*, *90*, 5951–5960, 1985.

Ogawa, T., and M. Komatsu, Analysis of q burst waveforms, *Radio Science*, *42*, 1–11, 2007.

Ogawa, T., and M. Komatsu, Q-bursts from various distances on the earth, *Atmospheric Research*, *91*, 538–545, 2008.

Ogawa, T., and M. Komatsu, Propagation velocity of vlf em waves from lightning discharges producing q-bursts observed in the range 10-15 mm, *Atmospheric Research*, *95*, 101–107, 2009.

Ogawa, T., and Y. Tanaka, Worldwide simultaneity of occurrence of a q-type elf burst in the schumann resonance frequency range, *Journal of Geomagnetism and Geoelectricity*, *19*, 377–384, 1967.

Ogawa, T., Y. Tanaka, and T. Miura, On the frequency response of the ball antenna for measuring elf radio signals, *Special Contributions, Geophysical Institute*, *6*, 9–12, 1966a.

Ogawa, T., Y. Tanaka, T. Miura, and M. Yasuhara, Observations of natural elf and vlf electromagnetic noises by using ball antennas, *Journal of Geomagnetism and Geoelectricity*, *18*, 443–454, 1966b.

Ogawa, T., a. Y. Tanak, and M. Yasuhara, Schumann resonances and worldwide thunderstorm activity, *Journal of Geomagnetism and Geoelectricity*, *21*, 447–452, 1969.

Pappert, R. A., and W. F. Moler, Propagation theory and calculations at lower extremely low frequencies (elf), *IEEE Transaction on Communications*, *22*, 438–451, 1974.

Parkinson, W., and O. Torrenson, The diurnal variation the electrical potential of the atmosphere over oceans, *Compt. Rend de l'Assemblee de Stockholm*, *8*, 340–345, 1931.

Pasko, V. P., Electric jets, *Nature*, *423*, 927–929, 2003.

Pasko, V. P., Blue jets and gigantic jets: transient luminous events between thunderstorm tops and the lower ionosphere, *Plasma Physics and Controlled Fusion*, *50*, 124,050, 2008.

Pasko, V. P., Recent advances in theory of transient luminous events, *Journal of Geophysical Research: Space Physics*, *115*, 1–24, 2010.

Pasko, V. P., U. S. Inan, T. F. Bell, and Y. N. Taranenko, Sprites produced by quasi-electrostatic heating and ionization in the lower ionosphere, *Journal of Geophysical Research*, *102*, 4529–4562, 1997.

Pasko, V. P., U. S. Inan, T. F. Bell, and S. C. Reising, Mechanism of elf radiation from sprites, *Geophysical Research Letters*, *25*, 3493–3496, 1998.

Pasko, V. P., U. S. Inan, and T. F. Bell, Mesosphere-troposphere coupling due to sprites, *Geophysical Research Letters*, *28*, 3821–3824, 2001.

Pasko, V. P., M. A. Stanley, J. D. Mathews, U. S. Inan, and T. G. Wood, Electrical discharge from a thundercloud top to the lower ionosphere, *Nature*, *416*, 152–154, 2002.

Pasko, V. P., J. Qin, and S. Celestin, Toward better understanding of sprite streamers: Initiation, morphology, and polarity asymmetry, *Surveys in Geophysics*, *34*, 797–830, 2013.

Rakov, V. A., and M. A. Uman, *Lightning Physics and Effects*, Cambridge University Press, 2003.

Ratcliffe, J. A., The physics of the ionosphere, *THE PROCEEDINGS OF THE INSTITUTION OF ELECTRICAL ENGINEERS*, *101*, 339–346, 1954.

Reising, S. C., U. S. Inan, T. F. Bell, and W. A. Lyons, Evidence for continuing current in sprite-producing cloud-to-ground lightning, *Geophysical Research Letters*, *23*, 3639–3642, 1996.

Reising, S. C., U. S. Inan, B. T. F., and L. W. A., Evidence for continuing current in sprite-producing cloud-to-ground lightning, *Geophysical Research Letters*, *23*, 3639–3642, 1999.

Roble, R. G., and I. Tzur, *The Earth's Electrical Environment*, The National Academies Press, 1986.

Rycroft, M. J., and A. Odzimek, Effects of lightning and sprites on the ionospheric potential, and threshold effects on sprite initiation, obtained using an analog model of the global atmospheric electric circuit, *Journal of Geophysical Research: Space Physics*, *115*, 2012.

Rycroft, M. J., K. A. Nicoll, K. L. Alpin, and R. G. Harrison, Recent advances in global electric circuit coupling between the space environment and the troposphere, *Journal of Atmospheric and Solar-Terrestrial Physics*, *90*, 198–211, 2012.

Said, R. K., U. S. Inan, and K. L. Cummins, Long-range lightning geolocation using a vlf radio atmospheric waveform bank, *Journal of Geophysical Research*, *115*, 2010.

Said, R. K., M. B. Cohen, and U. S. Inan, Highly intense lightning over the oceans: Estimated peak currents from global gld360 observations, *Journal of Geophysical Research: Atmospheres*, *118*, 6905–6915, 2013.

Sato, M., and H. Fukunishi, Global sprite occurrence locations and rates derived from triangulation of transient schumann resonance events, *Geophysical Research Letters*, *30*, 2003.

Satori, G., M. Rycroft, P. Bencze, and F. Marcz, An overview of thunderstorm-related research on the atmospheric electric field, schumann resonances, sprites, and the ionosphere at sopron, hungary, *Surveys in Geophysics*, *34*, 255–292, 2013.

Schumann, V. W., Über die strahlungslosen eigenschwingungen einer leitenden kugel, die von einer luftschicht und einer ionosphärenhülle umgeben ist, *Zeitschrift für Naturforschung A*, *7*, 149–154, 1951.

Schumann, V. W., Über die ausbreitung sehr langer elektrischer wellen um die erde und die signale des blitzes, *Il Nuovo Cimento*, *9*, 1116–1138, 1952.

Sentman, D., E. M. Wescott, D. Osborne, D. Hampton, and M. Heavner, Preliminary results from the sprites94 aircraft campaign: 1. red sprites, *Geophysical Research Letters*, *22*, 1205–1208, 1995.

Sentman, D. D., Schumann resonance spectra in a two-scale-height earth-ionosphere cavity, *Journal of Geophysical Research*, *101*, 9479–9487, 1996.

Shvets, A. V., Y. Hobara, and M. Hayakawa, Variations of the global lightning distribution revealed from three-station schumann resonance measurements, *Journal of Geophysical Research: Space Physics*, *115*, 2010.

Siingh, V., Devendra, V. Gopalakrishnan, and R. P. Singh, The atmospheric global electric circuit: An overview, *Atmospheric Research*, *84*, 91–110, 2007.

Singh, D. K., R. P. Singh, and A. K. Kamra, The electrical environment of the earth's atmosphere: A review, *Space Science Reviews*, *113*, 375–408, 2004.

Slyunyaev, N. N., N. V. Ilin, and E. A. Mareev, Modeling contributions of continents and oceans to the diurnal variation of the global electric circuit, *Geophysical Research Letters*, *46*, 5516–5525, 2019.

Soula, S., O. van der Velde, J. Montanya, P. Huet, C. Barthe, and J. Bor, Gigantic jets produced by an isolated tropical thunderstorm near réunion island, *Journal of Geophysical Research*, *116*, 2011.

Soula, S., E. Defer, M. Füllekrug, and O. van der Velde, Time and space correlation between sprites and their parent lightning flashes for a thunderstorm observed during the hymex campaign, *Journal of Geophysical Research: Atmospheres*, *120*, 2015.

Stanley, M., M. Brook, P. Krehbiel, and S. A. Cummer, Detection of daytime sprites via a unique sprite elf signature, *Geophysical Research Letters*, *27*, 871–874, 2000.

Stenbaek-Nielsen, H. C., and M. G. McHarg, High time-resolution sprite imaging: observations and implications, *Journal of Physics D: Applied Physics*, *41*, 14, 2008.

Stewart, B., *TERRESTRIAL MAGNETISM from The New Volumes of the Encylopaedia Britannica, The Ninth Edition*, 9 ed., Adam and Charles Black, 1882.

Su, H., Gigantic jets between a thundercloud and the ionosphere, *Nature*, *423*, 974–976, 2003.

Sung-Ming, H., R.-R. Hsu, L.-J. Lee, H.-T. Su, and C.-L. Kuo, Optical and radio signatures of negative gigantic jets: Cases from typhoon lionrock (2010), *Journal of Geophysical Research: Space Physics*, *117*, 2012.

Tanaka, Y. T., M. Hayakawa, Y. Hobara, A. P. Nickolaenko, K. Yamashita, M. Sato, Y. Takahashi, T. Terasawa, and T. Takahashi, Detection of transient elf emission caused by the extremely intense cosmic gamma-ray flare of 27 december 2004, *Geophysical Research Letters*, *38*, 2011.

Taranenko, Y. N., U. S. Inan, and T. F. Bell, Optical signatures of lightning-induced heating of the d region, *Geophysical Research Letters*, *19*, 1815–1818, 1996.

Taylor, W. L., and K. Sao, Elf attenuation rates and phase velocities observed from slow-tail components of atmospherics, *Radio Science*, *5*, 1453–1460, 1970.

Thomson, N. R., and M. A. Clilverd, Solar flare induced ionospheric d-region enhancements from vlf amplitude observations, *Journal of Atmospheric and Solar-Terrestrial Physics*, *63*, 1729–1737, 2001.

Tinsley, B. A., Influence of solar wind on the global electric circuit, and inferred effects on cloud microphysics, temperature, and dynamics in the troposphere, *Space Science Reviews*, *94*, 231–258, 2000.

Torreson, O. W., P. W. C., G. O. H., and W. G. R., Scientific results of cruise vii of the carnegie during 1928–1929 under command of captain j. p. ault, *The Quarterly Review of Biology*, *22*, 66, 1947.

Tuve, M. A., Early days of pulse radio at the carnegie institution, *Journal of Atmospheric and Terrestrial Physics*, *36*, 2079, 1974.

Uman, M. A., *The Lightning Discharge*, Dover Publications, 2001.

Van Der Velde, O. A., Multi-instrumental observations of a positive gigantic jet produced by a winter thunderstorm in europe, *Journal of Geophysical Research: Atmospheres*, *115*, 2010.

Van Der Velde, O. A., W. A. Lyons, T. E. Nelson, and S. A. Cummer, Analysis of the first gigantic jet recorded over continental north america, *JOURNAL OF GEOPHYSICAL RESEARCH*, *112*, 2007.

Van Der Velde, O. A., J. Montanya, A. Lopez, Jesus, and S. A. Cummer, Gigantic jet discharges evolve stepwise through the middle atmosphere, *Nature Communications*, 2019.

Vaughan, O. H. J., and B. Vonnegut, Recent observations of lightning discharges from the top of a thundercloud into the clear air above, *Journal of Geophysical Research: Atmospheres*, *94*, 13,179–13,182, 1989.

Wait, J. R., *Electromagnetic Waves in Stratified Media*, Pergamon Press, 1962.

Wang, Y., G. Lu, M. Ma, and H. Zhang, Triangulation of red sprites observed above a mesoscale convective system in north china, *Earth and Planetary Physics*, *3*, 2017.

Watanabe, K., F. Marmo, and J. Pressman, Formation of the lower ionosphere, *Journal of Geophysical Research*, *60*, 513–519, 1955.

Watson-Watt, R., Letter to the secretary of the radio research board, 1926, .

Watson Watt, R. A., and E. V. Appleton, On the nature of atmospherics. i, *Proceedings of the Royal Society of London*, *103*, 84–102, 1923.

Watson Watt, R. A., J. F. Herd, and F. E. Lutkin, On the nature of atmospherics. v, *Proceedings of the Royal Society of London*, *162*, 267–291, 1937.

Wescott, E. M., D. Sentman, D. Osborne, D. Hampton, and M. Heavner, Preliminary results from the sprites94 aircraft campaign: 2. blue jets, *Geophysical Research Letters*, *22*, 1209–1212, 1995.

Wescott, E. M., H. C. Stenbaek-Nielsen, D. D. Sentman, M. J. Heavner, D. R. Moudry, and F. T. S. Sabbas, Triangulation of sprites, associated halos and their possible relation to causative lightning and micrometeors, *Journal of Geophysical Research*, *106*, 10,467–10,478, 2001.

Whitten, R. C., and I. G. Poppoff, *Physics of the Lower Ionosphere*, Prentice Hall, Inc., 1965.

Williams, E. R., The schumann resonance: A global tropical thermometer, *Science*, *256*, 1184–1187, 1992.

Williams, E. R., The positive charge reservoir for sprite-producing lightning, *Journal of Atmospheric and Solar-Terrestrial Physics*, *60*, 689–692, 1998.

Williams, E. R., Problems in lightning physics—the role of polarity asymmetry, *Plasma Sources Science and Technology*, *15*, S91–S108, 2006.

Williams, E. R., The global electrical circuit: A review, *Atmospheric Research*, *91*, 140–152, 2009, 13th International Conference on Atmospheric Electricity.

Wilson, C. T. R., Iii. investigations on lighting discharges and on the electric field of thunderstorms, *Philosophical Transactions of the Royal Society of London*, *221*, 73–115, 1920.

Wilson, C. T. R., The electric field of a thundercloud and some of its effects, *Proceedings of the Physical Society*, *37*, 32D–37D, 1924.

Wilson, C. T. R., A theory of thundercloud electricity, *Proceedings of the Royal Society*, *236*, 297–317, 1956.

BIOGRAPHICAL SKETCH

Quincy Allen Flint was born in Dallas, Texas in 1991. He received the B.A.s in mathematics and computer science from Gustavus Adolphus College, Saint Peter, MN in 2014 and the M.S. and Ph.D. in electrical and computer engineering from the University of Florida, Gainesville, Florida in 2018 and 2022 respectively. His current research interests include lightning and transient luminous events, extremely-low frequency (ELF) and very-low frequency (VLF) radio wave generation and propagation, and electromagnetic source and propagation models. He is a member of the American Geophysical Union, Sigma Xi Research Society, and the Florida Institute for National Security. Mr. Flint is an engineer by day and a folk musician by night.